

The Texas Medical Center Library

DigitalCommons@TMC

The University of Texas MD Anderson Cancer
Center UTHealth Graduate School of
Biomedical Sciences Dissertations and Theses
(Open Access)


The University of Texas MD Anderson Cancer
Center UTHealth Graduate School of
Biomedical Sciences

8-2020

INVESTIGATING THE METABOLIC PROGRESSION OF GLIOBLASTOMA WITH HYPERPOLARIZED MAGNETIC RESONANCE

Travis Salzillo

Follow this and additional works at: https://digitalcommons.library.tmc.edu/utgsbs_dissertations

 Part of the [Biochemical Phenomena, Metabolism, and Nutrition Commons](#), [Diagnosis Commons](#),
[Medical Biophysics Commons](#), [Neoplasms Commons](#), [Nervous System Commons](#), [Oncology Commons](#),
and the [Radiology Commons](#)

Recommended Citation

Salzillo, Travis, "INVESTIGATING THE METABOLIC PROGRESSION OF GLIOBLASTOMA WITH HYPERPOLARIZED MAGNETIC RESONANCE" (2020). *The University of Texas MD Anderson Cancer Center UTHealth Graduate School of Biomedical Sciences Dissertations and Theses (Open Access)*. 1032.

https://digitalcommons.library.tmc.edu/utgsbs_dissertations/1032

This Dissertation (PhD) is brought to you for free and open access by the The University of Texas MD Anderson Cancer Center UTHealth Graduate School of Biomedical Sciences at DigitalCommons@TMC. It has been accepted for inclusion in The University of Texas MD Anderson Cancer Center UTHealth Graduate School of Biomedical Sciences Dissertations and Theses (Open Access) by an authorized administrator of DigitalCommons@TMC. For more information, please contact digitalcommons@library.tmc.edu.

The
TMC LIBRARY
Health Sciences Resource Center

**INVESTIGATING THE METABOLIC PROGRESSION OF GLIOBLASTOMA WITH
HYPERPOLARIZED MAGNETIC RESONANCE**

by

Travis Salzillo, B.Sc.

APPROVED:

Pratip Bhattacharya, Ph.D.
Advisory Professor

Ho-Ling Anthony Liu, Ph.D.

Richard Wendt, Ph.D.

John Hazle, Ph.D.

Frederick Lang, M.D.

Christopher Logothetis, M.D.

APPROVED:

Dean, The University of Texas
MD Anderson Cancer Center UTHHealth Graduate School of Biomedical Sciences

**INVESTIGATING THE METABOLIC PROGRESSION OF GLIOBLASTOMA WITH
HYPERPOLARIZED MAGNETIC RESONANCE**

A

Dissertation

Presented to the Faculty of

The University of Texas

MD Anderson Cancer Center UTHealth

Graduate School of Biomedical Sciences

In Partial Fulfillment

Of the Requirements

For the Degree of

Doctor of Philosophy

By

Travis Salzillo, B.S.

Houston, TX

August 2020

ACKNOWLEDGEMENTS

For my academic progress throughout my Ph.D., I would like to thank my advisor, Dr. Pratip Bhattacharya. He has been the perfect role model of an academic investigator which I aspire to achieve at some point in my career. Thank you for giving me the independence to explore the expanse of my project while still providing the guidance and support to develop my skills as an academic researcher.

My gratitude extends to the past and present members of the Bhattacharya laboratory who have supported me in this endeavor which include Dr. Niki Zacharias, Dr. Prasanta Dutta, Dr. Shivanand Pudakalakatti, Dr. Jaehyuk Lee, Dr. Sriram Shanmuga Velandy, Joseph Weygand, Caitlin McCowan, Vimbai Mawoneke, Akaanksh Shetty, Cassidy Andrichik, and Victoria Lee.

I was fortunate to work in a diverse and proficient department which promoted collaboration and critical advocacy. I want to especially thank Dr. David Piwnica-Worms, Dr. Seth Gammon, and Dr. Steven Millward for their support and invaluable recommendations to this work. I would also like to thank the staff of the Small Animal Imaging Facility, where all of the imaging for this work took place. I particularly want to acknowledge Charles Kingsley and Jorge Delacerda who helped train me with the equipment and assisted me with countless hyperpolarization experiments. Joy Gumin, who works in the Brain Tumor Center, was also instrumental in this work by taking care of all of the animal models and scheduling implantations according to my crazy imaging schedules.

I would like to acknowledge the members of my advisory committee, Dr. Richard Wendt, Dr. Anthony Liu, Dr. Frederick Lang, Dr. Christopher Logothetis, and Dr. John Hazle, for providing the time and support to cultivate a meaningful and worthwhile project while guiding me through my academic progress.

I am very appreciative of the funding that was allocated for this project. I especially want to acknowledge CPRIT Research Training Grant Award (RP170067) which funded the costs of my training during the final three years of my Ph.D.

Beyond academia, I would like to thank my immediate and extended family for their unconditional love and support through this process. I understand that much of my time was devoted to this degree, so thank you for still being there for me. I especially want to thank my mother who has always been by my side in each and every one of my endeavors as well as my father, who unfortunately passed while I was pursuing my degree, but would nonetheless remind me of how proud he was to have me as a son. I owe the entirety of my accomplishments to these two wonderful people.

Lastly, I would like to thank my lifelong and newly acquainted friends and significant other. They say to surround yourself with people who help make you a better version of you, and I've been lucky enough to do just that. My love goes out to Rhiannon who is the most kindhearted and intelligent person I know.

THE USE OF MAGNETIC RESONANCE IMAGING AND SPECTROSCOPY TO INTERROGATE THE METABOLISM OF BRAIN CANCER AND ASSOCIATED IMMUNE CELLS THROUGHOUT THE COURSE OF TUMOR PROGRESSION

Travis Salzillo, B.S.

Supervisory Faculty and Chair: Pratip Bhattacharya, Ph.D.

Rapid diagnosis and therapeutic monitoring of aggressive diseases such as glioblastoma (GBM) can improve patient survival by providing physicians the time to optimally deliver treatment. This includes early in development, while the tumor is still manageable, or following initial therapy, when alternative treatments should be considered. The main goal of this project was to determine whether metabolic imaging with hyperpolarized magnetic resonance spectroscopy (MRS) could detect changes in tumor progression more rapidly than conventional anatomic magnetic resonance imaging (MRI) in patient-derived GBM murine models. To comprehensively capture the dynamic nature of cancer metabolism, *in vivo* pyruvate-to-lactate conversion with hyperpolarized MRI, *ex vivo* metabolite pool size with nuclear magnetic resonance (NMR) spectroscopy, and *ex vivo* protein expression with immunohistochemistry (IHC) were measured at several time-points throughout tumor progression (tumor development, regression, and recurrence).

Hyperpolarized MRS was capable of detecting significant changes in pyruvate-to-lactate conversion throughout tumor progression, whereas tumor volume measured with anatomic MRI was not significantly altered during regression or recurrence. This was accompanied by alterations in amino acid and phospholipid lipid metabolism and

MCT1 expression. It is discussed how hyperpolarized MRS can help address clinical challenges such as identifying malignant disease prior to aggressive growth, differentiating pseudoprogression from true progression, quantifying treatment response, and predicting relapse. The individual evolution of these metabolic assays as well as their correlations with one another provides context for further academic research.

In addition to investigating GBM tumor progression, preliminary and supporting metabolic profiling data acquired with NMR spectroscopy is presented in the context of immunometabolism. Specifically, metabolic events associated with the licensing process of natural killer cells as well as macrophage polarization are analyzed. Collectively, this work demonstrates the value of interrogating the metabolism of GBM and tumor-associated immune cells with hyperpolarized MRS and NMR spectroscopy.

TABLE OF CONTENTS

APPROVAL PAGE.....	i
TITLE PAGE.....	ii
ACKNOWLEDGEMENTS	iii
ABSTRACT	v
TABLE OF CONTENTS	vii
LIST OF ILLUSTRATIONS	xiii
LIST OF TABLES.....	xvi
LIST OF ABBREVIATIONS	xvii
CHAPTER ONE: INTRODUCTION	1
State of Glioblastoma Patient Care.....	1
Medical Imaging.....	2
<i>Conventional Medical Imaging</i>	<i>2</i>
<i>Advanced Medical Imaging</i>	<i>2</i>
Cancer Metabolism.....	5
Established MR-Based Techniques to Study Cancer Metabolism	7

<i>Detected Metabolites Using ^1H MRS/NMR</i>	7
<i>Clinical ^1H MRS/NMR Spectroscopy</i>	8
<i>For Tumor Characterization</i>	9
<i>For Predicting Outcome or Response to Therapy</i>	9
Hyperpolarized Magnetic Resonance	10
<i>Spin Polarization in MR</i>	10
<i>Molecular and Metabolic MR</i>	12
<i>Hyperpolarization Techniques</i>	13
<i>Hyperpolarization in MR</i>	14
<i>Existing Hyperpolarized MR Literature</i>	16
Dissertation Overview	17
CHAPTER 2: GENERAL METHODS	19
Cell Lines	19
Animals	19
Anatomic Magnetic Resonance Imaging	20
Tumor Volume Measurements	21

Hyperpolarized Sample Preparation	21
¹³ C Magnetic Resonance Spectroscopy	22
Pyruvate-To-Lactate Measurements.....	22
Brain Sample Excision.....	23
Sample Preparation for Metabolite Extraction	23
Nuclear Magnetic Resonance Spectroscopy	24
Metabolite Pool Size Measurements	24
Sample Preparation for Immunohistochemistry	25
Immunohistochemistry	25
Protein Expression Measurements	26
Statistical Analysis	27
 CHAPTER 3: PRELIMINARY ANTOMIC AND METABOLIC IMAGING OF A PANEL OF PATIENT-DERIVED GBM XENOGRAFTS	 28
Motivation	28
Results.....	30

<i>Preliminary Anatomic MRI and Hyperpolarized ^{13}C MRS Of GSC Tumor-Bearing Mice</i>	30
Discussion	33
Central Hypothesis, Specific Aims, and Rationale	36
CHAPTER 4: MEASURING THE METABOLIC EVOLUTION OF GLIOBLASTOMA THROUGHOUT TUMOR DEVELOPMENT, REGRESSION, AND RECURRENCE WITH HYPERPOLARIZED MAGNETIC RESONANCE	38
Introduction	38
Methods	41
<i>Experimental Overview</i>	41
<i>Tumor Radiotherapy</i>	41
<i>Statistical Analysis</i>	42
Specific Aim 1: Track the Anatomic and Metabolic Evolution of GBM During Tumor Development	45
<i>Results</i>	45
<i>Discussion</i>	53

Specific Aim 2: Administer Radiation Therapy to GBM And Measure the Anatomic and Metabolic Response During Tumor Regression	55
<i>Results</i>	55
<i>Discussion</i>	61
Specific Aim 3: Monitor the Anatomic and Metabolic States of Regressed GBM Tumors to the Point of Relapse	63
<i>Results</i>	63
<i>Discussion</i>	67
Supplemental Data	72
<i>Results</i>	72
<i>Discussion</i>	83
CHAPTER 5: SUPPLEMENTAL DATA: PROFILING IMMUNOMETABOLISM.....	89
Introduction	89
Metabolic Profiling of Licensed and Unlicensed Natural Killer Cells	92
<i>Introduction</i>	92
<i>Methods</i>	94

<i>Results and Discussion</i>	97
Metabolic Profiling of CD14 ⁺ Monocytes and Polarized Macrophages	99
<i>Introduction</i>	99
<i>Methods</i>	101
<i>Results and Discussion</i>	105
CHAPTER 6: CONCLUDING REMARKS	109
BIBLIOGRAPHY	112
VITA	154

LIST OF ILLUSTRATIONS

Figure 1.1	Various types of contrast generated in MRI	4
Figure 1.2	Visualization of the Warburg effect	6
Figure 1.3	Instrumentation of two of the common hyperpolarization techniques	14
Figure 1.4	Polarization states during conventional and hyperpolarized MR experiments	16
Figure 3.1	Preliminary anatomic MRI and hyperpolarized ^{13}C MRS of GSC tumor-bearing mice	32
Figure 4.1	Anatomic and metabolic imaging of tumor-bearing mice over time	40
Figure 4.2	<i>In vivo</i> tumor volume significantly increases throughout tumor development	48
Figure 4.3	<i>In vivo</i> pyruvate-to-lactate conversion significantly increases throughout tumor development	49
Figure 4.4	<i>Ex vivo</i> metabolite pool sizes significantly increase throughout tumor development (Part 1)	50
Figure 4.5	<i>Ex vivo</i> metabolite pool sizes significantly increase throughout tumor development (Part 2)	51
Figure 4.6	<i>Ex vivo</i> MCT1 expression significantly increases throughout tumor development	52
Figure 4.7	<i>In vivo</i> tumor volume does not significantly decrease throughout regression	57

Figure 4.8	<i>In vivo</i> pyruvate-to-lactate conversion significantly decreases throughout tumor regression	58
Figure 4.9	<i>Ex vivo</i> metabolite pool sizes significantly decrease throughout tumor regression (Part 1)	59
Figure 4.10	<i>Ex vivo</i> metabolite pool sizes significantly decrease throughout tumor regression (Part 2)	60
Figure 4.11	<i>In vivo</i> tumor volume does not significantly increase throughout recurrence	65
Figure 4.12	<i>In vivo</i> pyruvate-to-lactate conversion significantly increases throughout tumor recurrence	66
Figure 4.13	Percent change of nLac, but not tumor volume, is significantly altered during tumor regression and recurrence	70
Figure 4.14	Evolution of nLac, volume, and rate of change of volume following radiotherapy	71
Figure 4.15	Radiotherapy significantly extends survival of GSC 8-11 tumor-bearing mice	74
Figure 4.16	Tumor volume increases during development but does not significantly change throughout regression or recurrence	75
Figure 4.17	<i>In vivo</i> pyruvate-to-lactate conversion is significantly altered throughout tumor development, regression, and recurrence	76
Figure 4.18	<i>Ex vivo</i> metabolite pool sizes are significantly altered throughout tumor development and regression (Part 1)	77

Figure 4.19	<i>Ex vivo</i> metabolite pool sizes are significantly altered throughout tumor development and regression (Part 2)	78
Figure 4.20	Significant correlations were observed between tumor volume, <i>in vivo</i> pyruvate-to-lactate conversion, and <i>ex vivo</i> metabolite pool sizes	80
Figure 4.21	<i>Ex vivo</i> metabolite pool sizes are significantly correlated with tumor volume	81
Figure 4.22	Correlations were observed between individual <i>ex vivo</i> metabolite pool sizes	82
Figure 5.1	Metabolic profiling of licensed and unlicensed natural killer cells	98
Figure 5.2	Significantly altered metabolites in CD14+ monocytes residing in blood and tissue samples from healthy donors and GBM patients	107
Figure 5.3	Significantly altered metabolites in unpolarized (M0), classically activated (M1) and alternatively activated (M2A, M2B) macrophages	108

LIST OF TABLES

Table 4.1	List of significantly altered metabolites during tumor development and/or tumor regression	79
-----------	---	----

LIST OF ABBREVIATIONS

CNS	Central Nervous System
GBM	Glioblastoma
MRI	Magnetic Resonance Imaging
RF	Radio Frequency
PET	Positron Emission Tomography
MR	Magnetic Resonance
FDG	^{18}F - fluorodeoxyglucose
FET	O-(2- ^{18}F -Fluoroethyl)-L-tyrosine
FDOPA	6- ^{18}F -fluoro-L-3,4-dihydroxyphenylalanine
rBV	Relative Blood Volume
ADC	Apparent Diffusion Coefficient
CSI	Chemical Shift Imaging
NMR	Nuclear Magnetic Resonance
MRS	Magnetic Resonance Spectroscopy
2-HG	2-Hydroxyglutarate
NAA	N-Acetylaspartate
Cho	Total-Choline-Containing Metabolites
Lac	Lactate
Lip	Mobile Lipids
Cre	Creatine
Glu	Glutamate
Gln	Glutamine

Glx	Glutamate + Glutamine
Gly	Glycine
GSH	Glutathione
PC	Phosphocholine
GPC	Glycerophosphocholine
PCr	Phosphocreatine
IDH	Isocitrate Dehydrogenase
SNR	Signal-to-Noise
TE	Echo Time
TR	Repetition Time
CNI	Choline-to-NAA Index
ppm	Parts Per Million
DNP	Dynamic Nuclear Polarization
dDNP	Dissolution Dynamic Nuclear Polarization
MRSI	Magnetic Resonance Spectroscopic Imaging
GSC	Glioma Sphere-Forming Cells
PBS	Phosphate-Buffered Saline
IACUC	Institutional Animal Care and Use Committee
T1-w	T1-weighted
T2-w	T2-weighted
FLAIR	Fluid Attenuated Inversion Recovery
FA	Flip Angle
BW	Bandwidth

FOV	Field of View
NEX	Number of Excitations
TI	Inversion Time
TRIS	2-Amino-2-(hydroxymethyl)-1,3-propanediol
EDTA	Ethylenediaminetetraacetic acid
ROI	Region of Interest
ID	Inner Diameter
IHC	Immunohistochemistry
DSS-d6	4,4-dimethyl-4-silapentane-1-sulfonic acid
DAB	3,3'-Diaminobenzidine
TCGA	The Cancer Genome Atlas
MCT1	Monocarboxylate Transporter 1
LDH-A	Lactate Dehydrogenase A
CHC	α -cyano-4-hydroxycinnamate
BCAA	Branched Chain Amino Acid
ALT	Alanine Transaminase
SHMT	Serine Hydroxymethyltransferase
ROS	Reactive Oxygen Species
NAD ⁺	Nicotinamide Adenine Dinucleotide +
NAMPT	Nicotinamide phosphoribosyltransferase
NK	Natural Killer
PD-L1	Programmed Death-Ligand 1
TGF	Transforming Growth Factor

TNF	Tumor Necrosis Factor
CSF	Colony-Stimulating Factor
IL	Interleukin
MDSC	Myeloid-Derived Suppressor Cells
KIR	killer cell Ig-like
MHC	Major Histocompatibility Complex
FBS	Fetal Bovine Serum
ECAR	Extracellular Acidification Rate
OCR	Oxygen Consumption Rate
LPS	Lipopolysaccharide
TAM	Tissue-Associated Macrophages
PBMC	Peripheral Blood Mononuclear Cell
GM-CSF	Granulocyte-Macrophage Colony-Stimulating Factor
HD	Healthy Donor

CHAPTER ONE:

INTRODUCTION

State of Glioblastoma Patient Care

In 2020, an estimated 87,240 new cases of primary brain and other central nervous system (CNS) tumors will be diagnosed in the United States with 25,800 expected to be malignant ¹. WHO grade IV glioblastoma (GBM) is the most common malignant brain tumor in adults representing 48.3% of the cases as well as the most deadly with 5-year survival rates of merely 6.8%. Despite standard-of-care treatment with surgery, radiotherapy, and temozolomide chemotherapy, prevailing therapies remain palliative, and tumors are almost always recurrent and lead to median survival times of approximately 15 months ². The only other FDA-approved treatments for primary or recurrent GBM are carmustine wafers ^{3,4}, bevacizumab ⁵, lomustine ⁶, and tumor treating fields device ⁷, which have shown modest improvements in overall survival. A number of novel treatments such as epigenetic, viral, and gene therapies along with small molecule chemotherapeutics and immunotherapies are being studied extensively, and several clinical trials have been initiated ⁸; however, little to no impact on survival has been reported as factors such as relatively average mutational load, tumor heterogeneity, and molecular filtration by the blood-brain barrier challenge drug development for this disease ⁹. This failure to make major inroads points to the need for alternative approaches in the management of this disease.

Medical Imaging

Conventional Medical Imaging

Imaging has been used to inform anatomic-based intervention by determining the extent of involvement of the tumor, its proximity to functional regions, and monitoring recurrence. The primary modality for imaging GBM is magnetic resonance imaging (MRI) due to its exquisite soft tissue contrast ¹⁰. Conventional MRI measures ¹H signal originating from tissue in the body when excited in a magnetic field. The primary source of this signal is water, but lipids and other ¹H-containing molecules also contribute to the overall signal. In the most common MRI sequences, contrast between different types of tissue is generated by leveraging intrinsic relaxation properties of tissues, known as T1 and T2 relaxation, with the timing of excitation and readout radiofrequency (RF) pulses ¹¹. These sequences produce images that are typically associated with MRI (Fig. 1.1). Alternate types of contrast can be generated by measuring properties of the ¹H-containing molecules in the tissue such as concentration, macroscopic motion (due to vascular flow), microscopic motion (diffusion), and chemical exchange ¹².

Advanced Medical Imaging

Advanced imaging techniques provide the opportunity to examine the cancer in alternate biologic domains that may determine therapeutic vulnerability in specific subsets. Such a strategy would complement the prevailing anatomic-based classifiers and could potentially address several clinical challenges when it comes to improving patient survival and optimizing drug discovery. These include the early detection and

discrimination of malignant disease, rapid assessment of treatment efficacy (including distinguishing pseudo-progression from true progression), and prediction of tumor recurrence. This type of information is difficult to gain from coarse anatomic imaging, although the field of machine learning and computer vision has recently sparked interest in this through radiomics studies ^{13,14}. Instead, novel technologies have been developed in attempts to image the functional properties of cancer that are discovered through cancer biology research. This is achieved by measuring the uptake and/or utilization of molecular/metabolic contrast agents using primarily optical imaging, positron emission tomography (PET), and magnetic resonance (MR) techniques ^{15,16}.

Optical imaging has fantastic sensitivity and specificity for targeting cancer cells, which is why it is used in gold-standard diagnostic tools from *ex vivo* specimens ¹⁷. The main disadvantage of *in vivo* optical imaging is that the depth-of-penetration of the photons is limited to at most a few cm ¹⁸. Thus, it is typically confined to intraoperative imaging during surgery, where it has proven successful at “painting” malignant tissue to aid in resection ^{19,20}. PET is arguably the most common molecular imaging modality, and it is routinely used in the clinic to measure the uptake of ¹⁸F-fluorodeoxyglucose (FDG) in glycolytic tumors ^{21,22}. However, in some cancers, the background signal is too high to produce sufficient contrast. This is most notable in prostate cancer, where the background signal originates from the excrement in the bladder, and brain cancer, where there is high uptake in surrounding healthy gray matter ²³. There exist alternate PET agents which have shown promise in measuring brain tumor activity such as O-(2-¹⁸F-Fluoroethyl)-L-tyrosine (FET) ^{24,25}, 6-¹⁸F-fluoro-L-

3,4-dihydroxyphenylalanine (FDOPA) ^{26,27}, and ¹¹C-choline ^{28,29}, although details of these agents are outside the scope of this project.

Multiparametric MRI of the Brain

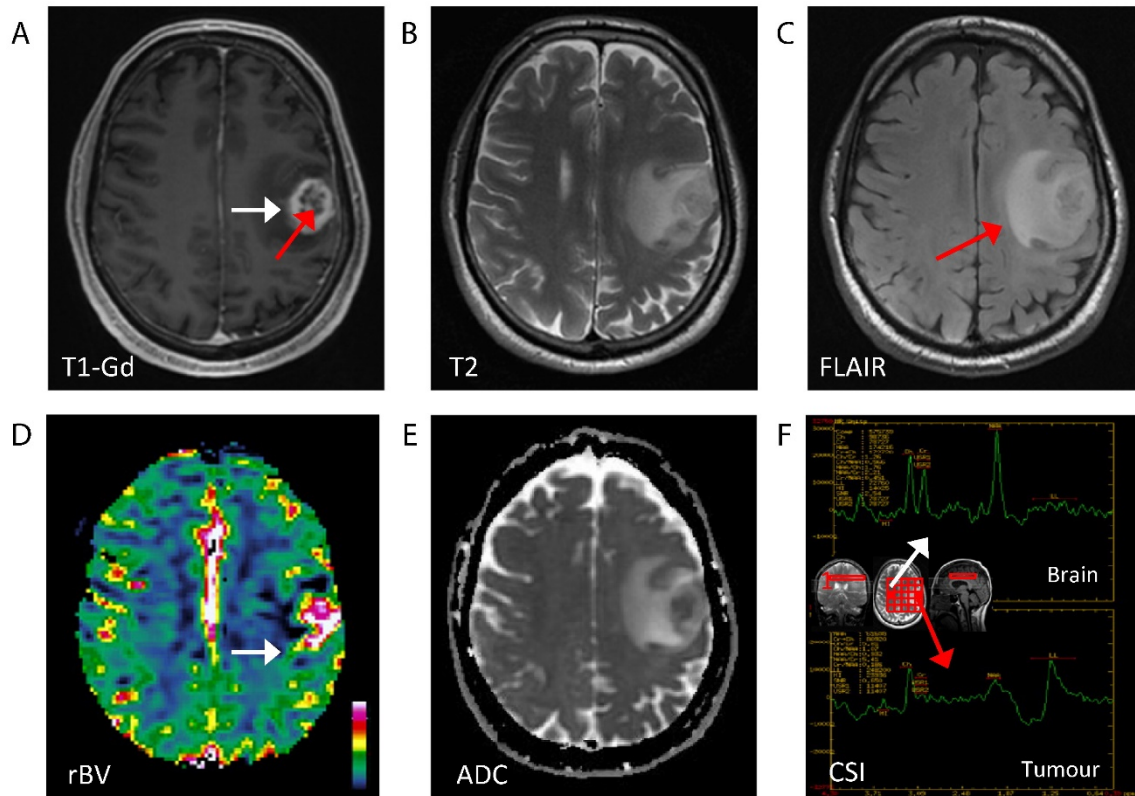


Figure 1.1: Various types of contrast generated in MRI. Pulse sequences which exploit differences in T1 and T2 relaxation are visualized in the top row: T1-weighted post-gadolinium contrast **(A)**, T2-weighted **(B)**, fluid-attenuated inversion recovery **(C)**. Pulse sequences which quantify functional properties of the tumor and microenvironment are shown in the bottom row: perfusion imaging quantifying relative blood volume (rBV) **(D)**, diffusion-weighted imaging quantifying apparent diffusion coefficient (ADC) **(E)**, and chemical shift imaging (CSI) quantifying relative metabolite concentrations **(F)**.

Reproduced with permission from Keunen O, Taxt T, Grüner R, Lund-Johansen M, Tonn J-C, Pavlin T, Bjerkvig R, Niclou SP, Thorsen F. Multimodal imaging of gliomas in the context of evolving cellular and molecular therapies. *Advanced Drug Delivery Reviews*. 2014;76(1):98-115. (License number: 1049029-1).

Lastly, MR-based techniques such as nuclear magnetic resonance (NMR) and magnetic resonance spectroscopy (MRS) have demonstrated the capability of measuring both steady-state metabolite pool sizes as well as the metabolic flux of injected agents. Cancer metabolism and the MR-based techniques to measure it are discussed in detail in the following sections.

Cancer Metabolism

The metabolites found in a cell are the products of gene expression and protein activity and thus can reflect the overall state of a cell ³⁰. Their concentrations also serve as feedback loops for certain cell regulation processes. For example, if a cell is too far away from a blood vessel and oxygen supply is low, oxidative phosphorylation becomes prohibitive. As a result, the HIF-1 α transcription factor is activated which alters the cells homeostatic state to operate in hypoxic conditions. This could lead to the secretion of growth factors such as VEGF to stimulate angiogenesis for increased oxygen supply ³¹. Some mutations can even induce direct metabolic switches. The most well-known example is the IDH1/2 mutation found in many low-grade gliomas ³². Normally, IDH1/2 catalyzes the decarboxylation of citrate to alpha-ketoglutarate, but the mutated form shuttles alpha-ketoglutarate away from the TCA cycle and into 2-hydroxyglutarate (2-HG) production. Thus, the accumulation of the oncometabolite 2-HG is a direct indicator of the IDH1/2 mutation, and many MRI studies are attempting to detect it *in vivo* ³³. When cancer cells rapidly proliferate, their metabolism begins to shift ^{34,35}. Elevated glucose uptake increases the cells energy production which is necessary to grow and divide. The Warburg effect describes the phenomenon where

cancer cells allocate a substantial proportion of their pyruvate from the TCA cycle and oxidative phosphorylation to lactate fermentation^{36,37} (Fig 1.2). This process is quicker at producing ATP, albeit not as efficient as oxidative phosphorylation. Moreover, it is postulated that this allows increased production of cellular building blocks such as choline and amino acids to provide the scaffolding for new cells. This shift to lactate production is the basis for *in vivo* hyperpolarized MR studies in this project.

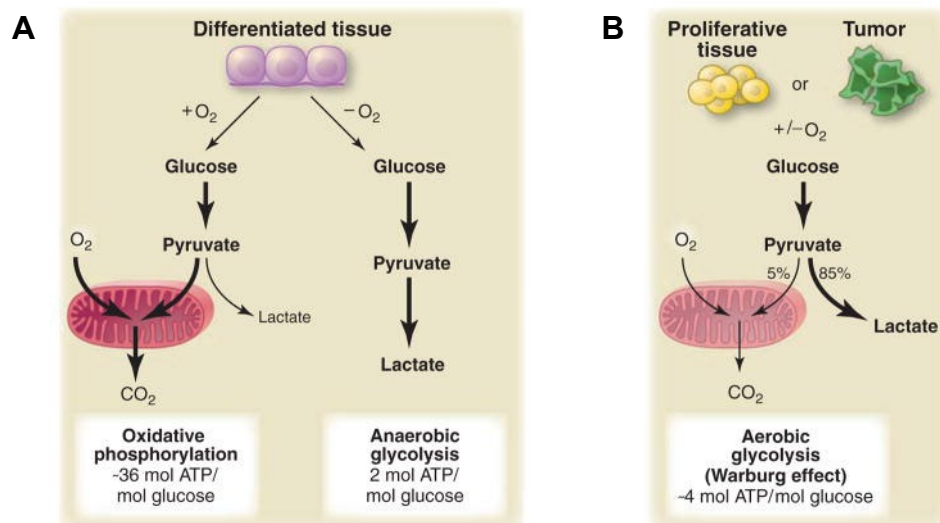


Figure 1.2: Visualization of the Warburg effect. Typical pyruvate utilization in differentiated cells is illustrated in **(A)**. Oxidative phosphorylation is the preferred and most efficient method of generating ATP. Only when oxygen is scarce will lactate fermentation occur, which generates substantially fewer ATP molecules. In highly proliferative cells such as cancer, the majority of pyruvate is allocated to lactate fermentation, regardless of oxygen presence **(B)**.

Reproduced with permission from: Vander Heiden MG, Cantley LC, Thompson CB. Understanding the Warburg Effect: The Metabolic Requirements of Cell Proliferation. *Science*. 2009;324(5930):1029-1033. (License number: 1049029-2)

Established MR-Based Techniques to Study Cancer Metabolism

This section from my first-authored review is reproduced with permission from:

Salzillo TC, Hu J, Nguyen L, Whiting N, Lee J, Weygand J, Dutta P, Pudakalakatti S, Millward NZ, Gammon ST, Lang FF, Heimberger AB, Bhattacharya PK. Interrogating Metabolism in Brain Cancer. *Magnetic Resonance Imaging Clinics of North America*. 2016;24(4):687-703. (License number: 1049029-3)

Detected Metabolites Using ^1H MRS/NMR

^1H MRS/NMR is extensively used to monitor the steady-state levels of major endogenous cellular metabolites. For a full review of *in vivo* ^1H MRS-detectable metabolites, see the following reference ³⁸. In the field of neuro-oncology, the most prevalent metabolites in the ^1H MR spectrum are N-acetylaspartate (NAA), total-choline-containing metabolites (Cho), lactate (Lac), mobile lipids (Lip), creatine (Cre), glutamate (Glu), glutamine (Gln), glutamine + glutamate (Glx), glycine (Gly), glutathione (GSH) and 2-hydroxyglutarate (2-HG). NAA shows the largest signal in normal healthy brain tissue and typically decreases in gliomas ³⁹. The Cho signal is a composite of free choline, phosphocholine (PC) and glycerophosphocholine (GPC), which are the precursors and breakdown products of the main membrane phospholipid phosphatidylcholine. The intensity of this peak is associated with cell proliferation and cell signaling and is typically elevated in cancer ⁴⁰. As previously mentioned, lactate is the end product of aerobic glycolysis and is enhanced in cancer as described by the Warburg effect. Lipids (long chain fatty acids), especially lipid droplets known as mobile lipids or triglycerides, are rarely observed in the normal brain

but are often increased in glial tumors and are associated with cell death and increased necrosis ⁴¹. The Cre signal is a composite of creatine and phosphocreatine (PCr), which are involved in energy metabolism via the creatine kinase reaction. Creatine levels vary within normal brain regions and in some cases with tumorigenesis ⁴². The amino acid Glu is the most abundant amino acid in the brain and an essential neurotransmitter. In gliomas, glutaminolysis is often required for tumor growth as an anaplerotic source of carbon complementary to glucose metabolism ⁴³. Recently, the oncometabolite 2-hydroxyglutarate (2-HG), which is produced in cells containing the isocitrate dehydrogenase (IDH) mutation, has been measured in patients with oligodendroglioma and astrocytoma tumors ⁴⁴.

Clinical ¹H MRS/NMR Spectroscopy

Numerous studies have highlighted the potential benefits of using ¹H MRS to estimate metabolite levels in brain tumors in the clinic ⁴⁵. When combined with similar spatial localization techniques that are used in generating anatomic MR images, this strategy can be used to produce maps of the variations in levels of Cho, Cre, NAA, Lac and Lip. With increased magnetic field strengths, improvements in scanner hardware and developments in software capabilities, the acquisition time for volumetric data is on the order of 5–10 minutes, and the spatial resolution of the voxels is typically 0.5–1 cm³ ⁴⁶. More recent advances in pulse sequence development and spectral editing schemes have facilitated the detection of metabolites with shorter T2 relaxation times and lower signal-to-noise (SNR) ratios such as Glu, Gln, Glx, and 2-HG, expanding the investigation of potential metabolic processes for both characterizing the spatial extent of gliomas and assessing therapeutic response.

For Tumor Characterization

The first studies to identify metabolic differences between gliomas and normal brain tissue date back to the mid-1990s and used a long TE (144 ms) ^1H MRS acquisition ^{47,48}. Since then, numerous studies have shown that elevated levels of Cho and reduced levels of NAA together can distinguish regions of tumor from normal brain ^{49,50}, define the spatial extent of abnormal metabolism due to tumor beyond the contrast-enhancing lesion ^{51,52}, guide the selection of biopsied tissue samples to the most aggressive part of the tumor ^{53,54}, and differentiate among tumor grades and types. The Cho-to-NAA index (CNI) is a metric that has been developed in the clinical setting to describe such changes and was found to be more robust than ratios and absolute quantification ⁵⁵. These *in vivo* results have been confirmed by correlating with both *ex vivo* histological characteristics from image-guided tissue samples and, more recently, ^1H high-resolution magic angle spinning of tumor biopsies to show that regions with elevated Cho and reduced NAA relative to normal brain have a high probability of corresponding to tumor ⁵⁴. However, despite the benefits of ^1H MRS in improving sensitivity to metabolically active tumor and differentiating gliomas from metastatic disease ⁵⁶, other disease processes such as inflammation can also cause a reduction in neuronal function while increasing cellularity, so alone ^1H MRS is not specific enough to differentiate tumor from inflammation ⁵⁷.

For Predicting Outcome or Response to Therapy

In high-grade gliomas, higher Cho-to-Cre, higher Cho-to-NAA, higher Lac-plus-Lip, and lower Cr-to-NAA abnormalities have been found to be associated with poor survival ⁵⁸. In low-grade gliomas, far less data are available on the prognostic value of

MRS in the clinic. In one study, normalized Cre was found to be a significant predictor for tumor progression and for malignant tumor transformation in grade II gliomas. Low-grade gliomas with decreased Cre appeared to have longer progression-free times and later malignant transformation than those with regular or increased Cre values ⁵⁹. The information provided by MRS data is complementary to anatomic images and may often be more valuable than the contrast-enhancing lesion in assessing therapeutic response. The spatial extent of the metabolic lesion can also be used to plan focal therapy, such as external beam radiotherapy and gamma knife radiosurgery ⁶⁰ as well as to assess the response to therapy ⁵⁰. For example, it was demonstrated that mean tumor Cho/NAA ratio and normalized Cho decreased from baseline after completion of external beam radiotherapy ⁶¹. In this study, patients who exhibited more than a 40% decrease in normalized Cho between mid- and post-radiotherapy studies were associated with shorter survival times and faster disease progression. The Lac/NAA ratio at the fourth week of radiotherapy and the change in normalized Cho/Cre between baseline and fourth week of radiotherapy were also predictive of outcomes, suggesting the possible benefit of adaptive, response-based radiation treatment.

Hyperpolarized Magnetic Resonance

Spin Polarization in MR

The major limitation of NMR/MRS is that it is inherently an insensitive technique relative to the ¹H concentration that is being measured. According to the nuclear

Zeeman effect, when an ensemble of nuclei is placed in a magnetic field, it will be split into two energy states according to their quantum spin when measured ⁶². These states are “spin up” (where the spins align parallel with the magnetic field) and “spin down” (where the spins align antiparallel with the field) ⁶³. The number of nuclei in each state are denoted N_- and N_+ , respectively, and as the “spin up” state is at lower energy, it contains slightly more nuclei than the “spin down” state. From the quantum mechanics framework, this is an overgeneralization as the spins technically exist in a linear combination of the two states, but for the sake of illustrating the concept for this project, this model should suffice. The population of the two states is governed by the Boltzmann distribution through the following equation.

$$\frac{N_+}{N_-} = e^{-\frac{\Delta E}{kT}} = e^{-\frac{\gamma \hbar B_0}{k_B T}} \quad \text{Equation 1}$$

Where ΔE is the energy difference between the states, γ is the gyromagnetic ratio of the nuclei, \hbar is the reduced Planck’s constant, k_B is the Boltzmann constant, and T is the temperature. Because the exponent is small at clinical magnet strengths and room temperature, this equation can be approximated by the first two terms of the Taylor expansion.

$$\frac{N_+}{N_-} \approx 1 - \frac{\gamma \hbar B_0}{k_B T} \quad \text{Equation 2}$$

Rearranging this equation yields:

$$\Delta N = N_- - N_+ = \frac{\gamma \hbar B_0}{k_B T} N_- \approx \frac{\gamma \hbar B_0}{k_B T} \left(\frac{1}{2} (N_- + N_+) \right) \quad \text{Equation 3}$$

Therefore, the ensemble polarization, P , is calculated by:

$$P = \frac{N_- - N_+}{N_- + N_+} \approx \frac{\gamma \hbar B_0}{2k_B T} \quad \text{Equation 4}$$

At clinical magnet strengths and room temperature, the ensemble polarization, which is proportional to the MR signal, is only a few parts per million (ppm). Therefore, the primary requirement to achieve an acceptable SNR for medical imaging is that a large concentration of nuclei must be measured. Fortunately, the concentration of water in the brain gray matter is approximately 40 M⁶⁴, so the low polarization is compensated for, allowing for the production of exquisite anatomic images.

Molecular and Metabolic MR

In order to detect a sufficient SNR from lower concentration molecules such as metabolites (which exist on the order of 10 mM in tissue), a large number of averages must be acquired, resulting in lengthy scan times. Thus, metabolites are often measured in “steady-state” where the pool size of the metabolite is reported as previously discussed in ¹H MRS studies. Alternatively, isotopically-enriched metabolic substrates (often ¹³C-labeled) can be infused into the subject, and the gradual incorporation of the label into its metabolic products can be measured over the course of several hours in a process known as stable isotope tracing^{65–67}. If the number of requisite averages to detect the label could be reduced by implementing a method to increase the polarization (and hence MR-signal of the substrate and products), the necessary scan time of these experiments could be vastly decreased, and accurate metabolic conversion rates could be measured in real-time. This is exactly what is achieved with a novel technique known as hyperpolarized magnetic resonance, which has found success over the past several years.

Hyperpolarization Techniques

There are four established hyperpolarization methods: brute force ^{68,69}, parahydrogen-induced ^{70,71}, optically-pumped ^{72,73}, and dynamic nuclear polarization (DNP) ^{74,75} (Fig. 1.3). DNP was exclusively used in this project. In this process, an isotopically-enriched metabolic substrate is doped with free electron radicals and cooled down to solid state at temperatures of a few kelvin. At these temperatures, the polarization of the electrons nearly reaches unity. The sample is then repeatedly irradiated with frequency-selective microwaves which transfers the polarization from the free electrons to the isotopically-enriched nuclei via the nuclear Overhauser effect ^{76,77}. The ensemble of nuclei is split into two distributions- a thermally polarized pool and a hyperpolarized pool- and the overall polarization of the ensemble represents a superposition of these states. Overall polarization levels of over 10,000-fold can be achieved with this process. However, what drove this technique to be clinically translatable was the engineering of a method to rapidly reheat and dissolve the hyperpolarized substrate into an injectable solution ⁷⁸. This process is known as dissolution DNP (dDNP), and Oxford Instruments engineered a preclinical system to reliably perform this procedure for academic research, which was used in this project. General Electric has recently manufactured a clinical-grade system called the SPINLab which adds processes to filter out toxic materials such as the free-radicals and to perform pharmacological quality assurance required for patient use.

(A) Solid State Dynamic Nuclear Polarization (DNP) **(B) Liquid State Para-hydrogen Induced Polarization (PHIP)**

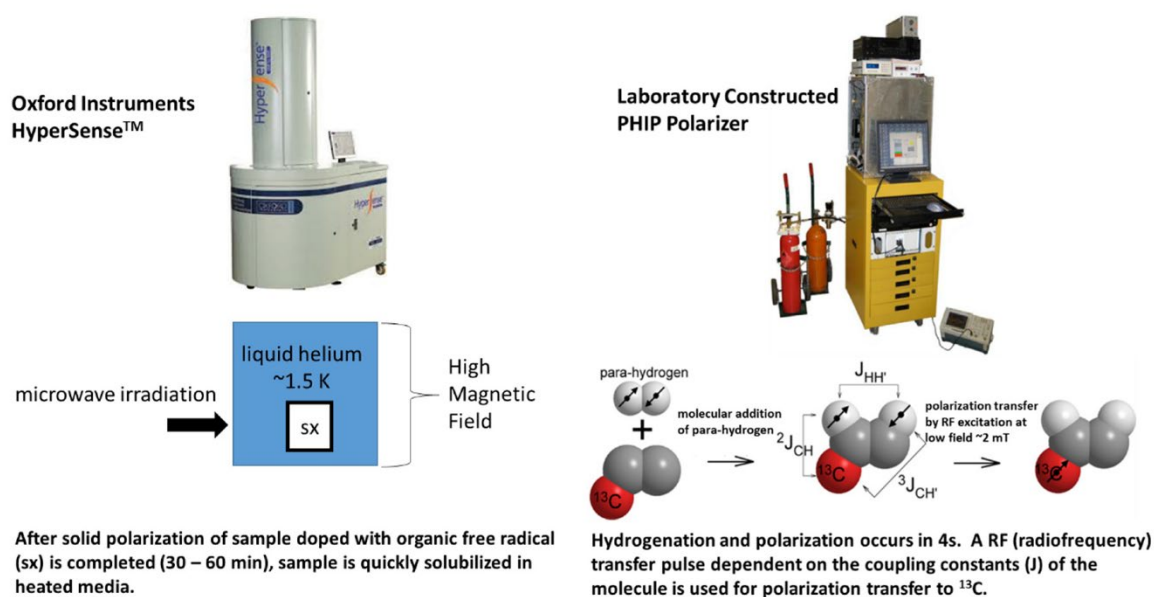


Figure 1.3: Instrumentation of two of the common hyperpolarization techniques. Dynamic nuclear polarization is illustrated in **(A)**, which is the most commonly used hyperpolarization technique and has been used in clinical trials. Parahydrogen-induced polarization is illustrated in **(B)**, which has found recent success in achieving high levels of polarization for a wide range of nuclei.

Reproduced from: Dutta P, Salzillo TC, Pudakalakatti S, Gammon ST, Kaiparettu BA, McAllister F, Wagner S, Frigo DE, Logothetis CJ, Zacharias NM, Bhattacharya PK. Assessing Therapeutic Efficacy in Real-time by Hyperpolarized Magnetic Resonance Metabolic Imaging. *Cells*. 2019;8(4):340. (Open access)

Hyperpolarization in MR

Because the hyperpolarized pool of nuclei is in a non-equilibrium state, the polarization will quickly begin to degrade once the sample is heated and removed from microwave irradiation, and eventually the ensemble of nuclei will be composed of only the thermally polarized pool whose polarization is described by Equation 4. The rate of this depolarization is equivalent to the T_1 relaxation of the ensemble, and thus different nuclei have unique hyperpolarized lifetimes⁷⁹. Additionally, once the

hyperpolarized solution is injected into a subject laying in the magnet, the process of exciting the nuclei with RF irradiation during imaging or spectroscopy and extracting the amplified signal results in the transfer of nuclei from the hyperpolarized pool to the thermally polarized pool (Fig. 1.4). This causes a fraction of the overall polarization of the ensemble of nuclei to be non-renewably depleted until the ensemble is composed entirely of the thermally polarized pool. The amount of depolarization is proportional to the RF power (and thus flip angle) used to excite the spins. Therefore, pulse sequences need to be carefully designed to quickly acquire data and avoid using large flip angles in order to optimally utilize the hyperpolarization of the sample.

Common pulse sequences used in hyperpolarized MR are either repeated single-voxel magnetic resonance spectroscopy (MRS) or multi-voxel magnetic resonance spectroscopic imaging (MRSI)^{80–82}. Single-voxel MRS is faster at acquiring each repeated excitation but contains no spatial distribution information. Multi-voxel MRSI has the advantage of producing parametric maps (usually of the metabolite signals or their exchange rates) but acquires repeated excitations at a slower rate and can suffer from distortions due to B0 and B1 inhomogeneity. Because there is typically sufficient SNR in one excitation to detect the hyperpolarized substrate and its metabolic products, spectra from repeated excitations can be stacked, rather than averaged. This allows the evolution of the hyperpolarized label to be measured in a cine-like manner with time resolutions of 2-10 s. The signal evolution of the injected substrate and its metabolites can be analyzed ratiometrically⁸³ or through kinetic modeling^{84,85} to inform on specific metabolic pathways *in vivo*.

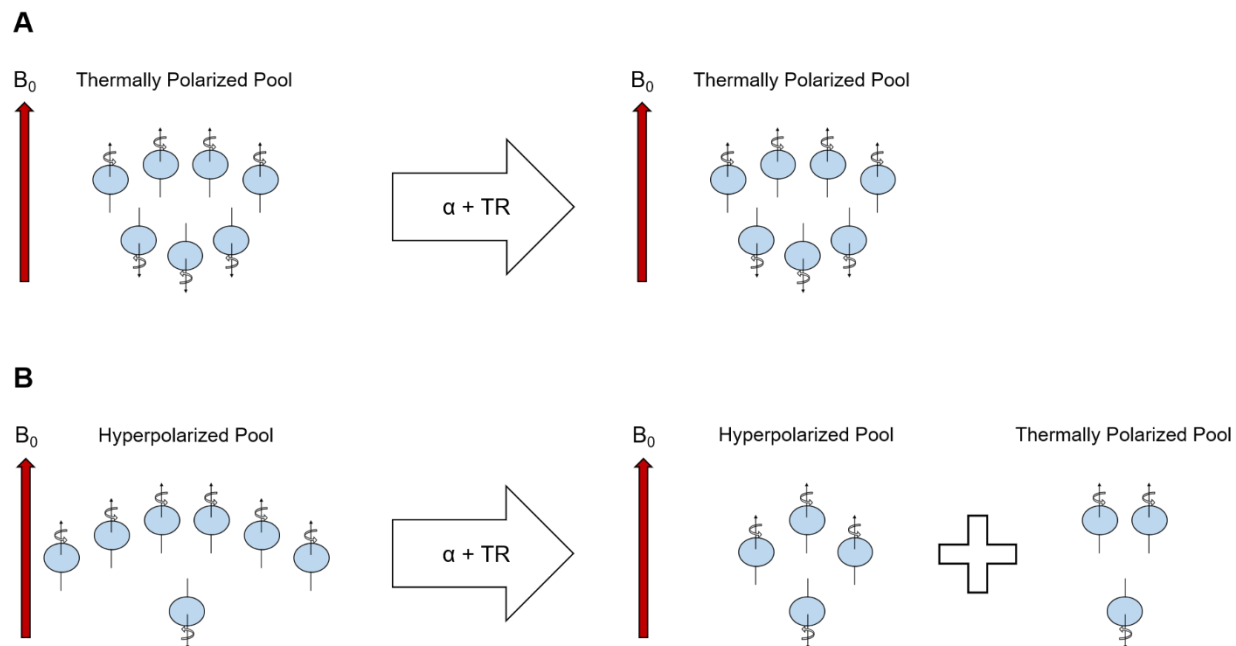


Figure 1.4: Polarization states during conventional and hyperpolarized MR experiments. During conventional MR experiments, the ensemble of nuclei is comprised of a thermally polarized pool which follows a Boltzmann distribution **(A)**. The polarization levels remain constant before and after a pulse sequence which contains an RF excitation pulse with flip angle, α , and repetition time, TR . During hyperpolarized MR experiments, the ensemble of nuclei is comprised of a hyperpolarized pool with some subset of nuclei left in the thermally polarized pool (not depicted) **(B)**. The overall polarization level is initially high, but it decreases throughout a pulse sequence due to both RF excitation and time between the excitations as nuclei equilibrate to the thermally polarized pool.

Existing Hyperpolarized MR Literature

There have been several reviews published on various metabolic substrates used in hyperpolarized MR ^{86,87} and their clinical applications of diagnosing a number of tumor types ⁸⁸ and measuring their response to therapy ^{89,90}. Pyruvate is the most commonly used hyperpolarized substrate due to its relatively long hyperpolarization lifetime and central role in tumor metabolism via the Warburg effect. There have been

several published preclinical studies using hyperpolarized [1-¹³C]pyruvate *in vivo* to distinguish brain tumors from healthy brain ^{91–95} as well as to measure the response of brain tumors to therapies such as radiotherapy ⁹⁶, temozolomide ⁹⁷, VEGF inhibitors ⁹⁸, and glycolytic inhibitors ⁹⁹. The success of these studies helped justify the initiation of several clinical trials for the use of hyperpolarized pyruvate in brain cancer, which have produced human data from healthy volunteers ^{100–102} and glioma patients ^{103–106}. Given the current advances, there is a strong likelihood that hyperpolarized pyruvate MR will be adopted in the clinic with FDA approval for metabolic imaging of brain cancer, and protocols for integrating this technique into the clinical workflow are underway ¹⁰⁷.

Dissertation Overview

The work presented in this dissertation was initiated with the goal of utilizing current and emerging MR technologies to study the metabolism of brain cancer and address several clinical challenges associated with the diagnosis and treatment of this disease. Specifics of the technologies and experimental methodologies used in this research are outlined in **CHAPTER 2**. Preliminary anatomic and metabolic data on a panel of patient-derived GBM xenograft mouse models are presented in **CHAPTER 3**. One of these mouse models was chosen for the bulk of this project, detailed in **CHAPTER 4**, which describes the anatomic and metabolic evolution of GBM as it progresses through tumor development, regression following radiotherapy, and eventual recurrence to the point of relapse. Lastly, supplemental data describing the metabolic profile of cancer-associated immune cells are presented in **CHAPTER 5**.

These data were produced in collaboration with several laboratories at MD Anderson and form the basis of a potential future project of measuring the metabolic response of immunotherapy in brain cancer.

CHAPTER 2:

GENERAL METHODS

Cell Lines

Glioma sphere-forming cells (GSC): GSCs were isolated from surgical samples from patients which have been reported in the literature ¹⁰⁸. The specific GSC lines that were selected for this project were 8-11, 262, 272, 231, 248, and 275. As reported in the literature ^{109,110}, cells were grown in Neurosphere Media containing DMEM/F12 (Corning) with B27 (x1, Thermo Fisher Scientific), bFGF (20 ng/ml, MilliporeSigma), and EGF (20 ng/ml, MilliporeSigma) at a temperature of 37° C. These cells were authenticated by the MDACC Cell Authentication Core.

(<https://www.mdanderson.org/research/research-resources/core-facilities/cytogenetics-and-cell-authentication-core.html>)

Animals

Mice: Five-week-old athymic nude mice (Experimental Radiation Oncology, MDACC) were used for *in vivo* studies. Mice were housed together in a sterilized facility with 5 to a cage, so only females were used as they are less-prone to fighting with each other. Mice received standard feed and water and were inspected for health daily. A guide-screw system was used for implantation to allow for consistent placement of intracranial xenografts as described in literature ¹¹¹. A 2.6 mm long guide screw with a 0.5 mm channel bored through its center was drilled into the skull directly over the caudate nucleus. After the mice had recovered for 2 weeks, 5×10^5 GSC 8-11 cells were suspended in 3 μ L of phosphate-buffered saline (PBS) and injected

stereotactically through the bore of the guide screw over a period of five minutes. After injection, a stylet was placed in the bore of the screw to close the system and prevent tissue from growing inside. Control animals were prepared in the same manner except that PBS absent of GSCs was injected. All procedures were performed in accordance with regulations of the Institutional Animal Care and Use Committee (IACUC) of the University of Texas MD Anderson Cancer Center.

Anatomic Magnetic Resonance Imaging

Tumor anatomy was visualized with MRI on a Bruker 7 T pre-clinical scanner (Bruker Biospin MRI GmbH) every 3 days. T1-weighted (T1-w), T2-weighted (T2-w), and fluid attenuated inversion recovery (FLAIR) ^1H pulse sequences were implemented. A 35 mm RF volume coil (Bruker) was used to acquire the images. The following pulse sequences and parameters were used:

- Coronal, sagittal, and axial T2-w (FA = 90° , TE = 6.5 ms, TR = 1500 ms, BW = 75 kHz, Matrix = 256 x 192, FOV = 25 mm x 25 mm (axial 20 mm x 20 mm), NEX = 4, Slice Thickness = 0.75 mm, Slice Gap = 0.25 mm, RARE Factor = 12)
- Axial T2-w FLAIR (FA = 90° , TE = 48 ms, TR = 10,000 ms, TI = 2000 ms, BW = 38 kHz, Matrix = 256 x 192, FOV = 20 mm x 20 mm, NEX = 3, Slice Thickness = 0.75 mm, Slice Gap = 0.25 mm, RARE Factor = 10, Fat Suppression on)
- Axial T1-w (FA = 90° , TE = 57 ms, TR = 3000 ms, BW = 85 kHz, Matrix = 256 x 192, FOV = 20 mm x 20 mm, NEX = 3, Slice Thickness = 0.75 mm, Slice Gap = 0.25 mm, RARE Factor = 4, Fat Suppression on)

Tumor Volume Measurements

DICOM images from the T1-w, T2-w, and FLAIR pulse sequences were imported into 3D Slicer software ¹¹². Tumors were segmented on each slice of the coronal, sagittal, and axial T2-w images. T1-w and FLAIR images were used to confirm tumor boundaries and differentiate tumor tissue from surrounding edema and cerebral spinal fluid. Volume in each plane of the T2-w images was calculated by multiplying the number of voxels within the tumor segmentation by the spatial dimensions of the voxels. The calculated volumes from each of the three T2-w imaging planes were averaged together to give the final volume measurement of the tumor. At least 5 tumor volumes were averaged at each time-point.

Hyperpolarized Sample Preparation

[1-¹³C]pyruvic acid (MilliporeSigma) was doped with Ox063 trityl radical (Oxford Instruments) to 15 mM concentration. 20 μ L of this solution was mixed with 0.4 μ L of 50 mM Gd³⁺ (Bracco Diagnostics). This solution was placed in a DNP HyperSense (Oxford Instruments) to polarize for approximately 1 hour under microwave irradiation at 94,100 GHz. An average polarization of 20,000 was achieved. Once the sample was prepared, it was rapidly heated and dissolved in 4 mL buffer comprised of 40 mM 2-Amino-2-(hydroxymethyl)-1,3-propanediol (TRIS; MilliporeSigma), 80 mM NaOH, 0.1 g/L ethylenediaminetetraacetic acid (EDTA; MilliporeSigma), and 50 mM NaCl. This solution had a final [1-¹³C]pyruvic acid concentration of 80 mM which was then injected intravenously through the tail vein of the mouse.

¹³C Magnetic Resonance Spectroscopy

A 72 mm ¹H volume coil (Bruker Biospin MRI GmbH) was used to acquire anatomic images for accurate region of interest (ROI) placement for spectroscopy. A ¹³C transmit/receive surface coil (Doty Scientific Inc) was placed above the skull, directly over the tumor. A ¹³C slice-selective, pulse-acquired spectroscopy sequence was prepared in which a single slice was placed over the tumor (FA = 25°, TE = 205 ms, TR = 2,000 ms, BW = 5 kHz, Matrix = 2048 x 64, FOV = 35 mm x 35 mm, NEX = 1, Slice Thickness = 6 mm, reference frequency = 75.515 MHz). Spectra were acquired every 2 seconds for 2 minutes to detect [1-¹³C]pyruvate and its lactate product.

Pyruvate-To-Lactate Measurements

The time-resolved stack of ¹³C MR spectra was imported into MATLAB (The MathWorks, Inc.). A freely-available MATLAB script courtesy of the Hyperpolarized MRI Technology Resource Center (Hyperpolarized-MRI-Toolbox. Available online at:

<https://github.com/LarsonLab/hyperpolarized-mri-toolbox>

DOI: 10.5281/zenodo.1198915) was used to analyze the spectra. This script was adapted so that each of the individual spectra in the time-resolved stack could be phase- and baseline-corrected individually, rather than as a sum. Following these corrections, the pyruvate and lactate peaks were integrated (full-width, quarter-max), and the integral values were summed across all spectra in the time-resolved stack. The metric for pyruvate-to-lactate conversion, denoted as nLac, was then calculated using these values as the ratio of lactate/(lactate+pyruvate). At least 5 nLac measurements from tumor-bearing mice were averaged at each time-point.

Additionally, N = 3 nLac measurements from control mice were averaged and compared with tumor-bearing mice at these time-points.

Brain Sample Excision

Mice were euthanized and the bolt and top of the skull were carefully removed to expose the brain. The optical tracts were severed, and the intact brain was excised. For samples to be processed for immunohistochemistry (IHC) analysis, the entire brain was placed and fixed in a vial containing 10% formalin.

For samples to be processed for NMR spectroscopy, incisions were made along the longitudinal and transverse fissures. The tissue within the left cerebral hemisphere (which contained the GSC injection site) was isolated from the remainder of the brain (which included the olfactory bulb, right cerebral hemisphere, and cerebellum). The isolated tissue was flash-frozen in liquid nitrogen and transferred to a freezer at -80°C. This process was executed as quickly as possible to preserve cellular metabolism, and the same volume of tissue was collected across all time-points, regardless of tumor size.

Sample Preparation for Metabolite Extraction

Metabolites were extracted from *ex vivo* samples as described in the literature ¹¹³. Frozen samples were pulverized and weighed. The tissue particles were transferred to a conical centrifuge tube containing 2 mL of methanol, 1 mL of water, and 0.5 mL of lysing beads. The samples were vortexed, flash-frozen, and thawed for 3 cycles to lyse the cells. The samples were then centrifuged at 4° C for 10 minutes, and the supernatant, which contained water, methanol, and dissolved metabolites, was

extracted. The methanol was evaporated under reduced pressure using a rotary evaporator, and the remaining solvent was freeze-dried using a lyophilizer. The dried product was dissolved in 600 μL of deuterium oxide, 36 μL of phosphate buffered saline, and 4 μL of 4,4-dimethyl-4-silapentane-1-sulfonic acid (DSS-d6) as the NMR reference standard (500 μM in solution). The final 640 μL solution was transferred to a 5 mm NMR tube. All supplies (deuterium oxide, DSS, phosphate buffer) were purchased from MilliporeSigma and used without further purification.

Nuclear Magnetic Resonance Spectroscopy

NMR spectra were obtained using a Bruker AVANCE III HD® NMR scanner (Bruker Biospin MRI GmbH) at a temperature of 298 K. The spectrometer operates at a ^1H resonance frequency of 500 MHz and is endowed with a triple resonance (^1H , ^{13}C , ^{15}N) Prodigy BBO cryogenic temperature probe with a Z-axis shielded gradient for increased sensitivity. A pre-saturation technique was implemented for water suppression. The spectra were obtained with a 90° pulse width, a scan delay t_{rel} of 6 s, a 10240 Hz spectral width, and an acquisition time t_{max} of 1.09 s (16,000 complex points). A total of 256 scans are collected and averaged for each spectrum, which resulted in a total scan time of 33 minutes. Here, $t_{\text{rel}} + t_{\text{max}}$ is nearly 8 s so that it exceeds $3 \cdot T_1$ for the metabolites observed. The time domain signal is apodized using an exponential function.

Metabolite Pool Size Measurements

The raw FID files from the spectrometer were imported into MestreNova software (Mestrelab Research) where they were Fourier transformed into chemical shift

spectra. The spectra were manually phase-corrected to form Lorentzian peak shapes and manually baseline-corrected to remove the noise floor, and the DSS reference peak was set to 0 ppm. The processed spectra were exported to Chenomx NMR Suite 8.1 software (Chenomx Inc.) where the peaks were identified by matching them to spectral models of metabolites contained in the database. The identified peaks were integrated in MestreNova, and the peak areas were normalized to the peak area of DSS. As described in the literature ¹¹⁴, these values were further normalized to the mass of the pulverized tissue (in mg) and converted to metabolite concentrations (in μM) by implementing the Beer-Lambert law. The final values were reported as $\mu\text{M}/\text{mg}$. Similar to the nLac measurements, there were $N = 5$ groups of measurements for tumors and $N = 3$ groups of measurements for healthy brain controls at each time-point.

Sample Preparation for Immunohistochemistry

Mice were sacrificed by intracardiac perfusion of PBS and 4% paraformaldehyde. Brains were removed, fixed in 10% formalin for at least 24 hours and embedded in paraffin. Sections ($5\ \mu\text{m}$) were cut for immunohistochemical analysis.

Immunohistochemistry

Sections of formalin-fixed paraffin-embedded mouse brain specimens were deparaffinized with xylene and rehydrated through a graded alcohol series, followed by distilled water and PBS. The slides were processed for antigen retrieval by pressure cooker in citrate buffer (pH 6.0) for 20 minutes. The slides were incubated overnight with the mouse antihuman monocarboxylate transporter 1 (MCT1) antibody

(Santa Cruz Biotechnology) at 1:200 dilution and rabbit antihuman lactate dehydrogenase-A (LDH-A) antibody (Abcam) at 1:100 dilution. For the MCT1 immunostaining, slides were incubated with Mouse Ig Blocking Reagent (Vector Laboratories) to reduce endogenous mouse Ig staining. The slides were rinsed with PBS and incubated with Anti-rabbit Poly-HRP-IgG (Leica Biosystems) and Polymer Anti-Mouse IgG reagent (Leica Biosystems) and visualized with 3,3'-Diaminobenzidine (DAB). The slides were counterstained with hematoxylin, dehydrated and coverslipped.

Protein Expression Measurements

The 40x images (1360 x 1024 pixels) of MCT1 and LDH-A stains were loaded into the FIJI package of ImageJ ¹¹⁵. Color deconvolution was performed ¹¹⁶ to extract the DAB stain from the image. These DAB images were thresholded so that DAB signal was set to 1 and everything else was set to 0. Three nonoverlapping, uniformly-sized ROI (340 x 256 pixels) were randomly placed in the tumor and one ROI outside the tumor as a background measurement. The percent area of DAB stain was calculated in these ROI (number of DAB-positive pixels divided by number of pixels in ROI). Percent area from the background ROI was subtracted from each of the tumor ROI which were then averaged together to produce the final metric for protein expression in that image. Average percent area from each image at a time-point were further averaged together to describe protein expression over the course of tumor development.

Statistical Analysis

All statistical analysis was conducted using GraphPad Prism 8 (GraphPad Software). All measurements are reported as the mean value \pm standard deviation, and error bars in the figures represent standard deviation. N represents the sample size for each group as a single number or range of values. Statistics are described in detail for each project in their respective sections.

CHAPTER 3:

PRELIMINARY ANTOMIC AND METABOLIC IMAGING OF A PANEL OF PATIENT-DERIVED GBM XENOGRAFTS

Motivation

Cancer is a heterogenous disease with varying phenotypes, even within the same type of cancer. In fact, within a tumor, there are heterogenous subregions of cells which possess varying mutational, proteomic, and metabolic profiles ^{117,118}. As a tumor grows and reacts to its microenvironment or other stimuli, dominant profiles emerge which can alter overall tumor behavior over time. This heterogeneity is what makes cancer so difficult to treat. Two patients can experience vastly different tumor evolutions and symptom development. Furthermore, these patients can respond to the same treatment completely differently. Even if the treatment is initially successful and drives the tumor into remission, the remnants of the tumor can adapt and develop resistance as its dominant profiles change which leads to recurrence and eventual relapse.

The Cancer Genome Atlas (TCGA) identified initially four subtypes of GBM which has since been narrowed down to three (classical, mesenchymal, and proneural) based on genetic and transcriptome analysis of over 600 GBM tumors ^{119,120}. This data has been analyzed to predict clinical outcomes of these subtypes such as overall survival and response to therapy ¹²¹. We wanted to take this one step further and determine tumor aggressiveness non-invasively with hyperpolarized MR. This proposal was motivated by a prior study in our laboratory which demonstrated that significant differences of hyperpolarized pyruvate-to-lactate

conversion and metabolite pool sizes existed between groups of patient-derived pancreatic xenograft murine models with varying median survival times ¹²².

In collaboration with the MD Anderson Brain Tumor Center and laboratory of Dr. Frederick Lang, we sought to produce orthotopic murine models of GBM from a panel of authenticated patient-derived glioma sphere-forming cell (GSC) lines. Six GSC lines were chosen which spanned the original four TCGA subtypes and were paired by median survival time of either one, three, or six months (unpublished data). These GSC lines were 8-11, 262, 272, 231, 248, and 275. Before ordering large cohorts of mice, preliminary imaging experiments were performed as a proof-of-concept. In addition to validating the nominal median survival and measuring rough growth curves to plan the timing of metabolic assays, we needed to establish that it was possible to detect sufficient hyperpolarized pyruvate and lactate signal from the brain tumors. Mouse vasculature, blood brain barrier permeability, tumor perfusion, MR coil setup, and MR pulse sequence parameters could all affect the signal detection.

Results

Preliminary Anatomic MRI and Hyperpolarized ^{13}C MRS Of GSC Tumor-Bearing Mice.

Tumor aggressiveness of each GSC line was verified by measuring the time-to-target-volume and survival of the tumor-bearing mice. Anatomic MRI was performed on the six groups of GSC tumor-bearing mice at various times throughout development. Tumor volume was calculated from these scans and plotted over time to form tumor growth curves (Fig. 3.1A). The maximum time to reach a target tumor volume of 25 mm³ for each GSC line is as follows: 28 days (8-11), 41 days (262), 40 days (272), N/A days (231), 152 days (248), and 195 days (275). Because the volume measurements are fairly sparse at the early time-points (due to scanner availability), the actual time to reach this volume could occur before these reported time-points.

Hyperpolarized MRS experiments were also performed in five of the six groups of GSC tumor-bearing mice (Fig. 3.1B). GSC 231 had abnormally low nLac values due to poor SNR. However, all but one of the remaining nLac measurements were greater than 0.3 with an average value of 0.40 ± 0.14 .

The mouse survival produced by each of the GSC lines is shown in Fig 3.1C. Some of the data is censored due to mouse euthanasia and tumor excision for *ex vivo* analysis. Median survival for each of the GSC lines is as follows: 34 days (8-11), 39 days (262), 59 days (272), N/A days (231), 154 days (248), and 203 days (275).

Many of the hyperpolarized MRS experiments were performed on different days, so the change in nLac over the course of tumor development was investigated by plotting nLac against time after implantation. However, the different GSC lines

produced varying survival times, so the same date after implantation corresponded to a unique point in tumor development for each GSC line. Thus, the day at which the hyperpolarized MRS experiments were performed was divided by the survival of the corresponding mouse in attempts to normalize the stage of tumor development between the GSC lines. Excluding the abnormally low nLac values in the GSC 231 tumor-bearing mice, nLac was plotted against this normalized tumor development time (Fig 3.1D), and it can be seen that all of the hyperpolarized MRS experiments were conducted at > 70% survival. A positive linear trend in nLac over time with a slope of 0.064 per 10% survival can be observed.

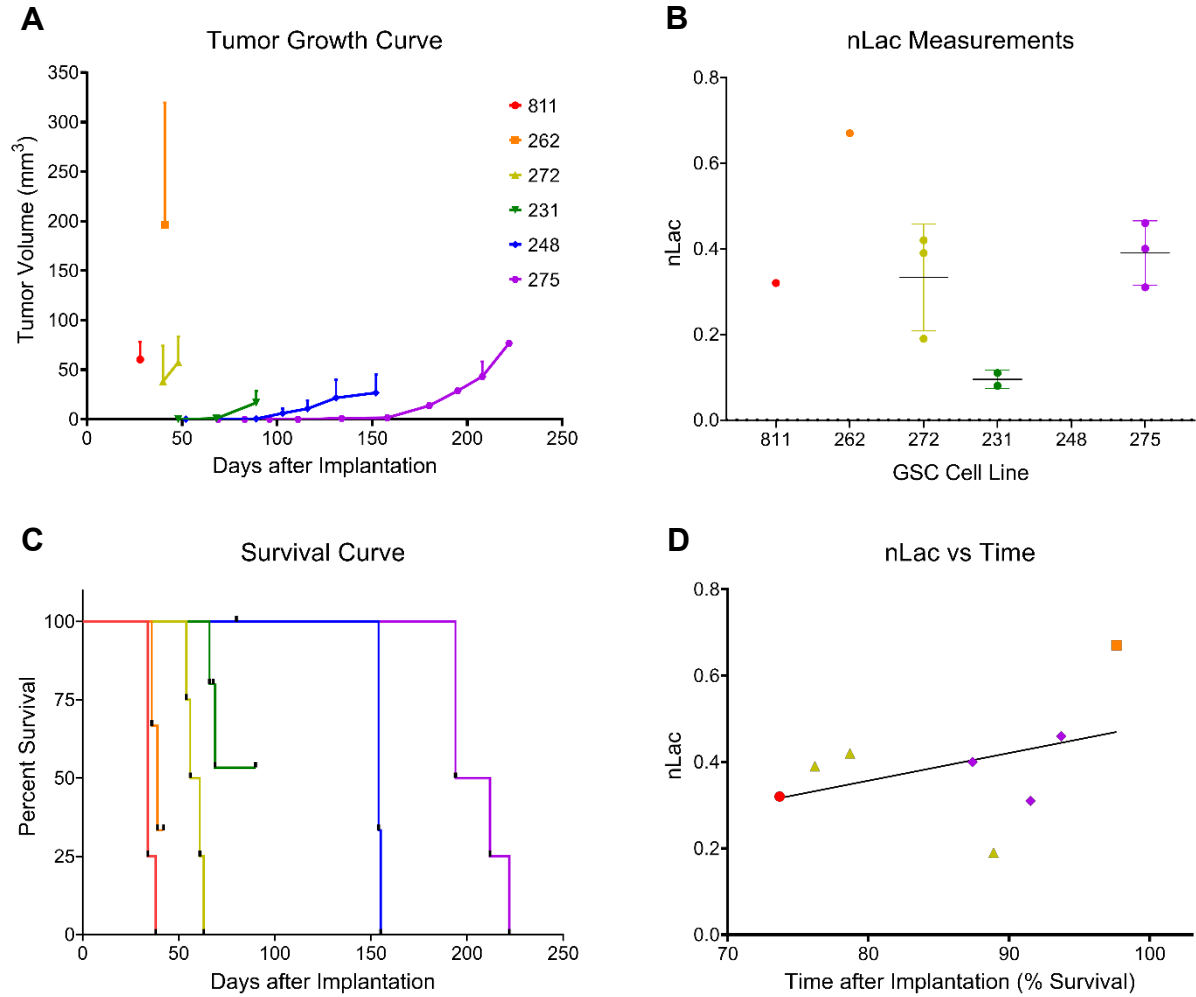


Figure 3.1: Preliminary anatomic MRI and hyperpolarized ^{13}C MRS of GSC tumor-bearing mice. Average tumor volume, measured from anatomic MRI, is plotted as a function of time for each of the GSC lines (**A**). Individual nLac values, measured with hyperpolarized ^{13}C MRS, are plotted for the different GSC lines (**B**). The survival curve for each of the GSC lines are plotted in (**C**). The time-points of each of the hyperpolarized MRS experiments in (**B**) were normalized to the survival of the corresponding mouse to convert the time-points from days to % Survival. Individual nLac values are plotted as a function of % Survival for the various GSC lines (**D**).

Discussion

While the number of data points for each GSC line was too sparse to conduct advanced statistical analysis, this preliminary project served its purpose as a proof-of-concept that pyruvate-to-lactate conversion could reliably be detected in brain tumors using our hyperpolarized MRS protocol. Furthermore, a general idea of the tumor growth rate and median survival of the GSC lines was gained. Collectively, these data allowed us to rank the aggressiveness of the GSC lines (from most aggressive to least: 8-11, 262, 272, 231, 248, 275), so an *a priori* hypothesis of how the nLac data would vary among the different lines could be formed. Lastly, this preliminary project provided me with the experience with these experimental methods to have confidence to perform them independently and understand their challenges so that I could optimally design my experiments and troubleshoot any potential errors.

Following this initial analysis of the six GSC models, the goal was to expand the sample size of each group of mice in order to establish statistical power for the original hypothesis: that measuring tumor metabolism with hyperpolarized MRS and NMR spectroscopy could predict GBM tumor aggressiveness. An *a priori* power analysis was conducted using a power of 0.8, Type I error probability of 0.05, and effect size which was estimated from the hyperpolarized MRS and NMR spectroscopy data acquired in the aforementioned pancreatic cancer project ¹²². Significant differences between any of the two groups for the hyperpolarized MRS experiments were expected with a sample size of 3, and between 2 and 6 for the various metabolites from the NMR spectroscopy experiments. Thus, it was planned to include N = 5 mice per group.

When performing these experiments on GSC models with varying survival times, an imperative factor to consider is at what point during tumor development to acquire these measurements to ensure that the results are comparable between GSC models. In other words, at what time does tumor metabolism stabilize so that it is possible to accurately compare the results between GSC models without having the stage of tumor development confound the results? Many studies pick an arbitrary time-point during development to perform these experiments. Alternatively, other reports wait until the tumor is an arbitrary size to conduct the metabolic imaging experiments. However, a common size among different GSC lines does not ensure that they will also possess same metabolic maturity.

The positive linear trend of nLac that was observed in Fig. 3.1D was particularly interesting because it suggested that conversion of hyperpolarized pyruvate to lactate was increasing throughout the latter half of tumor development. I wondered if this trend could be extrapolated back to early tumor development. This marked a major crossroads for my PhD project. If changes in tumor metabolism could not be detected with hyperpolarized MR and NMR spectroscopy throughout tumor development, then a metabolic equilibrium should exist such that I could choose a time-point to confidently compare the results between GSC lines, and I could attempt to predict tumor aggressiveness through these modalities as originally intended. However, if significant changes in tumor metabolism could be detected with hyperpolarized MR and NMR spectroscopy throughout tumor development, then alternative clinical applications of this technology could be explored such as early detection of GBM malignancy or improving diagnostic and prognostic capabilities. Furthermore, this

longitudinal approach of studying the metabolic evolution of these tumors could also be applied to investigate post-therapy events such as tumor regression and eventual recurrence.

Therefore, the theme of this project transformed from measuring the metabolic differences between several GSC lines at one time-point to measuring the metabolic evolution of one GSC line at several time-points. GSC 8-11 was chosen from this panel of tumors because it was a highly aggressive cell line, and existing data (unpublished) demonstrated that the tumors responded relatively well to radiotherapy. Taking time as a common dimension, the individual development of tumor anatomy and metabolism as well as their interrelationship could be studied throughout all stages of tumor progression. This led to the formation of the central hypothesis of my Ph.D. project along with the specific aims to test it.

Central Hypothesis, Specific Aims, and Rationale

Central Hypothesis: Throughout each stage of glioblastoma progression (development, regression, and recurrence), significant metabolic changes of the tumor can be detected prior to significant anatomic changes.

Specific Aim 1: Track the anatomic and metabolic evolution of GBM during tumor development. Following orthotopic GBM cell implantation, the mice will be imaged periodically with conventional anatomic MRI pulse sequences to measure tumor volume over time. Then at specific time-points throughout tumor development, hyperpolarized MRS experiments will be performed to measure the dynamic conversion of pyruvate to lactate *in vivo*. Following hyperpolarized MRS experiments, tumors will be excised and prepared for global metabolomic analysis with NMR and IHC.

Specific Aim 2: Administer radiation therapy to GBM and measure the anatomic and metabolic response during tumor regression. At around 75% through tumor development, radiation therapy will be delivered to the brains of tumor-bearing mice. Tumor volume and pyruvate-to-lactate conversion will then be measured throughout tumor regression as described in SA 1. Tumors will again be excised following hyperpolarized MRS experiments for global metabolomic analysis.

Specific Aim 3: Monitor the anatomic and metabolic states of regressed GBM tumors to the point of relapse. Following tumor regression from radiation therapy, mice will be imaged each week to measure tumor volume and pyruvate-to-lactate

conversion until the eventual recurrence of the tumor. Tumors will not be excised for this aim in order to produce longitudinal measurements of the same mouse.

Rationale: If metabolic changes in these aggressive tumors could be detected more rapidly than anatomic changes, then physicians could augment their existing protocols with these techniques to achieve several clinical benefits. In addition to the aforementioned possibilities of early detection of malignancy and improved diagnostic and prognostic capabilities, current challenges include distinguishing pseudoprogression from true progression following therapy, rapidly quantifying treatment response, and predicting recurrence. During tumor development, early detection of malignant transformation would allow physicians to administer therapy sooner while the tumor is less invasive and in a more treatable state, leading to improved patient outcomes. Assessing true tumor response shortly after the administration of therapy would provide physicians with the information of whether a treatment was effective, giving them more time to shift their strategy if the tumor continued to progress. Lastly, detecting early tumor recurrence during follow-up exams before the patient fully relapses would allow physicians to take early corrective action before the recurrent tumor becomes unmanageable. In each stage of tumor progression, detecting alterations in metabolic activity prior to anatomic changes in these aggressive cancers would ultimately improve the chance of patient survival.

CHAPTER 4:

MEASURING THE METABOLIC EVOLUTION OF GLIOBLASTOMA THROUGHOUT TUMOR DEVELOPMENT, REGRESSION, AND RECURRENCE WITH HYPERPOLARIZED MAGNETIC RESONANCE

Introduction

There is still much to be explored to determine how hyperpolarized MR can impart a positive clinical impact in the treatment of brain tumors. The aforementioned preclinical studies discussed in **INTRODUCTION** (Chapter 1) do a thorough job of elucidating differences in pyruvate utilization between tumors and healthy brain or between untreated and treated tumors, but they only do so at one point during development or with one pre- and post-treatment measurement. Tumor metabolism is heterogeneous and evolves over the course of tumor development suggesting that the time-point of the measurement can significantly impact the results ^{123–125}. Following treatment, metabolism is similarly dynamic as it responds to therapeutic insults before gaining resistance or re-growing. This complex metabolic trajectory cannot be captured with one post-treatment measurement alone. Therefore, we sought to implement for the first time, a series of serial hyperpolarized MRS measurements at multiple time-points over the course of tumor growth and treatment regimen. *In vivo* hyperpolarized pyruvate-to-lactate conversion values were obtained at multiple time-points throughout three stages of tumor progression (development, regression following radiotherapy, and recurrence to the point of relapse). Additionally, the novel use of hyperpolarized MRS to assess brain tumor recurrence, which is an unfortunate and inevitable reality for most GBM patients, could improve patient

survival by informing physicians when additional treatment is necessary before the tumor aggressively regrows ^{126,127}.

The purpose of this study was to compare hyperpolarized pyruvate-to-lactate conversion values from the serial hyperpolarized MRS experiments with tumor volume changes that were acquired with anatomic MRI during each stage of tumor progression (Fig. 4.1). This analysis was performed to demonstrate the value of adding hyperpolarized MR to conventional imaging protocols by addressing several challenges commonly encountered in the clinical setting. Furthermore, we sought to form a more complete picture of the metabolic events occurring throughout tumor progression by performing global metabolomics with NMR spectroscopy and protein expression assays with IHC on *ex vivo* tumor samples at multiple time-points. Lastly, correlative analysis was performed to investigate the interrelationship of each of these measurements over time.

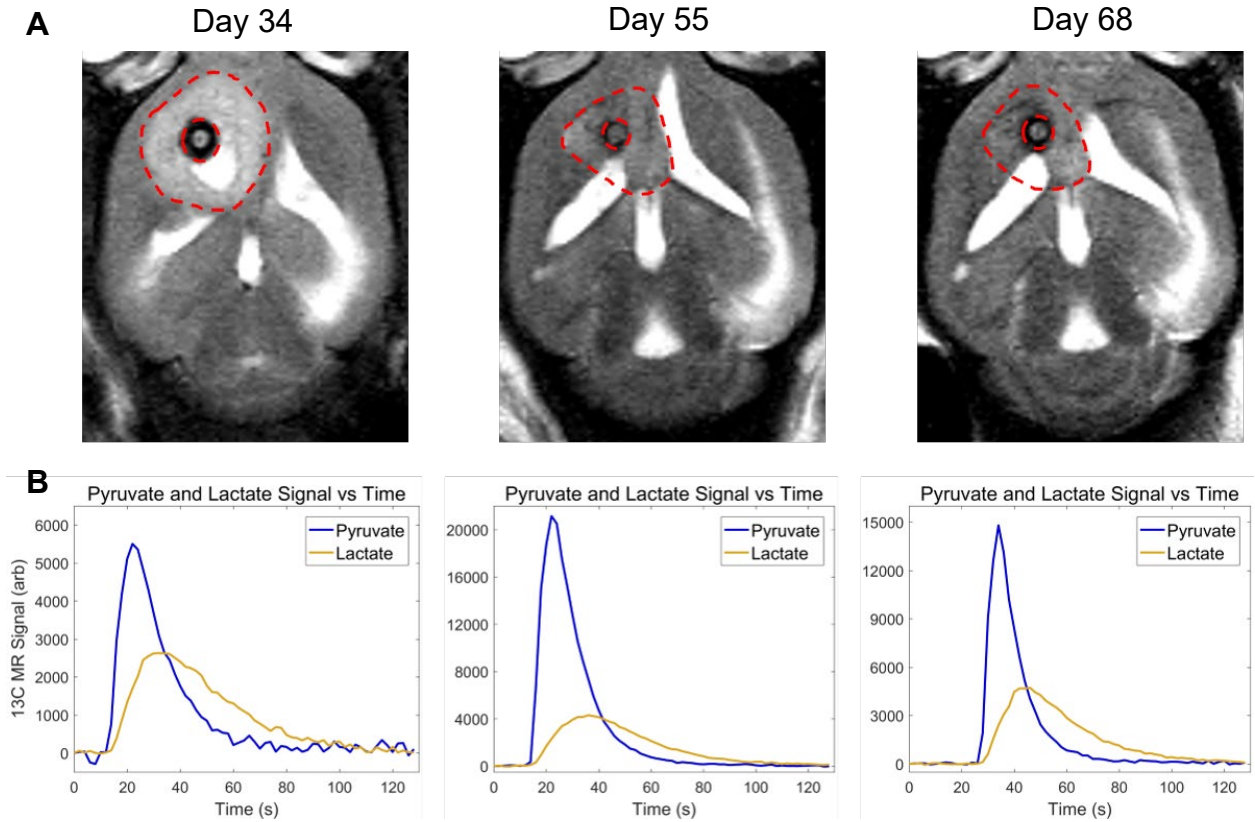


Figure 4.1: Anatomic and metabolic imaging of tumor-bearing mice over time. Tumor volume **(A)**, imaged with T2-weighted MRI, and pyruvate-to-lactate conversion **(B)**, measured with hyperpolarized MRS, is displayed at the end of tumor development (Day 34), end of tumor regression (Day 55), and at the point of relapse (Day 68) in the same mouse.

Methods

Refer to **GENERAL METHODS** in Chapter 2 for detailed discussion of experimental methods. Specific methods for this project are given below.

Experimental Overview

Following the intracranial implantation of patient-derived GSCs, the anatomic and metabolic properties of this GBM model were interrogated at several time-points during three stages of tumor progression: tumor development, regression following radiotherapy, and eventual recurrence. Mice were split into three cohorts: untreated tumor-bearing mice, treated tumor-bearing mice (2x5 Gy radiotherapy), and control mice. Anatomic growth and shrinkage were studied *in vivo* with T1-weighted, T2-weighted, and fluid-attenuated ¹H MRI. Real-time conversion of injected pyruvate to lactate was measured in the tumor *in vivo* with hyperpolarized ¹³C MRS. *Ex vivo* metabolite pool sizes and protein expression were determined with NMR spectroscopy and IHC, respectively. All measurements were acquired within ± 1 day of their nominal time-point.

Tumor Radiotherapy

Tumor-bearing mice in the treatment cohort underwent radiotherapy to attenuate tumor growth. On Days 25 and 27, the mice were imaged and treated with 5 Gy whole-brain irradiation on the X-RAD SmART small animal irradiator (Precision X-Ray). A cone-beam CT was acquired for treatment planning, and irradiation was executed with two opposing fields of 2.5 Gy each.

Statistical Analysis

All statistical analysis was conducted using GraphPad Prism 8 (GraphPad Software). All measurements are reported as the mean value \pm standard deviation, and error bars in the figures represent standard deviation. N represents the sample size for each group as a single number or range of values.

Median Survival Time: Kaplan-Meier analysis was used to compare the median survival of untreated (N = 102) and treated (N = 59) tumor-bearing mice. Specifically, the Mantel-Cox logrank test was used to test for significant differences between median survival times, and the logrank method was used to calculate the hazard ratio.

***In Vivo* Tumor Volume Measurements:** In untreated tumors during development, average volume at each time-point (N = 5-10) was compared with baseline average volume measured on Day 5 (N = 6). In treated tumors following radiotherapy, average volume at each time-point (N = 5-10) was compared with average volume at time of treatment on Day 26 (N = 8) as well as to maximum average volume (N = 10). Volume data was log-transformed to correct for heteroscedasticity and tested for significant differences using ordinary one-way ANOVA and follow-up Fisher's Least Significant Differences tests ($p < 0.05$) where p is the probability value.

Repeated measures of individual tumor volume values in treated tumor-bearing mice were further analyzed using mixed-effects analysis with the Geisser-Greenhouse correction as an additional check for significant changes.

***In Vivo* Pyruvate-to-Lactate Measurements:** During tumor development, average nLac of untreated tumors (N = 5) were compared with average nLac of controls

(N = 3) at each time-point. In treated tumors, average nLac at each time-point (N = 5-8) was compared with average nLac at all prior time-points as well as to average nLac of untreated tumors and controls on Days 28 and 34. Statistical significance was determined using ordinary one-way ANOVA and follow-up Fisher's Least Significant Difference tests ($p < 0.05$).

Repeated measures of individual nLac values in treated tumor-bearing mice were further analyzed using mixed-effects analysis with the Geisser-Greenhouse correction as an additional check for significant changes.

Ex Vivo Metabolite Pool Size Measurements: During tumor development, average metabolite pool sizes of untreated tumors (N = 5-7) were compared with average metabolite pool sizes of normal brain tissue controls (N = 3) at each time-point. In treated tumors, average metabolite pool sizes at each time-point (N = 5) were compared with average metabolite pool sizes at all prior time-points as well as to average metabolite pool sizes of untreated tumors and controls on Days 28 and 34. Statistical significance was determined using ordinary one-way ANOVA and follow-up Fisher's Least Significant Difference tests. Due to the large number of comparisons (each set of comparisons made for 26 metabolites), the false discovery rate was controlled using the two-stage step-up method of Benjamini, Krieger and Yekutieli ($Q < 0.05$).

Ex Vivo Protein Expression Measurements: During tumor development, average background-subtracted percent stained area (MCT1 and LDH-A) from 3 ROI in each 40x capture (N = 1-5) from untreated tumors was compared at each time-point as well

as with healthy brain controls. Statistical significance was determined using ordinary one-way ANOVA and follow-up Fisher's Least Significant Difference tests ($p < 0.05$).

Inter-experiment Correlations: In the subset of mice in which anatomic MRI, hyperpolarized MRS, and NMR experiments were each performed at a particular time-point, tumor volume, nLac, and metabolite pool sizes were directly correlated with one another. Pearson correlation coefficients were calculated for the following combinations: logarithm of tumor volume and nLac ($N = 59$), logarithm of tumor volume and metabolite pool sizes ($N = 34$), nLac and metabolite pool sizes ($N = 47$), and the individual metabolite pool sizes with one another ($N = 70$). R^2 values were reported from these correlation coefficients and deemed statistically significant if $p < 0.05$.

Specific Aim 1: Track the Anatomic and Metabolic Evolution of GBM During Tumor Development

Results

Tumor Volume (*in vivo*): Following GSC implantation, average tumor volume was assessed every 3-4 days with T1-weighted, T2-weighted, and fluid-attenuated MRI (Fig 4.2). An initial baseline volume of $1.4 \pm 0.5 \text{ mm}^3$ was measured on Day 5. Average tumor volume experienced exponential growth ($R^2 = 0.60$), increasing slowly at first before rapidly expanding on Day 21 where it nearly tripled from the prior time-point to a value of $15.2 \pm 9.7 \text{ mm}^3$. At a value of $3.5 \pm 0.9 \text{ mm}^3$, average tumor volume was significantly increased by Day 10 compared with baseline volume ($p = 0.0282$). By the endpoint of tumor development (Day 34), average untreated tumor volume was $88.6 \pm 56.3 \text{ mm}^3$.

Hyperpolarized pyruvate-to-lactate conversion (*in vivo*): Using hyperpolarized ^{13}C MRS, pyruvate-to-lactate conversion, quantified by nLac, was measured in tumor-bearing mice and control mice every 7 days with an extra measurement on Day 10 to capture early tumor dynamics (Fig. 4.3). nLac is defined as the ratio of lactate/(lactate+pyruvate) where lactate and pyruvate are the area-under-the-curve values calculated from the time-resolved ^{13}C spectra. Starting on Day 14, average nLac was significantly increased in tumor-bearing mice compared with control mice (0.39 ± 0.16 vs. 0.26 ± 0.10 , $p = 0.0273$) which persisted throughout the remaining time-points in tumor development. In tumor-bearing mice, average nLac increased with a significantly nonzero slope (0.0069 days^{-1} , $p = 0.0006$) to a final value of 0.45

± 0.09 on Day 34. In contrast, average nLac in control mice remained constant across all time-points (slope = 0.0005 days^{-1} , $p = 0.7674$), at an average value of 0.26 ± 0.07 .

Metabolite pool size (ex vivo): Tumors and controls (healthy murine brain tissue) were excised at the same time-points as the hyperpolarized MRS experiments for *ex vivo* global metabolomics using NMR spectroscopy. Pool sizes of 26 metabolites were quantified and compared between tumors and controls in the same manner as nLac (Fig. 4.4, 4.5). By Day 28, average pool size of the metabolites alanine (3.92 ± 1.55 vs. $1.54 \pm 0.61 \text{ } \mu\text{M/mg}$, $q = 0.0366$) and phosphocholine (3.14 ± 1.62 vs. $1.32 \pm 0.49 \text{ } \mu\text{M/mg}$, $q = 0.0491$) were significantly increased in tumors compared with controls. On Day 34, average pool sizes of alanine (4.80 ± 1.98 vs. $1.45 \pm 0.97 \text{ } \mu\text{M/mg}$, $q = 0.0027$) and phosphocholine (3.40 ± 1.23 vs. $1.17 \pm 0.64 \text{ } \mu\text{M/mg}$, $q = 0.0144$) were still significantly increased in tumors compared with controls along with glycerophosphocholine (3.19 ± 1.14 vs. $0.93 \pm 0.34 \text{ } \mu\text{M/mg}$, $q = 0.0343$), glycine (10.56 ± 6.53 vs. $2.86 \pm 2.01 \text{ } \mu\text{M/mg}$, $q = 0.0106$), and valine (0.81 ± 0.43 vs. $0.28 \pm 0.20 \text{ } \mu\text{M/mg}$, $q = 0.0072$).

Protein Expression (ex vivo): IHC was performed on *ex vivo* tumor samples at several time-points to measure changes in MCT1 and LDH-A expression throughout tumor development (Fig. 4.6). MCT1 is a membrane-bound protein responsible for shuttling monocarboxylates such as pyruvate into the cell. LDH-A is the enzyme responsible for converting intracellular pyruvate into lactate. Qualitatively, MCT1 was membrane-bound and LDH-A was confined to the cytoplasm, as expected. Semi-quantitatively, average MCT1 percent stained area was significantly higher in untreated tumors by Day 21 compared with controls (13.43 ± 5.33 vs. 3.11 ± 3.57 , p

= 0.0139; 13.43 ± 5.33 vs. 2.73 ± 1.98 , $p = 0.0110$) and remained significantly increased through Days 25, 28, and 34. Additionally, average MCT1 percent stained area was significantly higher in untreated tumors by Day 21 compared with untreated tumors early in development on Day 10, (13.43 ± 5.33 vs. 5.15 ± 4.86 , $p = 0.0459$) and remained significantly increased through Days 25, 28, and 34. Conversely, average LDH-A percent stained area was elevated in untreated tumors at all time-points of development, and the only significant increase was on Day 34 when compared with Days 14 (37.15 ± 5.48 vs. 19.77 ± 6.88 , $p = 0.0002$), 25 (37.15 ± 5.48 vs. 23.86 ± 5.52 , $p = 0.0030$), and 28 (37.15 ± 5.48 vs. 20.24 ± 12.81 , $p = 0.0008$).

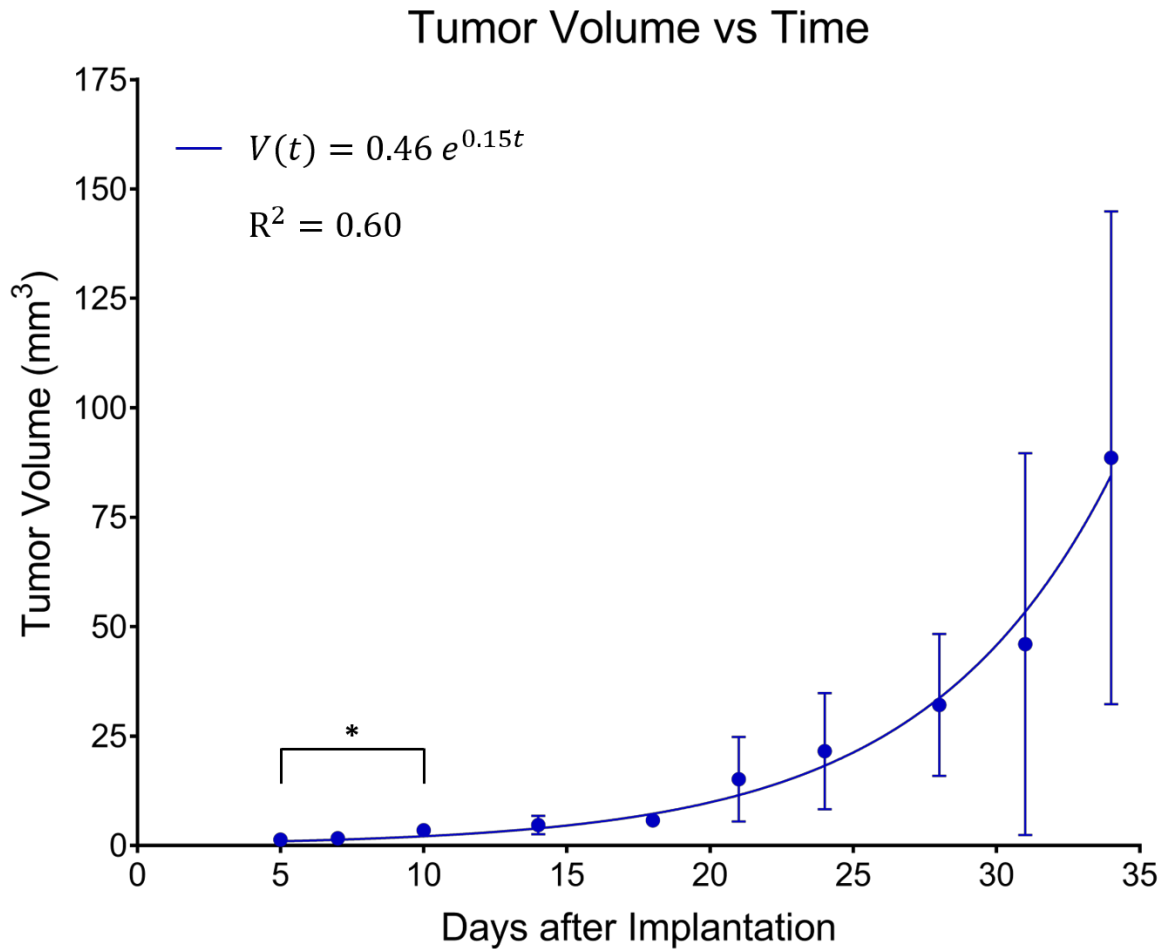


Figure 4.2: *In vivo* tumor volume significantly increases throughout tumor development. Average tumor volume, measured from anatomic MRI, is plotted as a function of time in untreated mice. An exponential function was fit to the data which is represented by the blue line. Error bars represent standard deviation (not visible before Day 21 due to scale of Y-axis). These values were log-transformed to correct for heteroscedasticity and tested for significant differences using ordinary one-way ANOVA and follow-up Fisher's Least Significant Differences tests. Comparisons that produced $p < 0.05$ were deemed significant. * $p < 0.05$.

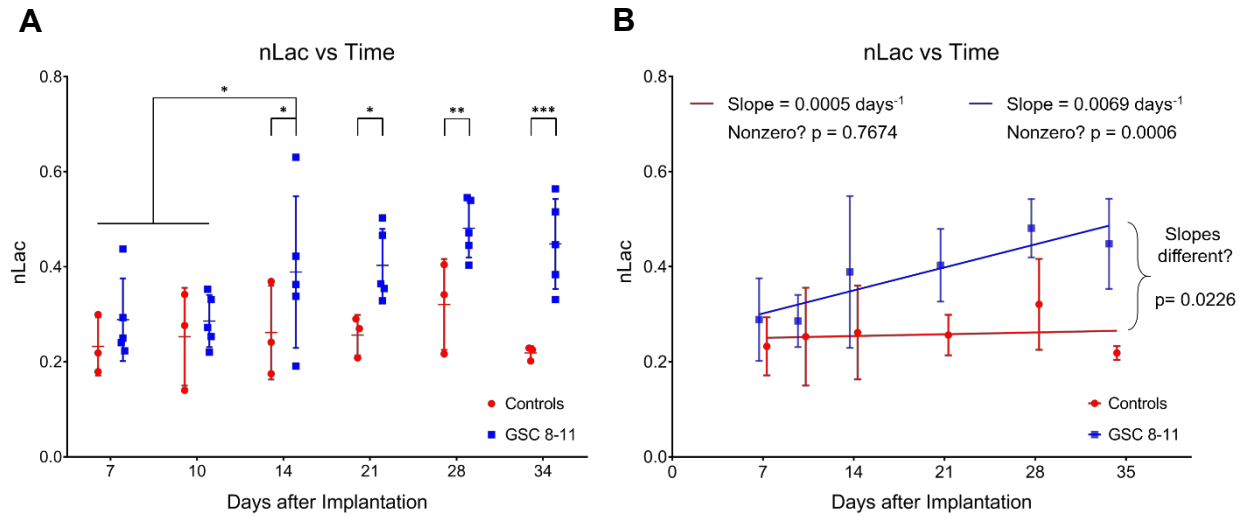


Figure 4.3: *In vivo* pyruvate-to-lactate conversion significantly increases throughout tumor development. nLac values, measured with hyperpolarized ^{13}C MRS, are plotted as a function of time for control mice (red circles) and untreated tumor-bearing mice (blue squares) during tumor development. Individual nLac values for each time-point are plotted in **(A)**. Statistically significant changes of nLac between untreated tumor-bearing and control mice for a particular time-point as well as between untreated tumor-bearing mice at different time-points are illustrated. Average nLac values between groups and time-points were assessed for significance using ordinary one-way ANOVA and follow-up Fisher's Least Significant Difference tests. Average nLac values for each time-point are plotted in **(B)** along with a linear fit of the data for untreated tumor-bearing mice and controls. The slopes of the linear fits are depicted in addition to the p-values from the comparisons of whether the slopes were significantly greater than zero as well as whether they were significantly different from each other. Linear regression was performed to calculate linear fits with each replicate considered, and slope values were tested for significance with the F-test (to test against a slope value of 0) or two-tailed T-test (to test the slope values against each other). Error bars represent standard deviation. Significance attributed to comparisons that produced $p < 0.05$. * $p < 0.05$, ** $p < 0.01$, *** $p < 0.001$.

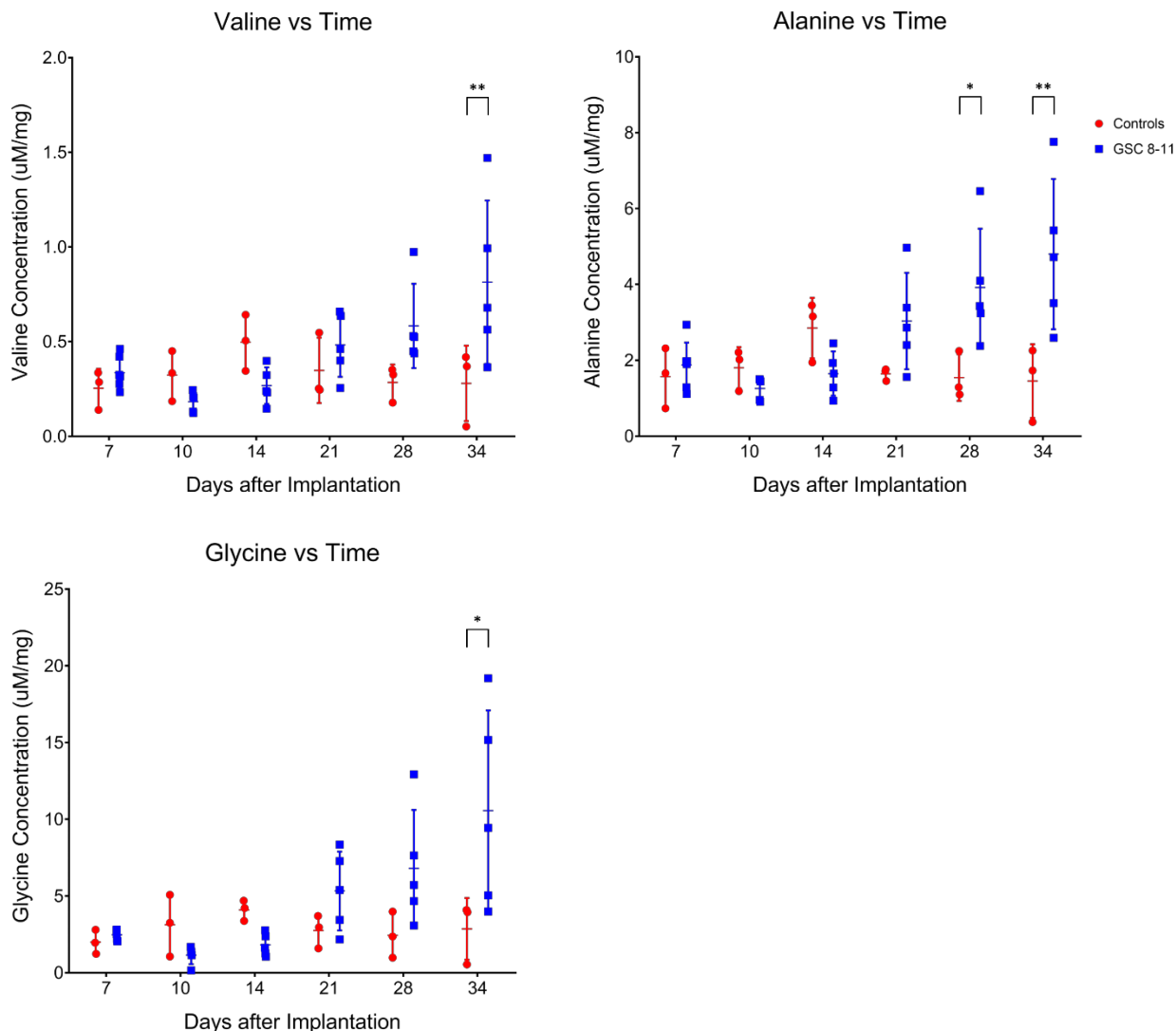


Figure 4.4: *Ex vivo* metabolite pool sizes significantly increase throughout tumor development (Part 1). Individual metabolite pool sizes, measured with NMR spectroscopy, are plotted as a function of time for control mice (red circles) and untreated mice (blue squares). Error bars represent standard deviation. The Y-axis is reported as concentration of metabolite pool per mg of tissue. Statistical significance was determined using ordinary one-way ANOVA and follow-up Fisher's Least Significant Difference tests. The false discovery rate was controlled using the two-stage step-up method of Benjamini, Krieger and Yekutieli, and significance was attributed to comparisons that produced $q < 0.05$. * $q < 0.05$, ** $q < 0.01$.

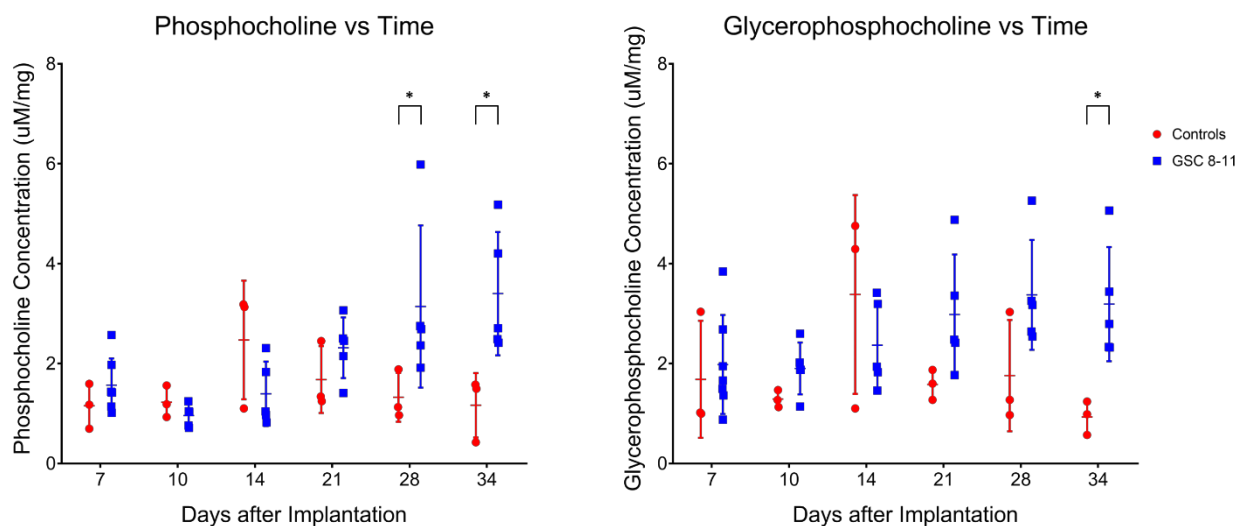


Figure 4.5: *Ex vivo* metabolite pool sizes significantly increase throughout tumor development (Part 2). Individual metabolite pool sizes, measured with NMR spectroscopy, are plotted as a function of time for control mice (red circles) and untreated mice (blue squares). Error bars represent standard deviation. The Y-axis is reported as concentration of metabolite pool per mg of tissue. Statistical significance was determined using ordinary one-way ANOVA and follow-up Fisher's Least Significant Difference tests. The false discovery rate was controlled using the two-stage step-up method of Benjamini, Krieger and Yekutieli, and significance was attributed to comparisons that produced $q < 0.05$. * $q < 0.05$.

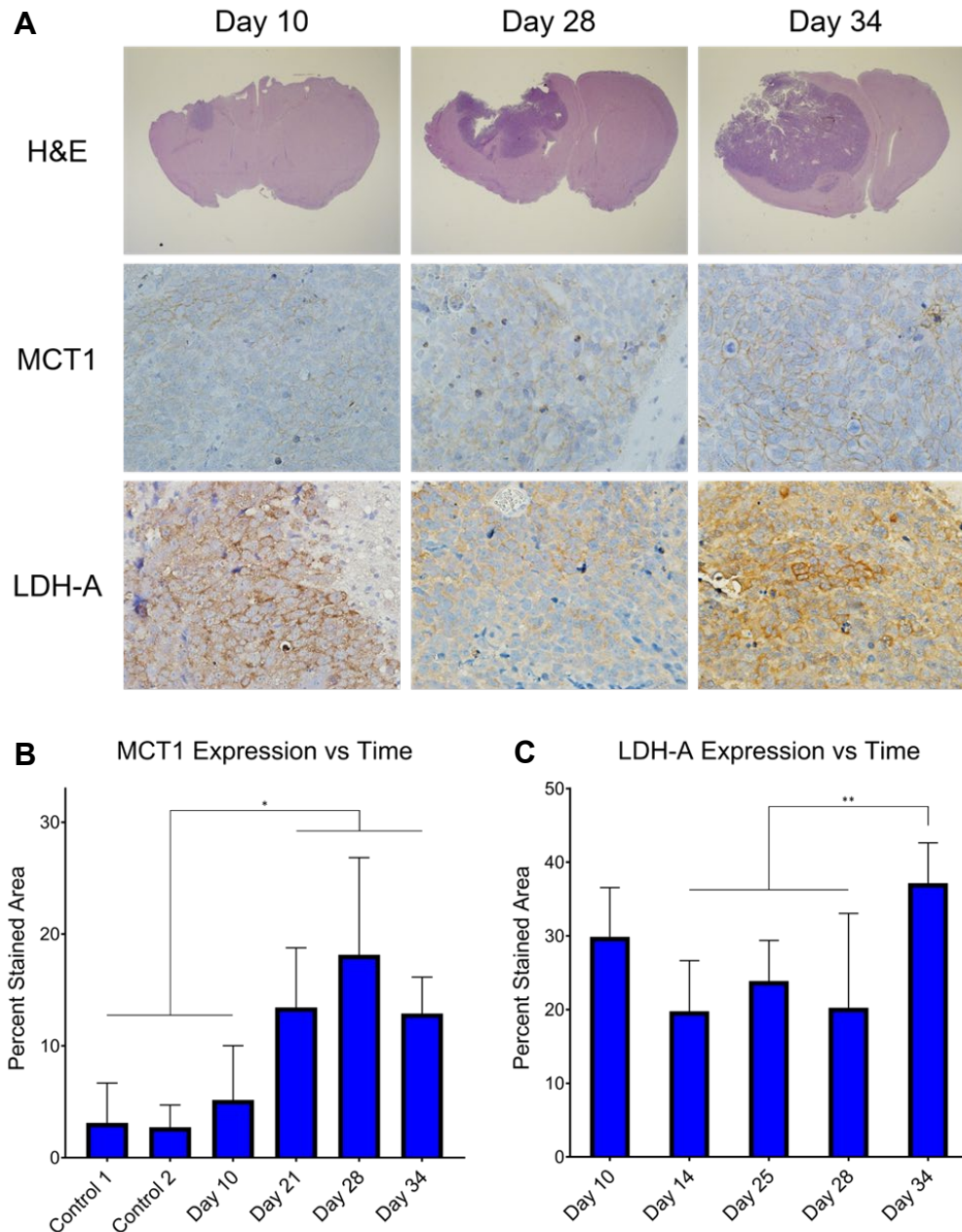


Figure 4.6: *Ex vivo* MCT1 expression significantly increases throughout tumor development. Histology stains of H&E, MCT1, and LDH-A were measured in *ex vivo* untreated tumor samples at several time-points throughout tumor development (**A**). It can be clearly seen that MCT1 is confined to the cell membrane and LDH-A to the cytoplasm. Percent stained area was calculated from the MCT1 (**B**) and LDH-A (**C**) IHC images at these time-points. Average percent stained area between time-points was assessed for significance using ordinary one-way ANOVA and follow-up Fisher's Least Significant Difference tests with significance attributed to comparisons that produced $p < 0.05$. * $p < 0.05$, ** $p < 0.01$.

Discussion

Because average tumor volume values and their variances were low on Day 5, significant increases in untreated tumor volume were detected as soon as Day 10. However, it was not until Day 21 that average tumor volume began to rapidly increase, tripling in value compared with Day 18. Meanwhile, nLac was significantly increased compared with controls beginning on Day 14. Thus, hyperpolarized MRS predicted aggressive growth while the tumor was still in the slow-growing phase. One potential clinical application of this is the ability to distinguish aggressive tumors from their slower-growing counterparts early in tumor development and predict malignant transformation. This would allow physicians to begin administering therapy before the tumor aggressively invades neighboring tissue and is still treatable, which may lead to improvements in patient survival.

An analysis of the REMBRANDT and TCGA databases of patient brain tumors revealed that *SLC16A1* expression- the gene which encodes MCT1- was elevated in GBM compared with lower-grade astrocytoma, oligodendroma, and non-tumor brain samples ¹²⁸. When grouping these glioma subtypes together, those with high expression of *SLC16A1* led to significantly reduced survival compared to those with low expression of *SLC16A1* ¹²⁹. Further analysis of the TCGA database revealed that MCT1 expression was significantly reduced in IDH1-mutant glioma samples compared to those with wild-type IDH1 ¹³⁰. IDH1 mutations are predominately found in WHO grade II and III gliomas (70% of cases) compared to grade IV GBM (12% of cases), and GBM which harbor the IDH1 mutation lead to significantly longer survival times of greater than two-fold ^{32,131}. In individual studies, MCT1 immunoreactivity

scores were significantly increased in 24 high-grade patient samples of GBM and anaplastic astrocytoma compared with 24 low-grade patient samples of oligodendrogliomas and low-grade astrocytomas ¹³², and it was significantly increased in 78 GBM patient samples compared with 24 non-tumor brain samples ¹³³. Furthermore, the MCT inhibitor α -cyano-4-hydroxycinnamate (CHC) induced cytotoxic effects and inhibited proliferation, invasion, and migration capacity in high-grade glioma cell lines which possessed high expression of MCT1 ^{133,134}. Because MCT1 has differential expression between malignant and healthy brain cells, and even between low- and high-grade disease, it is an attractive prognostic biomarker. In this study, we have shown that increasing MCT1 expression correlates with hyperpolarized pyruvate-to-lactate conversion throughout GBM tumor development. In patients with prostate ¹³⁵ and breast cancers ¹³⁶, similar correlations of MCT1 expression and hyperpolarized pyruvate-to-lactate conversion were observed which also correlated with tumor grade. Thus, hyperpolarized MRS has a promising clinical application in the early detection of high-grade brain cancer through MCT1 interrogation.

Specific Aim 2: Administer Radiation Therapy to GBM And Measure the Anatomic and Metabolic Response During Tumor Regression

Results

Tumor Volume (*in vivo*): Following radiotherapy, tumor volume was measured on Days 26, 30, 34, and every 7 days thereafter (Fig. 4.7). On Day 34, average treated tumor volume was significantly increased compared with its initial value on Day 26 (82.9 ± 66.6 vs. 26.0 ± 14.9 mm³, $p = 0.0090$). Average treated tumor volume then began to decrease to a minimum of 57.3 ± 51.2 mm³ on Day 48 although no significant differences were observed compared with initial treated tumor volume on Day 26 or maximum treated tumor volume on Day 34.

Hyperpolarized pyruvate-to-lactate conversion (*in vivo*): Following radiotherapy, hyperpolarized MRS experiments were conducted in treated mice starting on Day 28 and every 7 days thereafter (Fig. 4.8). Average nLac decreased following radiotherapy and was significantly decreased in treated tumor-bearing mice on Day 48 compared with treated tumor-bearing mice on Days 28 (0.31 ± 0.05 vs. 0.44 ± 0.09 , $p = 0.0080$), 34 (0.31 ± 0.05 vs. 0.49 ± 0.08 , $p = 0.0004$), and 41 (0.31 ± 0.05 vs. 0.43 ± 0.07 , $p = 0.0186$). Additionally, average nLac was significantly decreased in treated tumor-bearing mice on Day 48 compared with untreated tumor-bearing mice on Days 28 (0.31 ± 0.05 vs. 0.48 ± 0.06 , $p = 0.0008$) and 34 (0.31 ± 0.05 vs. 0.45 ± 0.09 , $p = 0.0063$). Lastly, of the tumor-bearing mice which had initial values of nLac < 0.4 immediately following treatment (on Day 28 or 34), 0/3 died from tumor burden by the Day 94 endpoint of the study. In contrast, 5/7 treated tumor-bearing mice with initial values of nLac > 0.4 died from tumor burden before reaching the Day 94 endpoint.

Metabolite pool size (*ex vivo*): Following radiotherapy, samples were excised from treated mice at the same time-points as the hyperpolarized MRS experiments for NMR spectroscopy (Fig. 4.9, 4.10). On Day 34, average pool size of the following metabolites were significantly decreased in treated tumors compared with untreated tumors: alanine (2.20 ± 1.42 vs. 4.80 ± 1.98 $\mu\text{M}/\text{mg}$, $q = 0.0072$), glycine (5.21 ± 4.23 vs. 10.56 ± 6.53 $\mu\text{M}/\text{mg}$, $q = 0.0457$), and valine (0.34 ± 0.18 vs. 0.81 ± 0.43 $\mu\text{M}/\text{mg}$, $q = 0.0061$). By Day 48, average pool size of these metabolites were still significantly decreased in treated tumors compared with untreated tumors on Day 34 along with the metabolites, NAD⁺ (0.36 ± 0.05 vs. 0.69 ± 0.21 $\mu\text{M}/\text{mg}$, $q = 0.0496$) and phosphocholine (1.80 ± 0.79 vs. 3.40 ± 1.23 $\mu\text{M}/\text{mg}$, $q = 0.0457$). Another result of note is that on Day 28, average glutathione pool size was significantly increased in treated tumors compared with treated tumors on Days 41 (5.32 ± 1.79 vs. 1.50 ± 0.58 $\mu\text{M}/\text{mg}$, $q = 0.0328$) and 48 (5.32 ± 1.79 vs. 1.81 ± 0.70 $\mu\text{M}/\text{mg}$, $q = 0.0491$).

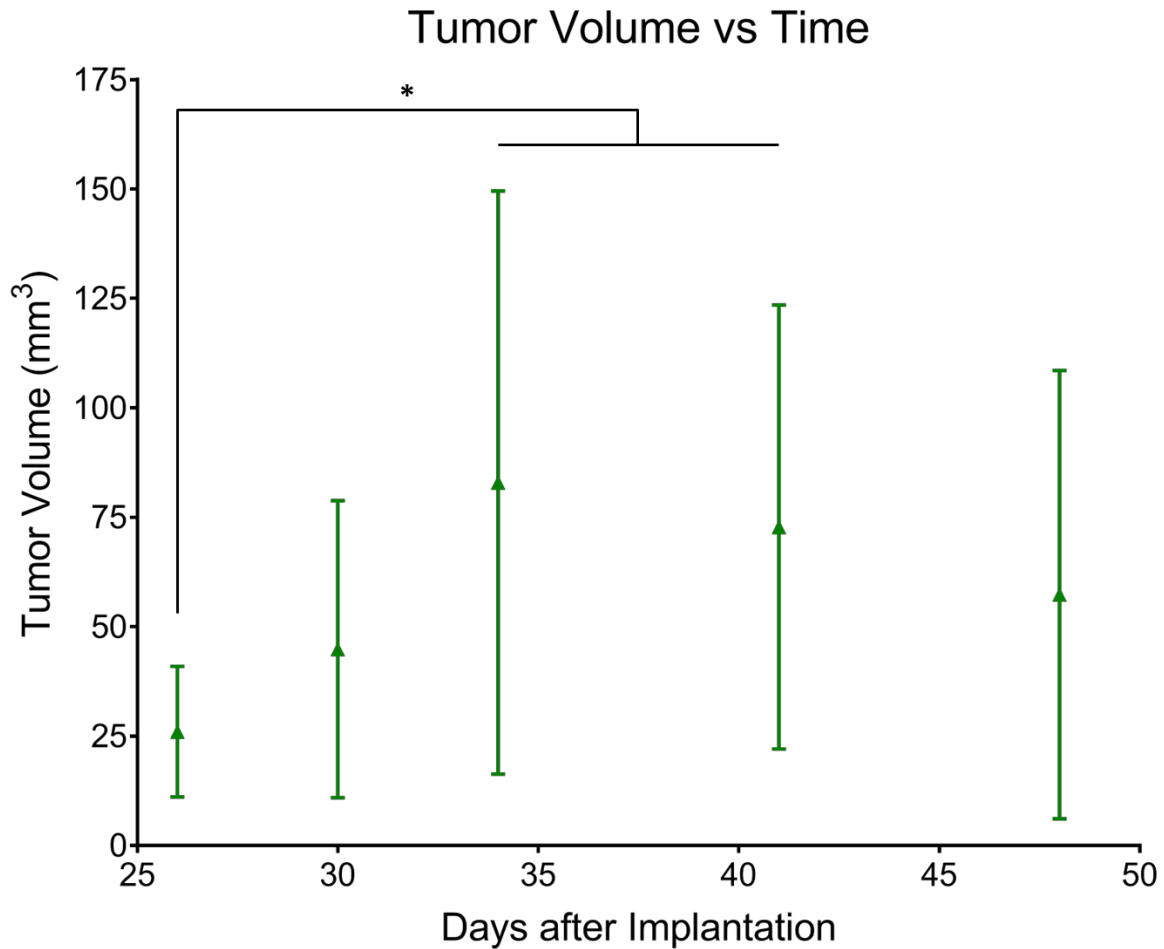


Figure 4.7: *In vivo* tumor volume does not significantly decrease throughout regression. Average tumor volume, measured from anatomic MRI, is plotted as a function of time in treated mice. Apparent pseudoprogression was observed immediately following radiotherapy before tumor volume began to decrease. Error bars represent standard deviation. These values were log-transformed to correct for heteroscedasticity and tested for significant differences using ordinary one-way ANOVA and follow-up Fisher's Least Significant Differences tests. Comparisons that produced $p < 0.05$ were deemed significant. * $p < 0.05$.

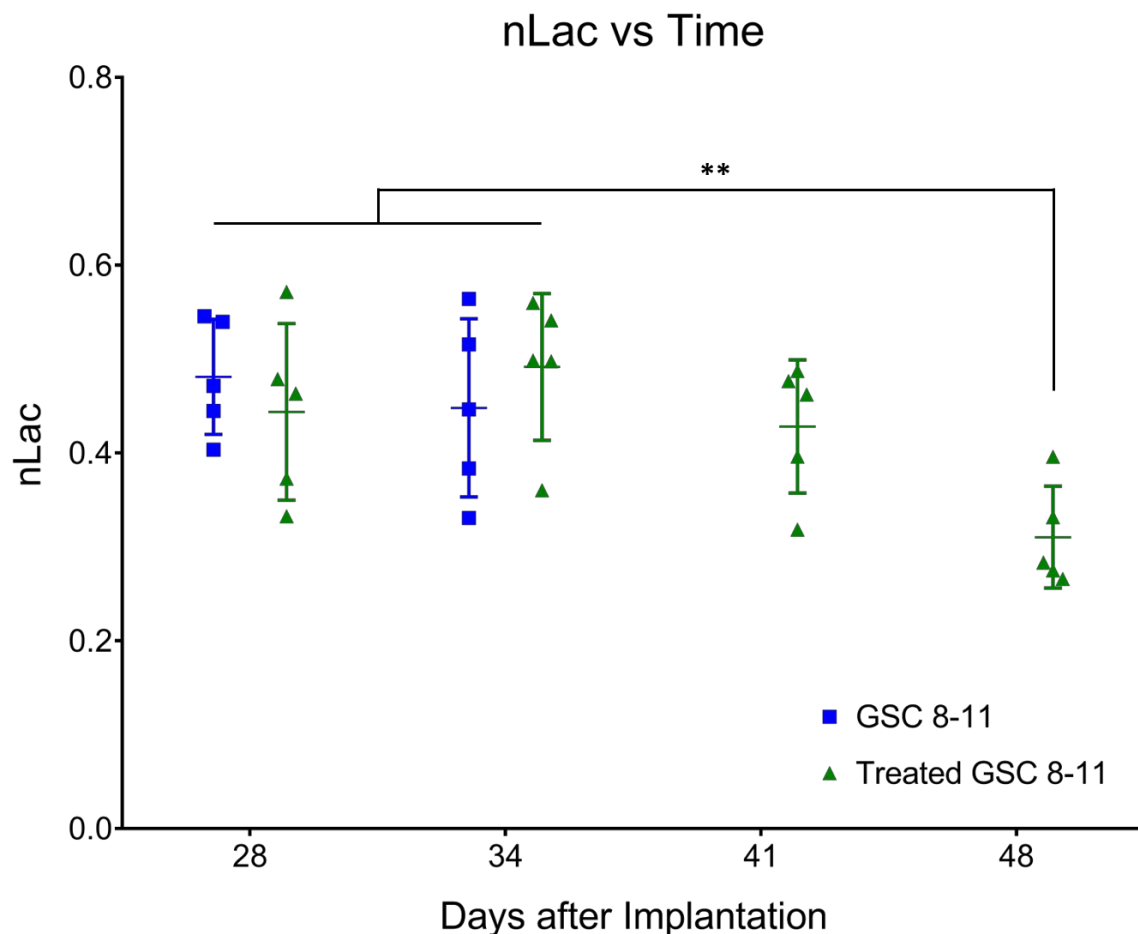


Figure 4.8: *In vivo* pyruvate-to-lactate conversion significantly decreases throughout tumor regression. Individual nLac values, measured with hyperpolarized ^{13}C MRS, are plotted as a function of time for untreated (blue squares) and treated (green triangles) tumor-bearing mice during tumor regression following radiotherapy. Average nLac values between groups and time-points were assessed for significance using ordinary one-way ANOVA and follow-up Fisher's Least Significant Difference tests. Error bars represent standard deviation. Significance attributed to comparisons that produced $p < 0.05$. ** $p < 0.01$.

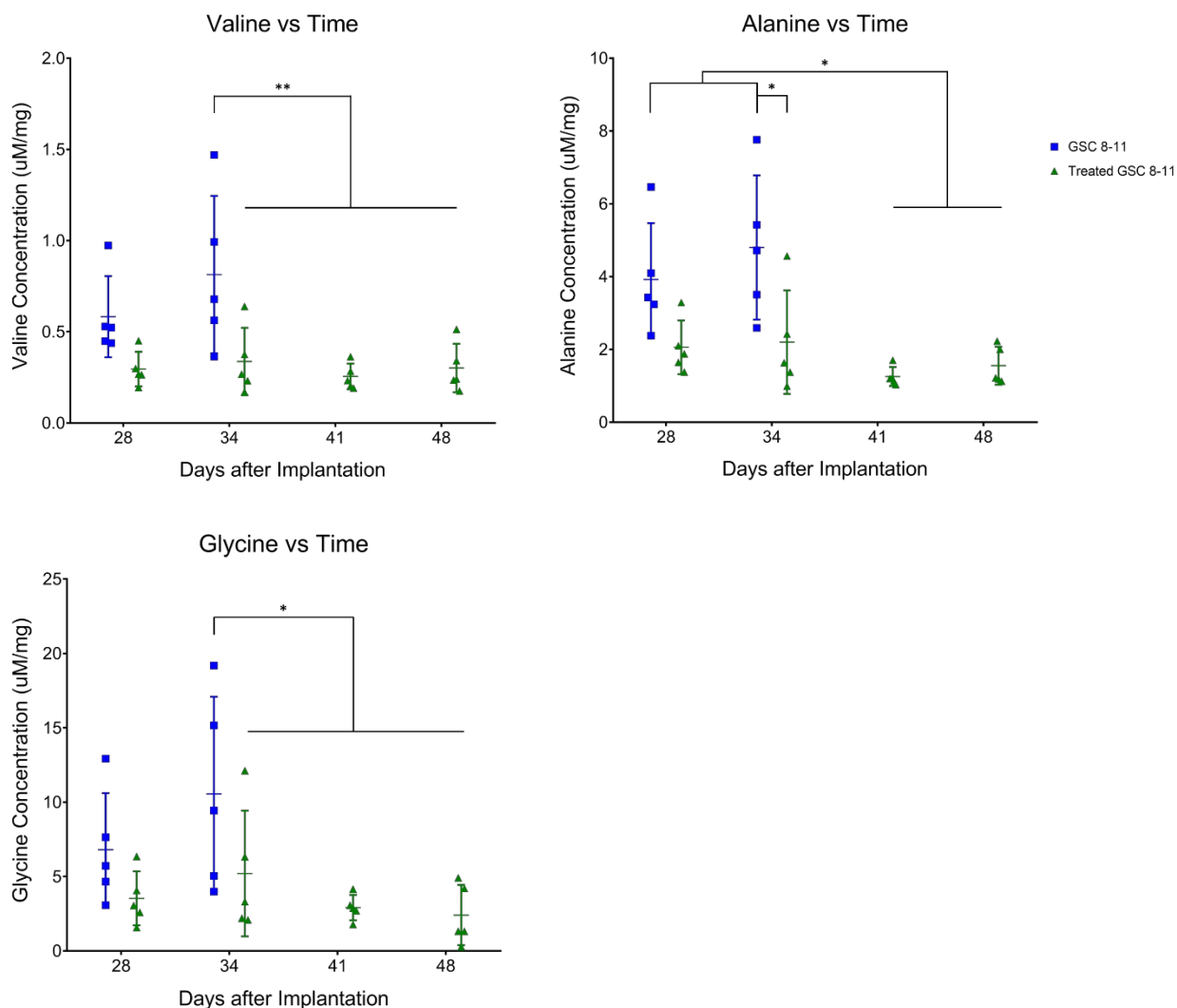


Figure 4.9: *Ex vivo* metabolite pool sizes significantly decrease throughout tumor regression (Part 1). Individual metabolite pool sizes, measured with NMR spectroscopy, are plotted as a function of time for untreated (blue squares) and treated (green triangles) tumor-bearing mice. Error bars represent standard deviation. The Y-axis is reported as concentration of metabolite pool per mg of tissue. Statistical significance was determined using ordinary one-way ANOVA and follow-up Fisher's Least Significant Difference tests. The false discovery rate was controlled using the two-stage step-up method of Benjamini, Krieger and Yekutieli, and significance was attributed to comparisons that produced $q < 0.05$. * $q < 0.05$, ** $q < 0.01$.

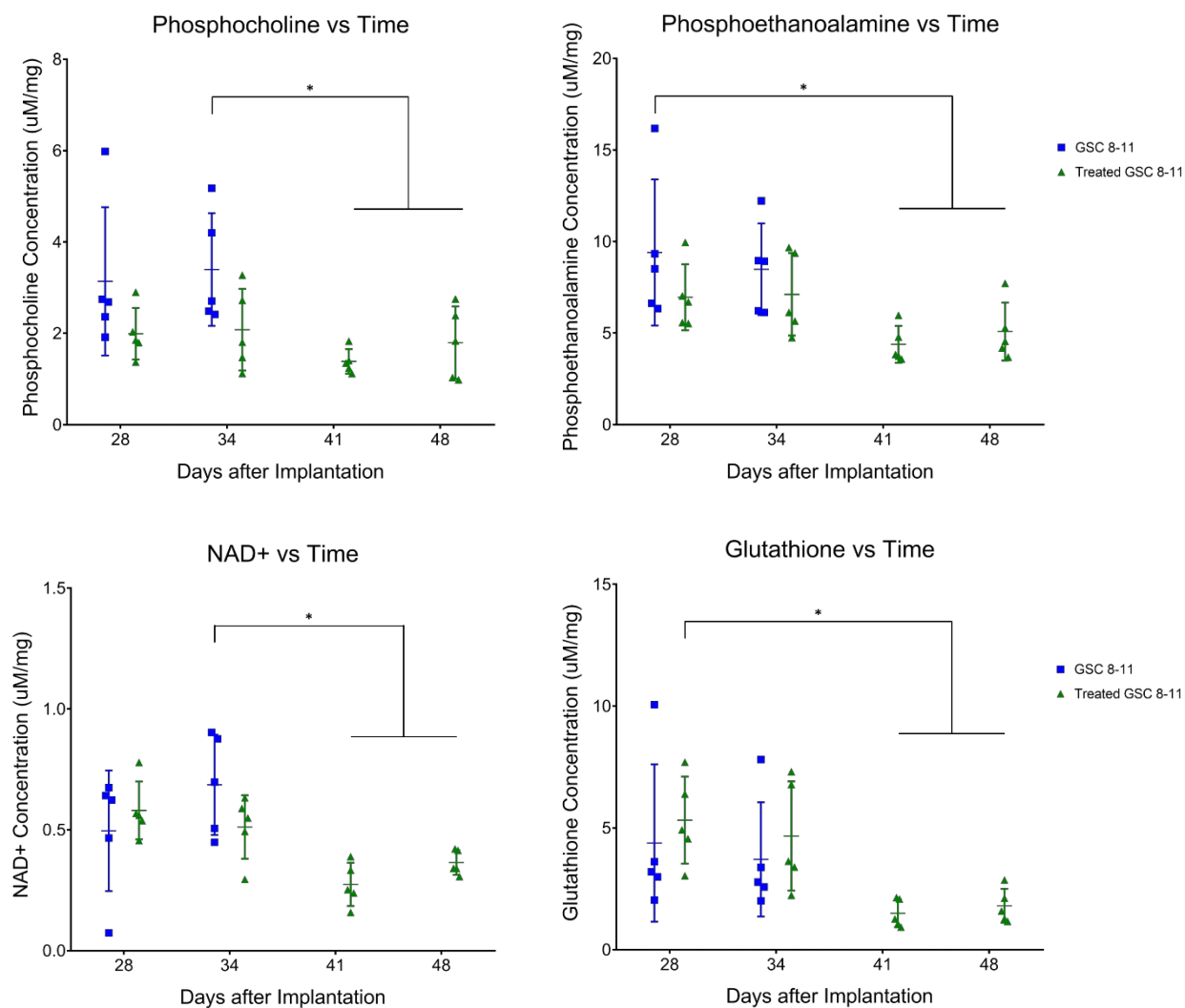


Figure 4.10: *Ex vivo* metabolite pool sizes significantly decrease throughout tumor regression (Part 2). Individual metabolite pool sizes, measured with NMR spectroscopy, are plotted as a function of time for untreated (blue squares) and treated (green triangles) tumor-bearing mice. Error bars represent standard deviation. The Y-axis is reported as concentration of metabolite pool per mg of tissue. Statistical significance was determined using ordinary one-way ANOVA and follow-up Fisher's Least Significant Difference tests. The false discovery rate was controlled using the two-stage step-up method of Benjamini, Krieger and Yekutieli, and significance was attributed to comparisons that produced $q < 0.05$. * $q < 0.05$.

Discussion

One current clinical challenge facing neuro-oncologists is distinguishing pseudoprogression from true progression following radiotherapy. Pseudoprogression is an anatomic MRI pattern that mimics tumor progression and can confound treatment monitoring with direct consequences in clinical practice. It can lead to prematurely withholding adjuvant temozolomide or continuing with potentially ineffective treatment in patients in which cases of tumor progression are not clear¹³⁷. Apparent pseudoprogression was observed in this study with anatomic MRI as tumor volumes in treated mice significantly increased on Days 34 and 41 before eventually decreasing throughout regression. Conversely, there were no significant increases in nLac during this time-course, which suggests hyperpolarized MR could help mitigate this problem in the clinic.

When comparing the quality of the data, there were larger magnitudes of change and lower variance in the hyperpolarized MRS data compared with the anatomic MRI data throughout tumor regression. This allowed us to observe significant changes in hyperpolarized pyruvate-to-lactate conversion following radiotherapy, rendering it a more sensitive measure of tumor response. After radiotherapy, nLac decreased significantly in treated tumor-bearing mice on Day 48 compared with Days 28 and 34 whereas tumor volume did not significantly decrease in this time period. This suggests that hyperpolarized MRS has the potential to effectively detect treatment response of GBM to radiotherapy and do so more reliably than measuring changes in tumor volume with anatomic MRI. Furthermore, the predictive value of hyperpolarized MRS to stratify subjects into likely and unlikely

responders was alluded to when looking at the initial nLac values following treatment. Of the 10 mice who underwent hyperpolarized MRS immediately following treatment, a cutoff value of nLac > 0.4 was able to predict if a mouse would succumb to tumor burden before the Day 94 endpoint with a sensitivity of 100% and specificity of 60%. These sample sizes are too small to draw definite conclusions, but it serves as motivation for a larger study.

Specific Aim 3: Monitor the Anatomic and Metabolic States of Regressed GBM Tumors to the Point of Relapse

Results

Tumor Volume (*in vivo*): The same group of mice were imaged every 7 days throughout tumor recurrence (Fig. 4.11). After reaching a minimum of $57.3 \pm 51.2 \text{ mm}^3$ on Day 48, average treated tumor volume monotonically increased to a final volume of $72.3 \pm 57.0 \text{ mm}^3$ on Day 72. While this value was significantly higher than initial treated tumor volume on Day 26 ($p = 0.0396$), neither grouped ANOVA analysis nor mixed-effects analysis of individual repeated measures revealed any significant increases in treated tumor volume throughout the stage of tumor recurrence.

Hyperpolarized pyruvate-to-lactate conversion (*in vivo*): Hyperpolarized MRS experiments were performed on the same group of mice every 7 days throughout tumor recurrence (Fig. 4.12). Average nLac linearly increased with a significantly nonzero slope (0.0067 days^{-1} , $p < 0.0001$) in treated tumor-bearing mice from Day 48 to Day 68. When compared with the trend of average nLac in untreated tumor-bearing mice during tumor development, average nLac in treated tumor-bearing mice during tumor recurrence had a nearly identical slope (0.0067 vs. 0.0069 days^{-1} , $p = 0.9415$). When analyzed with grouped ANOVA analysis, average nLac in treated tumor-bearing mice was significantly increased by Day 68 compared with treated tumor-bearing mice on Days 48 (0.44 ± 0.04 vs. 0.31 ± 0.05 , $p = 0.0085$) and 55 (0.44 ± 0.04 vs. 0.35 ± 0.05 , $p = 0.0452$) as well as when compared with control mice on Days 28 (0.44 ± 0.04 vs. 0.32 ± 0.10 , $p = 0.0341$) and 34 (0.44 ± 0.04 vs. 0.22 ± 0.01 , $p = 0.0002$). Furthermore, when analyzing comparisons of individual repeated measurements with

mixed-effects analysis, nLac was still significantly increased on Day 68 compared with Day 55 (0.44 ± 0.04 vs. 0.35 ± 0.05 , $p = 0.0214$).

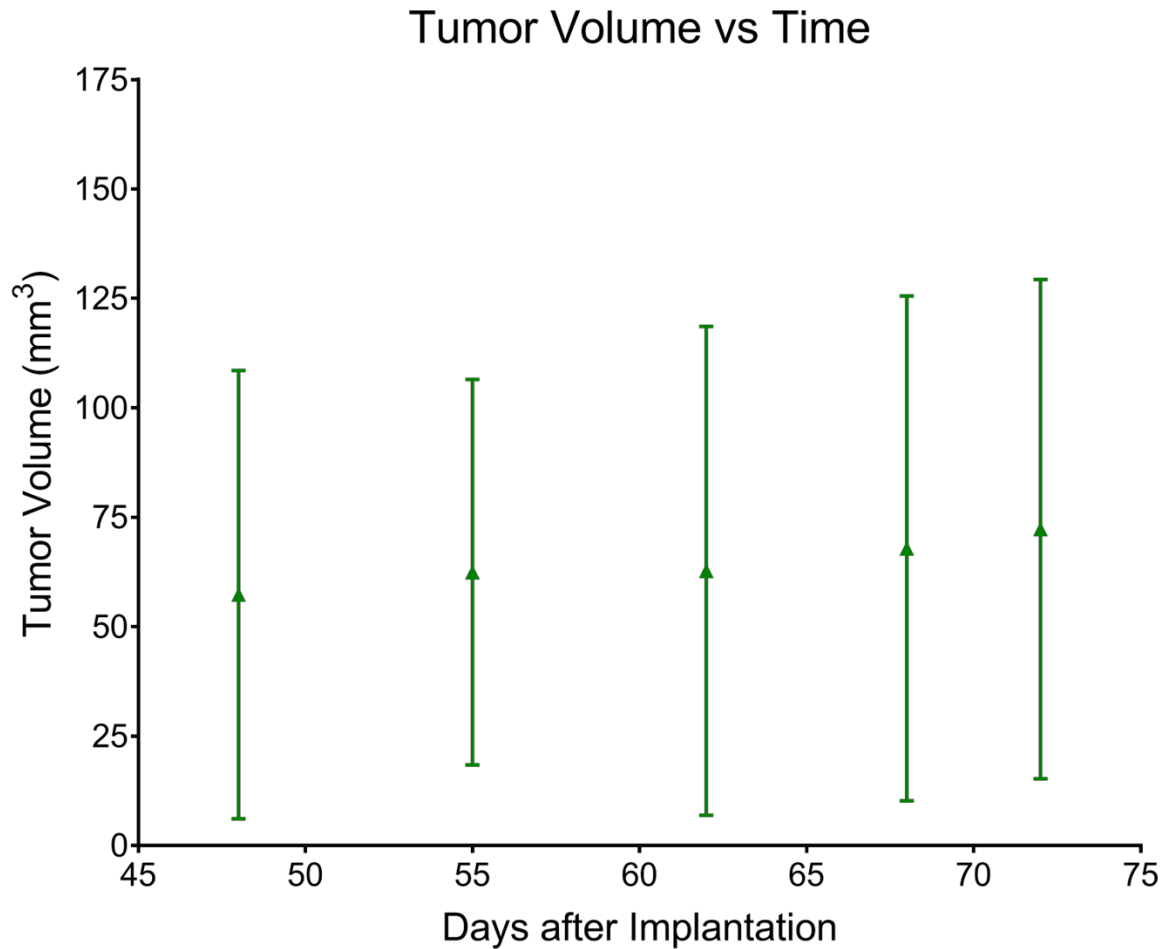


Figure 4.11: *In vivo* tumor volume does not significantly increase throughout recurrence. Average tumor volume, measured from anatomic MRI, is plotted as a function of time in treated mice. Error bars represent standard deviation. These values were log-transformed to correct for heteroscedasticity and tested for significant differences using ordinary one-way ANOVA and follow-up Fisher's Least Significant Differences tests. Comparisons that produced $p < 0.05$ were deemed significant.

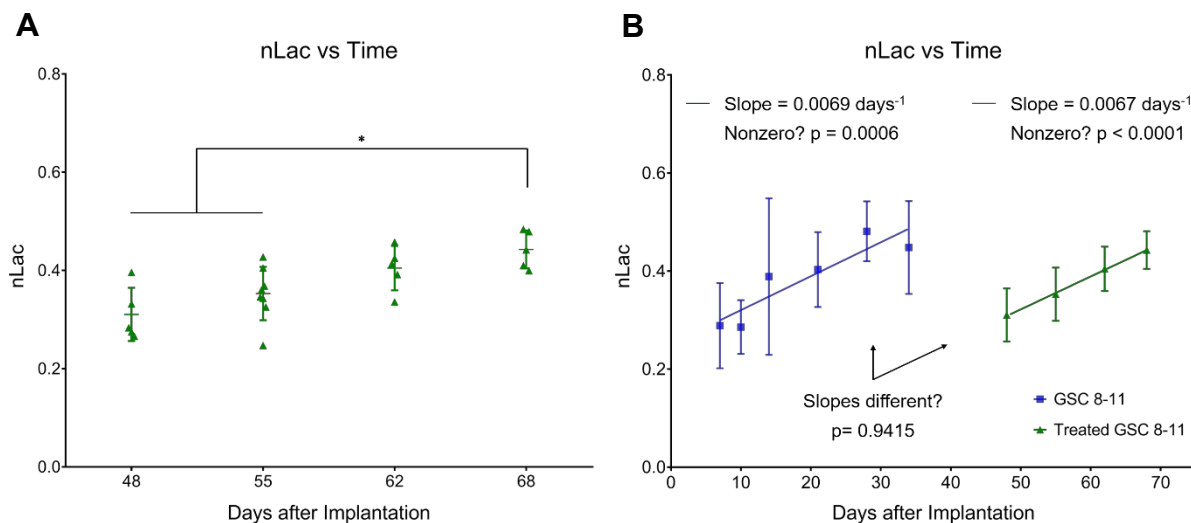


Figure 4.12: *In vivo* pyruvate-to-lactate conversion significantly increases throughout tumor recurrence. nLac values, measured with hyperpolarized ^{13}C MRS, are plotted as a function of time for untreated (blue squares) and recurring treated (green triangles) tumor-bearing mice during tumor recurrence. Individual nLac values for each time-point are plotted in **(A)**. Statistically significant changes of nLac between treated tumor-bearing mice at different time-points are illustrated. Average nLac values between time-points were assessed for significance using ordinary one-way ANOVA and follow-up Fisher's Least Significant Difference tests. Average nLac values for each time-point are plotted in **(B)** along with a linear fit of the data for untreated and recurring treated tumor-bearing mice, which demonstrates the similarity of nLac evolution over time. The slopes of the linear fits are depicted in addition to the p-values from the comparisons of whether the slopes were significantly greater than zero as well as whether they were significantly different from each other. Linear regression was performed to calculate linear fits with each replicate considered, and slope values were tested for significance with the F-test (to test against a slope value of 0) or two-tailed T-test (to test the slope values against each other). Error bars represent standard deviation. Significance attributed to comparisons that produced $p < 0.05$. * $p < 0.05$.

Discussion

To our knowledge, this is the first study to investigate all three stages of brain tumor progression, including tumor recurrence, with hyperpolarized MRS. There is one prior study that used hyperpolarized MRSI to measure the glycolytic effects of switching off MYC expression in transgenic mouse models of breast cancer which resulted in tumor regression followed by recurrence¹³⁸. Shin, et al. observed that the hyperpolarized lactate/pyruvate ratio significantly decreased as the tumors regressed from MYC withdrawal, and after a latency period, the tumors recurred, which was accompanied by a significant increase of hyperpolarized lactate/pyruvate ratio. In one of the mice, this increase of lactate production was observed prior to increases in tumor volume, which supports the results we observed across multiple treated GBM tumor-bearing mice.

Analogous with the tumor regression stage, no significant changes in volume were observed during tumor recurrence. The only significant change in volume that was observed following radiotherapy was that average treated tumor volume on Day 72 was significantly increased compared with initial treatment volume on Day 26, which does suggest that the mice were beginning to relapse. Even when treated tumor volumes were normalized to their individual initial values to measure percent change (for those mice that were measured several times throughout regression and recurrence), no significant changes were observed throughout regression or recurrence (Fig. 4.13). Within this set of repeated tumor volume measurements, average tumor volume reached a minimum of 81% of its initial treated volume on Day

62 before increasing back to 96% of its initial treated volume on Day 72, which further suggests that relapse was beginning to occur.

Hyperpolarized MRS was effective at predicting relapse as nLac was significantly increased in treated mice by Day 68 compared with Days 48 and 55 whereas tumor volume did not significantly increase in this time period. Furthermore, nLac values in treated mice on Day 68 were equivalent to initial values following treatment on Days 28 and 34. Thus, there was a complete reprise in hyperpolarized pyruvate-to-lactate conversion by Day 68, further supporting that relapse was occurring. When looking at percent change of nLac in the mice that were measured at multiple time-points throughout regression and recurrence, average nLac fell to a minimum of 71% of its initial value after treatment on Day 55. This value was significantly decreased ($p = 0.0258$) compared with Day 68 when average nLac was back to 88% of the initial treated value (Fig. 4.13). Based on these data, we suspect that pyruvate-to-lactate conversion measured with hyperpolarized MRS in this animal model is a direct metabolic readout of tumor response during regression (Day 55) and relapse (Day 68) which is occurring prior to radiological tumor volume changes.

Another interesting result is that the slope of nLac in treated tumor-bearing mice in the tumor recurrence stage was nearly identical to that of the untreated tumor-bearing mice in the development stage. This suggests that the metabolic programming of recurring tumors was not altered, and the mechanism of recurrence was similar to that of initial growth. This is expected since tumors were only treated with radiotherapy. Had adjuvant chemotherapy or targeted therapy been implemented, cancer cells could have potentially been pressured to escape therapy through the

development of resistance by adapting and reprogramming a new mechanism of survival and proliferation, which may have been reflected in the metabolic assays. This idea is currently of immense interest as metabolic changes that reflect resistance to therapy could be exploited with molecular imaging techniques and would be invaluable to physicians looking to optimize therapeutic approaches. This could have a significant benefit for patients with recurrent disease, and future research will investigate this idea further.

Because tumor volume appeared to lag behind hyperpolarized pyruvate-to-lactate conversion, it was postulated that the metabolic events would more accurately align with the rate of change of volume. After all, macroscopic tumor volume is a result of the culmination of all the growth processes occurring in the cell. Increased pyruvate-to-lactate conversion, which is a biomarker of proliferation, should be associated with relative increases in volume rather than the absolute value of the volume. Therefore, the volume curves were linearly interpolated between the data points to form a continuous curve and then numerically differentiated, using the symmetric Newton's quotient method, to calculate the rate of change of the volume ($d\text{Volume}/dt$) over time (Fig. 4.14). The timing of the shift from regression to recurrence appears to be more consistent between nLac and $d\text{Volume}$ compared with nLac and volume, although changes in $d\text{Volume}$ still lag behind changes in nLac.

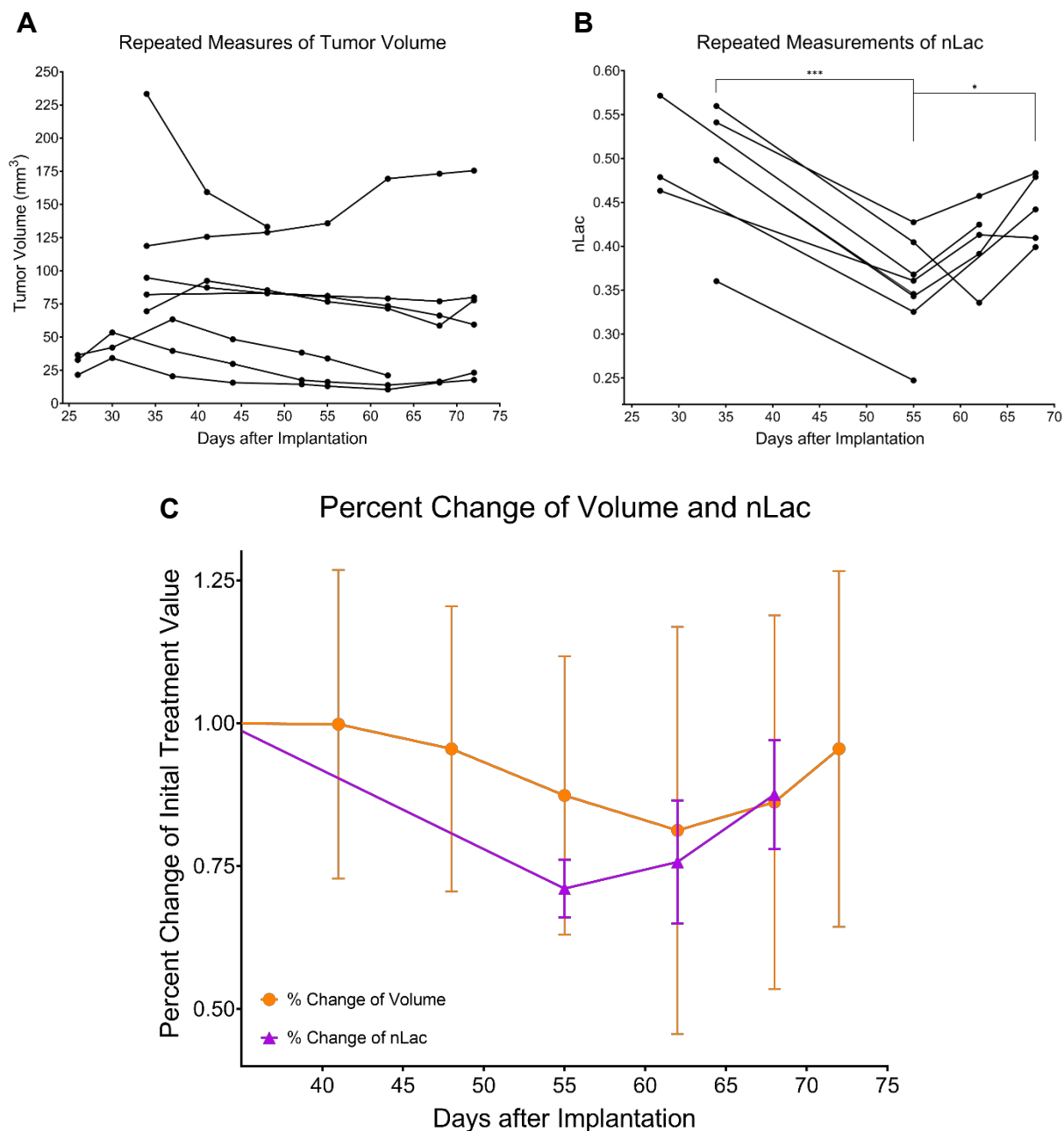


Figure 4.13: Percent change of nLac, but not tumor volume, is significantly altered during tumor regression and recurrence. Repeated measures of tumor volume are acquired over time in treated mice with anatomic MRI **(A)** and hyperpolarized MRS **(B)**. At each time-point, volume and nLac were normalized to their initial value following treatment and plotted as percent change over time **(C)**. The data were tested for significance using mixed-effects analysis with the Geisser-Greenhouse correction, and comparisons that produced $p < 0.05$ were deemed significant. * $p < 0.05$, *** $p < 0.001$.

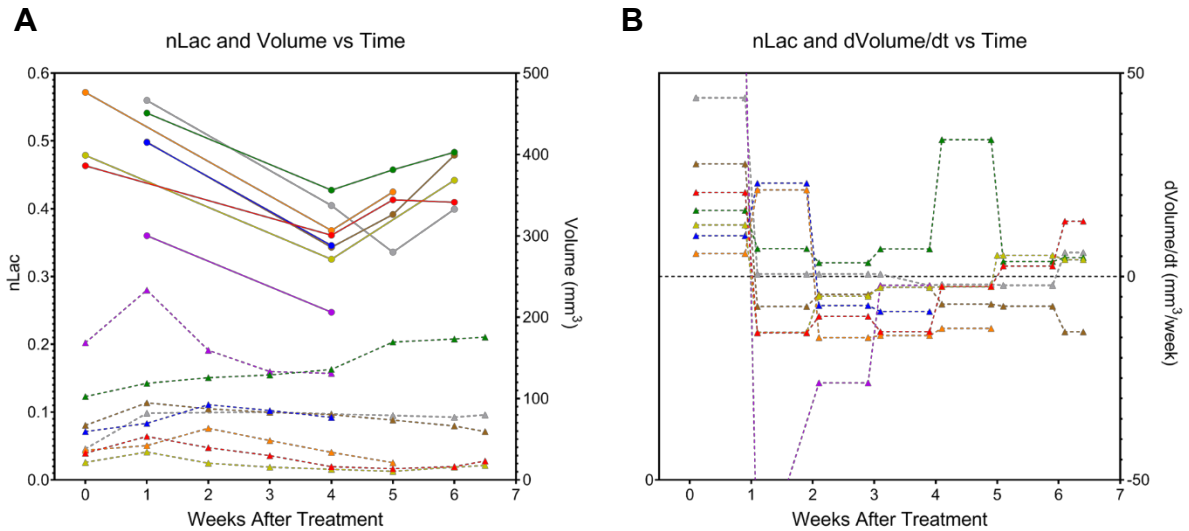


Figure 4.14: Evolution of nLac, volume, and rate of change of volume following radiotherapy. nLac (solid lines) and tumor volume (dashed lines) are plotted on the same time axis (represented as weeks after treatment) to clearly compare the changes in these variables over time **(A)**. Tumor volume was numerically differentiated using the symmetric Newton's quotient method and plotted over time to visualize the rate of change of volume **(B)**. A dashed line is drawn through $d\text{Volume}/dt = 0$ to illustrate at what value tumor volume is not changing. Values below this line indicate tumors are shrinking and values above this line indicate that they are growing. Each colored line represents the same mouse.

Supplemental Data

Results

Radiotherapy Significantly Extends Survival of GSC 8-11 Tumor-Bearing Mice:

In mice implanted with GSC 8-11, survival time was compared between untreated mice and mice treated with 2x5 Gy of whole-brain irradiation on Days 25 and 27 using Kaplan-Meier analysis (Fig. 4.15). Median survival was significantly increased in treated tumor-bearing mice compared with untreated mice (88 vs. 34 days, $p < 0.0001$). There was over a 250% increase in median survival time, which produced a hazard ratio of 4.6. Therefore, the radiotherapy dose of 2x5 Gy was effective at extending the survival of tumor-bearing mice, allowing for tumor regression and recurrence to be assessed in the radiotherapy treated mouse cohort.

Anatomic and Metabolic Changes Throughout All of Tumor Progression (Day 1-

72): Tumor volume (Fig. 4.16), hyperpolarized pyruvate-to-lactate (Fig. 4.17), and metabolite pool size (Fig. 4.18, 4.19) data from each stage of tumor progression (development, regression, and recurrence) are combined and plotted on one graph. The purpose of these figures is to qualitatively visualize the complete evolution of tumor anatomy and metabolism, so statistical analyses are not included (since they were presented in the previous sections). Refer to Table 4.1 for all significant metabolite pool size changes throughout tumor development and regression.

Correlations Between Tumor Volume, In Vivo Pyruvate-To-Lactate Conversion,

And Ex Vivo Metabolite Pool Sizes: Log-transformed tumor volume and nLac values from the same mice at the same time-points were plotted against one another, and

significant positive correlations were observed in untreated ($R^2 = 0.3086$, $p = 0.0021$) and treated ($R^2 = 0.2076$, $p = 0.0100$) tumor-bearing mice (Fig. 4.20A). Of the *ex vivo* metabolite pools that were significantly altered during tumor development or regression, those that were significantly positive-correlated with log-transformed tumor volume in untreated tumors were (Fig. 4.20B, Fig. 4.21): alanine ($R^2 = 0.6821$, $p < 0.0001$), glycerophosphocholine ($R^2 = 0.5001$, $p = 0.0001$), glycine ($R^2 = 0.5626$, $p < 0.0001$), NAD⁺ ($R^2 = 0.3224$, $p = 0.0038$), phosphocholine ($R^2 = 0.5528$, $p < 0.0001$), phosphoethanolamine ($R^2 = 0.5515$, $p < 0.0001$), and valine ($R^2 = 0.4958$, $p = 0.0001$). Significant positive correlations were also observed between nLac and *ex vivo* pool size of glycerophosphocholine ($R^2 = 0.3315$, $p = 0.0032$) and phosphoethanolamine ($R^2 = 0.1802$, $p = 0.0387$) (Fig. 4.20C,D). Other than a negative correlation between NAD⁺ pool size and nLac ($R^2 = 0.40$, $p = 0.0497$), no significant correlations between *ex vivo* metabolite pool sizes and either log-transformed tumor volume or *in vivo* pyruvate-to-lactate conversion were observed in treated tumors. Pearson correlation coefficients were also calculated between each of the *ex vivo* metabolite pool sizes in the untreated and treated tumors, controls, and combination of all groups. Correlation matrices of these values are illustrated for qualitative analysis of potential metabolic pathways that could be up- or down-regulated during tumor development and regression (Fig. 4.22).

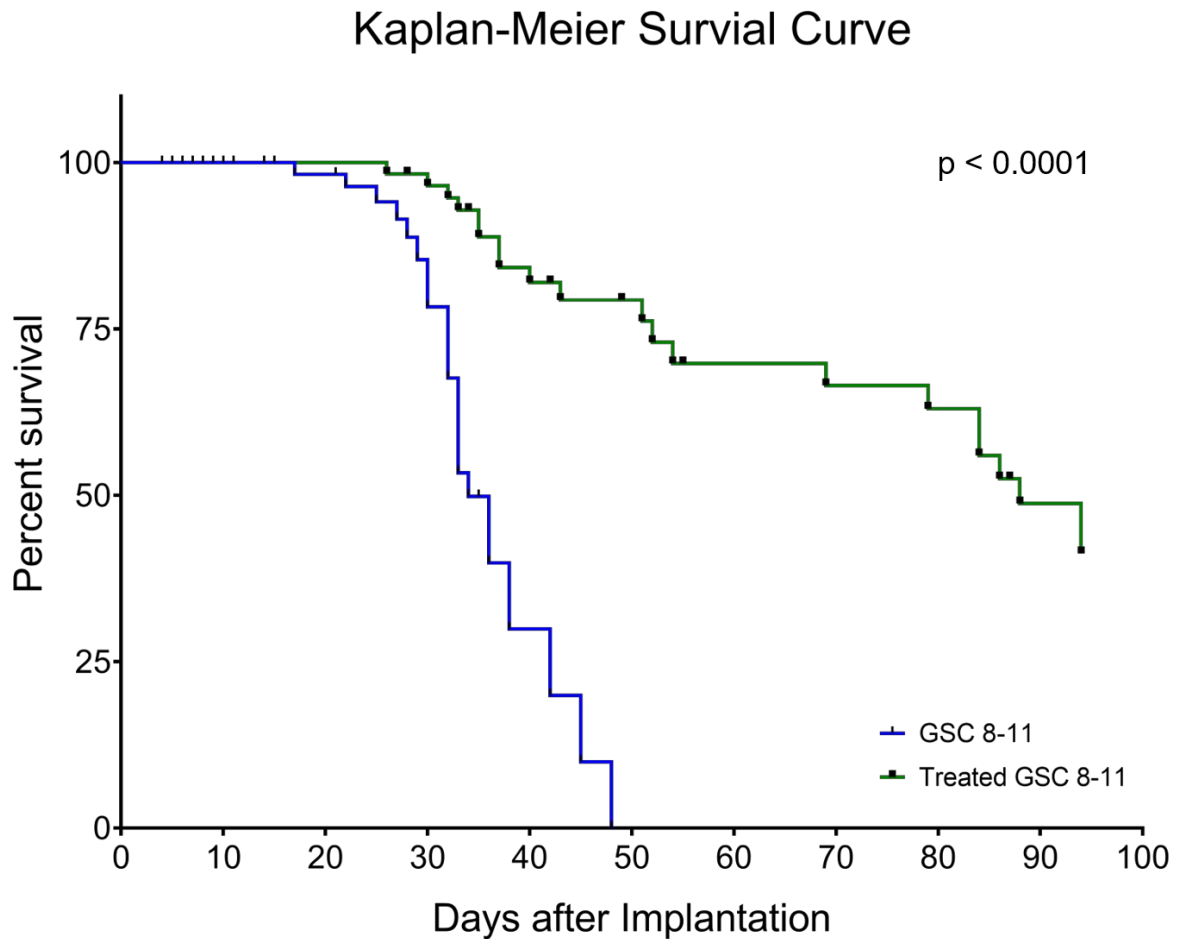


Figure 4.15: Radiotherapy significantly extends survival of GSC 8-11 tumor-bearing mice. Median survival of treated mice (green line) was significantly higher compared with untreated mice (blue line) (88 vs. 34 days, $p < 0.0001$). The hazard ratio of untreated-to-treated mice was 4.6. Mice that were euthanized on specific time-points for *ex vivo* experiments as well as those that died from non-tumor-related causes (such as from infection or from the experiment itself) were censored (black markers). Survival was calculated using Kaplan-Meier analysis. Significant differences between the curves was calculated with the Mantel-Cox logrank test and the hazard ratio using logrank approach.

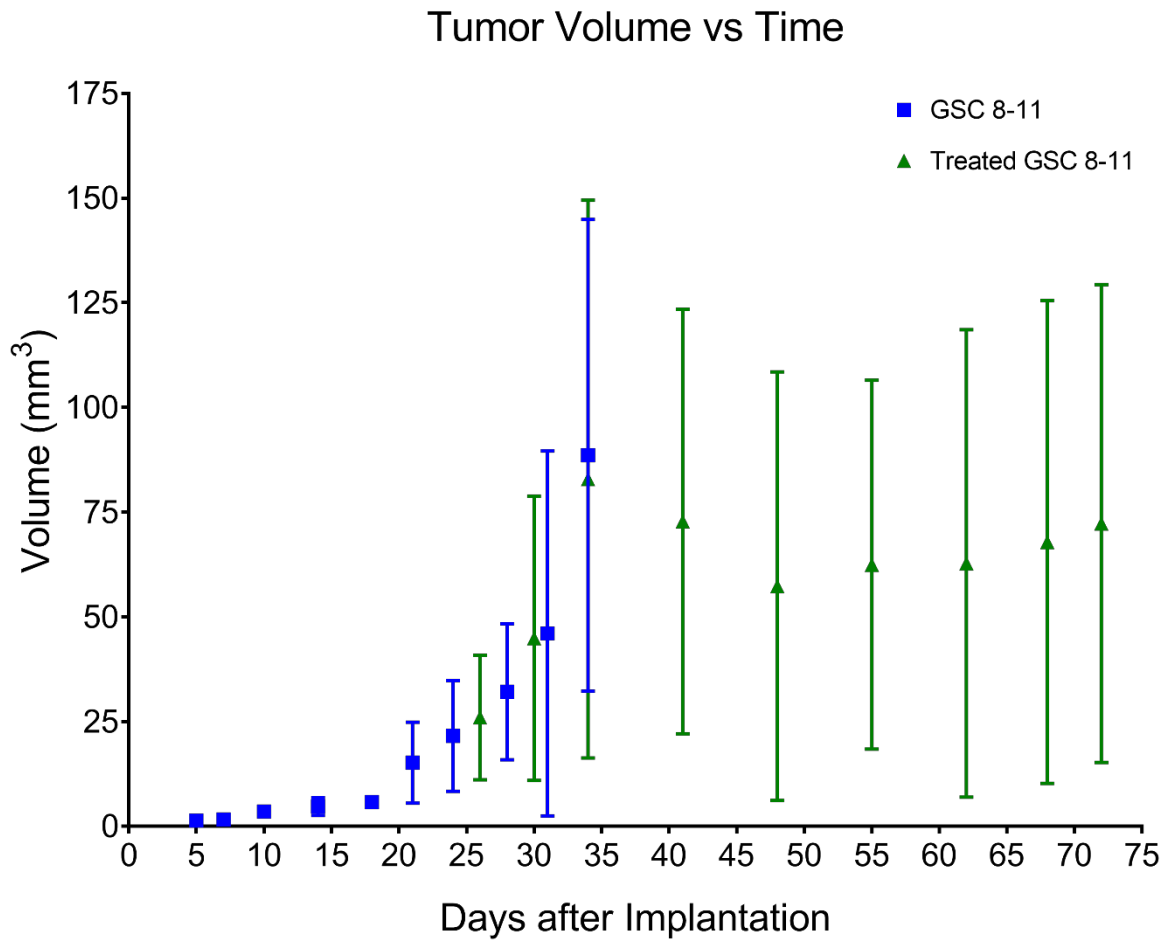


Figure 4.16: Tumor volume increases during development but does not significantly change throughout regression or recurrence. Average tumor volume, measured from anatomic MRI, is plotted as a function of time in untreated (blue squares) and treated (green triangles) mice. Error bars represent standard deviation.

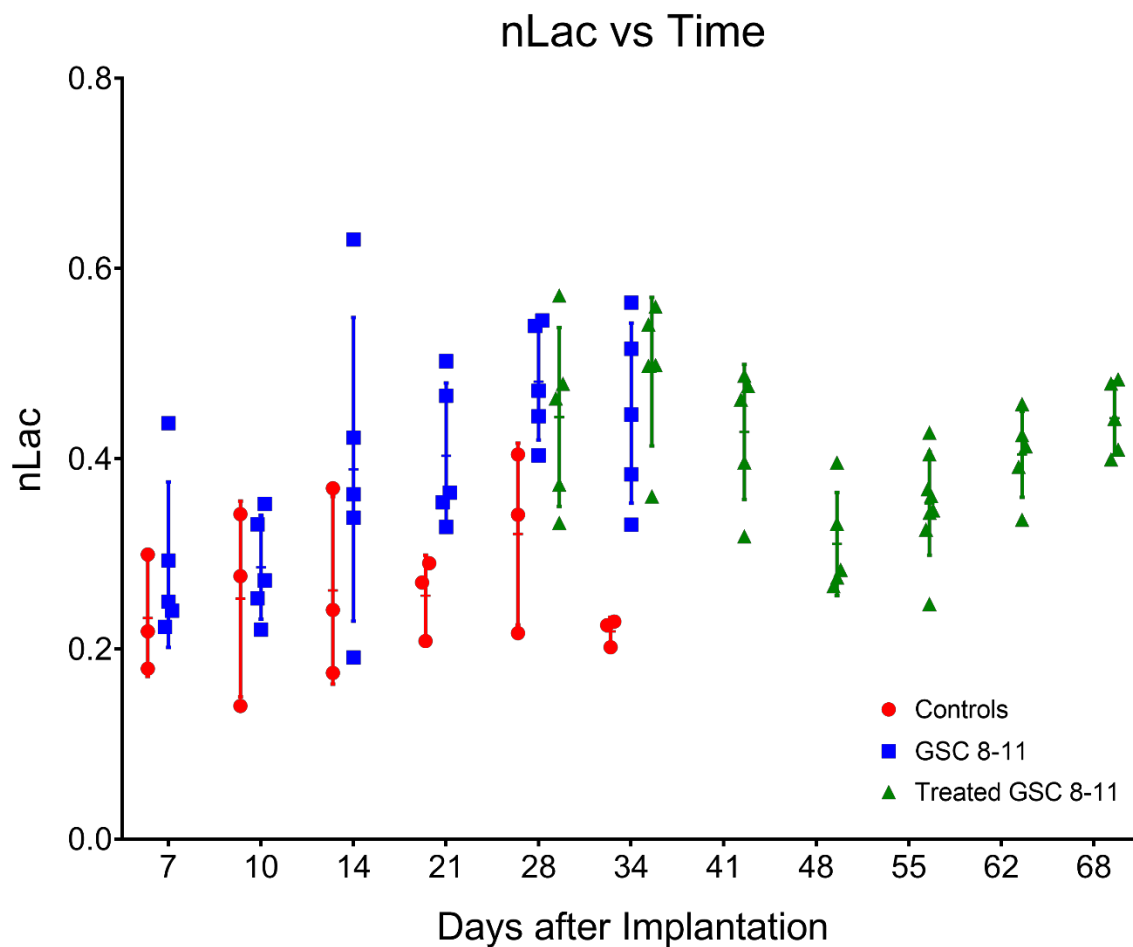


Figure 4.17: *In vivo* pyruvate-to-lactate conversion is significantly altered throughout tumor development, regression, and recurrence. Individual nLac values, measured with hyperpolarized ^{13}C MRS, are plotted as a function of time for control mice (red circles) and untreated (blue squares) and treated (green triangles) tumor-bearing mice at all points of tumor progression. Error bars represent standard deviation.

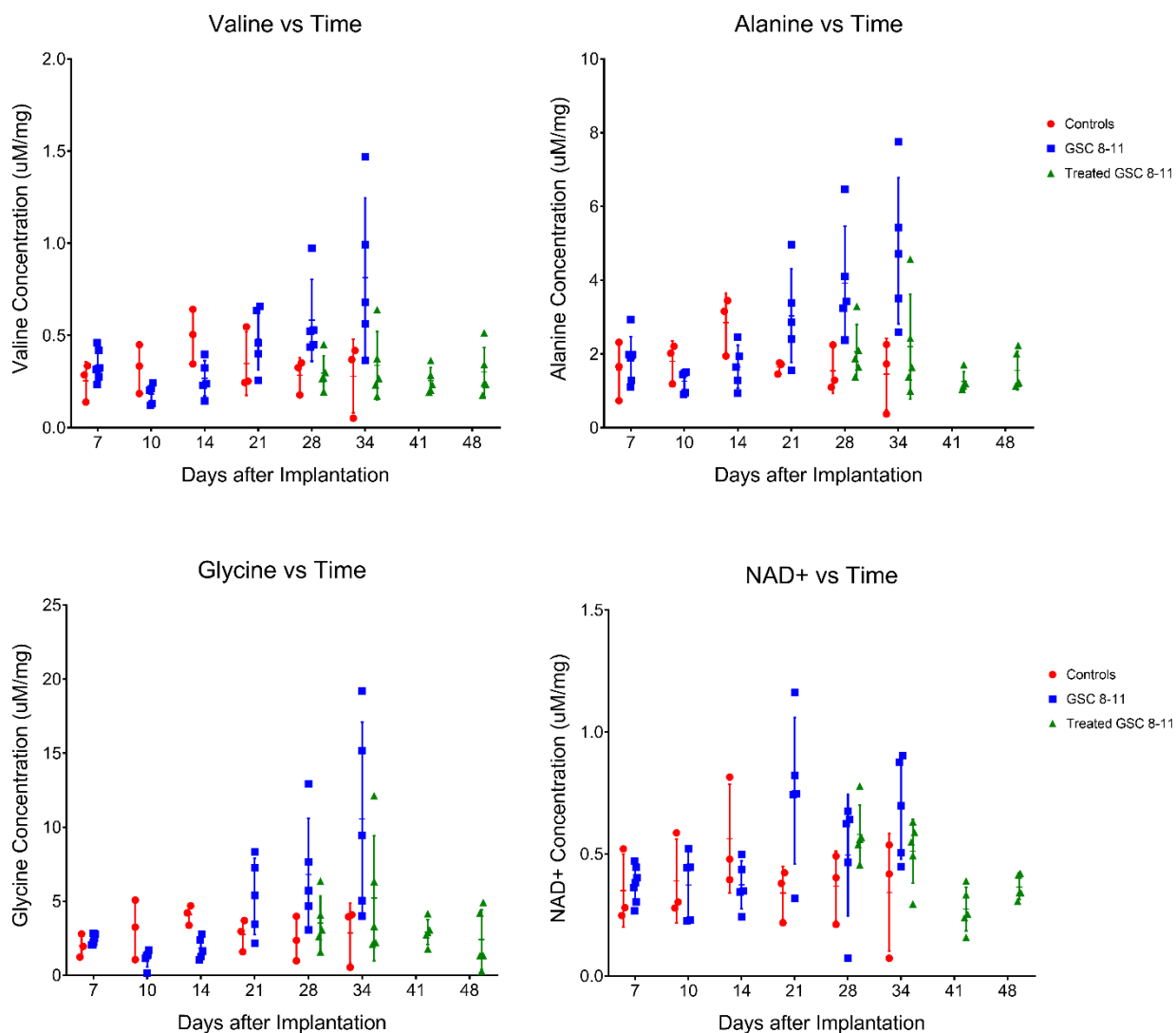


Figure 4.18: *Ex vivo* metabolite pool sizes are significantly altered throughout tumor development and regression (Part 1). Individual metabolite pool sizes, measured with NMR spectroscopy, are plotted as a function of time for control mice (red circles) and untreated (blue squares) and treated (green triangles) tumor-bearing mice. Error bars represent standard deviation.

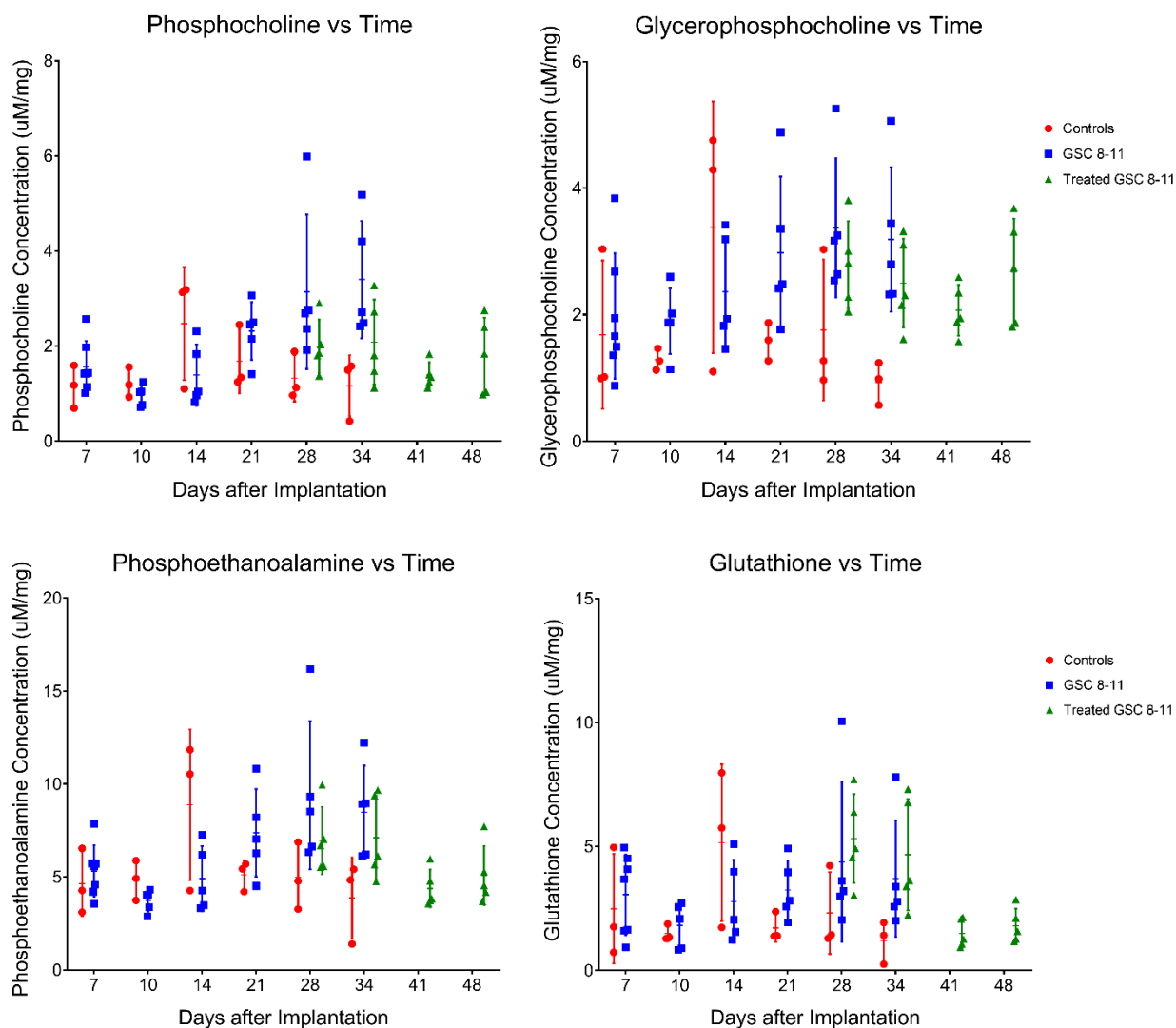


Figure 4.19: *Ex vivo* metabolite pool sizes are significantly altered throughout tumor development and regression (Part 1). Individual metabolite pool sizes, measured with NMR spectroscopy, are plotted as a function of time for control mice (red circles) and untreated (blue squares) and treated (green triangles) tumor-bearing mice. Error bars represent standard deviation.

Metabolite	Tumor Development	Tumor Regression	Potential Pathway
Valine	U34 > C34, q=0.0072	T34 < U34, q=0.0061 T41 < U34, q=0.0013 T48 < U34, q=0.0027	BCAA Catabolism
Alanine	U28 > C28, q=0.0366 U34 > C34, q=0.0027	T34 < U34, q=0.0072 T41 < U28, q=0.0063 T41 < U34, q=0.0004 T48 < U28, q=0.0149 T48 < U34, q=0.0011	Glutamine Anaplerosis
Glycine	U34 > C34, q=0.0106	T34 < U34, q=0.0457 T41 < U34, q=0.0034 T48 < U34, q=0.0021	Glycine Cleavage Folate Cycle
Phosphocholine	U28 > C28, q=0.0491 U34 > C34, q=0.0144	T41 < U28, q=0.0284 T41 < U34, q=0.0106 T48 < U34, q=0.0457	Kennedy Pathway Choline Cycle
Glycero-phosphocholine	U34 > C34, q=0.0343		
Phosphoethanolamine		T41 < U28, q=0.0154 T41 < U34, q=0.0496 T48 < U28, q=0.0401	
Glutathione		T41 < T28, q=0.0328 T48 < T28, q=0.0491	Trans-Sulphuration Pathway
NAD ⁺		T41 < U34, q=0.0106 T48 < U34, q=0.0496	Energy Metabolism

Table 4.1: List of significantly altered metabolites during tumor development and/or tumor regression. In the “Tumor Development” and “Tumor Regression” columns, the naming convention is the group (U=untreated, C=control, T=treated) followed by the time-point. For example, U34 > C34, q=0.0241 indicates that the metabolite was significantly increased in untreated tumor-bearing mice on Day 34 compared with control mice on Day 34, and the comparison produced a q-value of 0.0241. The q-values are p-values adjusted to control the false discovery rate using the two-stage step-up method of Benjamini, Krieger and Yekutieli. Pathways that the metabolites belong to which have been reported to be upregulated in cancer are also presented.

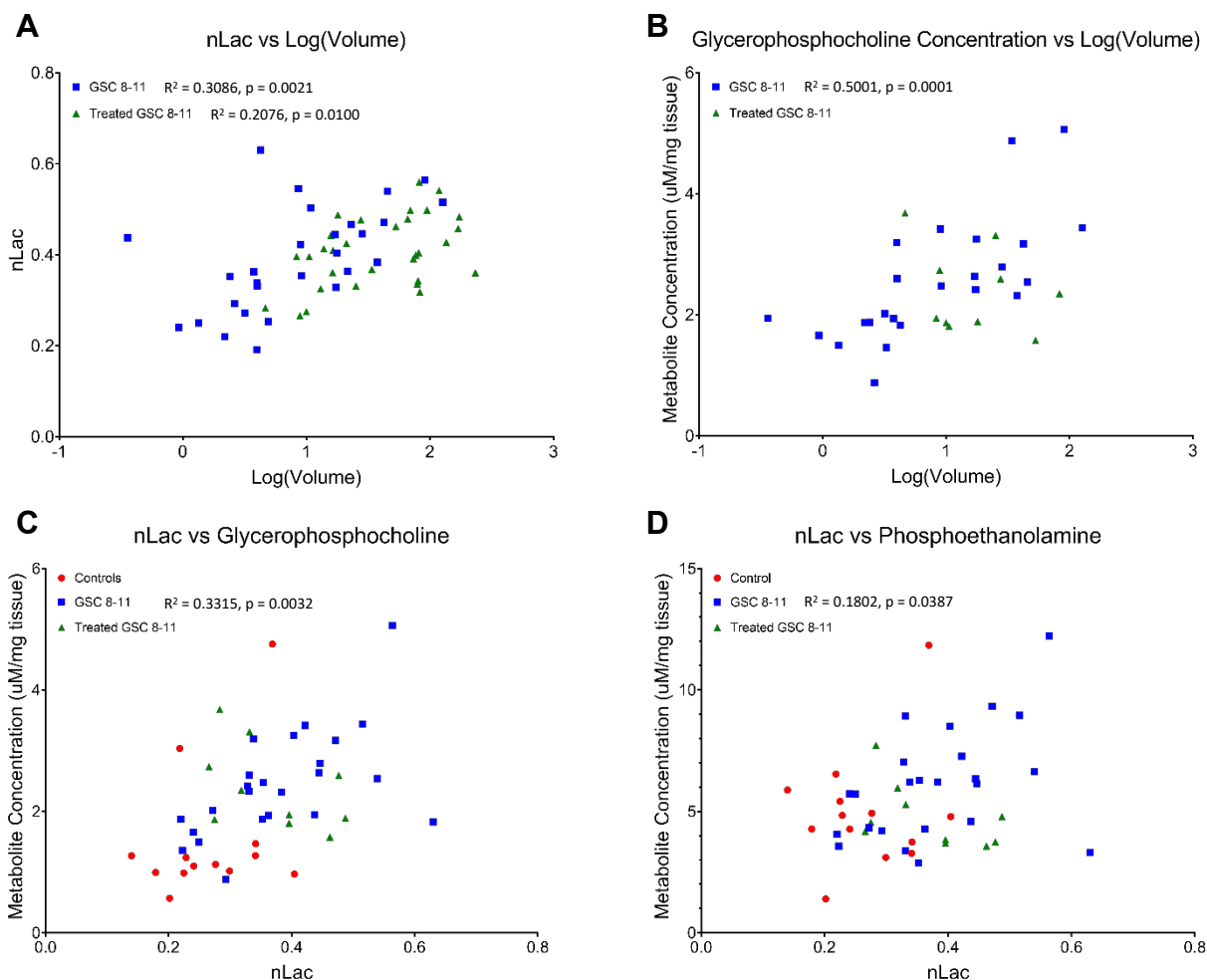


Figure 4.20: Significant correlations were observed between tumor volume, *in vivo* pyruvate-to-lactate conversion, and *ex vivo* metabolite pool sizes. The log-transformed tumor volume and nLac measurements from the same mice at the same time-points were plotted against each other and produced significant correlations in both groups of untreated and treated tumor-bearing mice (**A**). The log-transformed tumor volume values were also plot against metabolite pool sizes from the same mice at the same time-points which produced significant correlations with glycerophosphocholine among other metabolites (**B**) in untreated tumors. nLac values were then plotted against the metabolite pool sizes in the same mice at the same time-points, and significant correlations between nLac and glycerophosphocholine (**C**) and phosphoethanolamine (**D**) were observed in untreated tumors. Correlation was determined by calculating Pearson correlation coefficients and significance was attributed to correlations that produced $p < 0.05$.

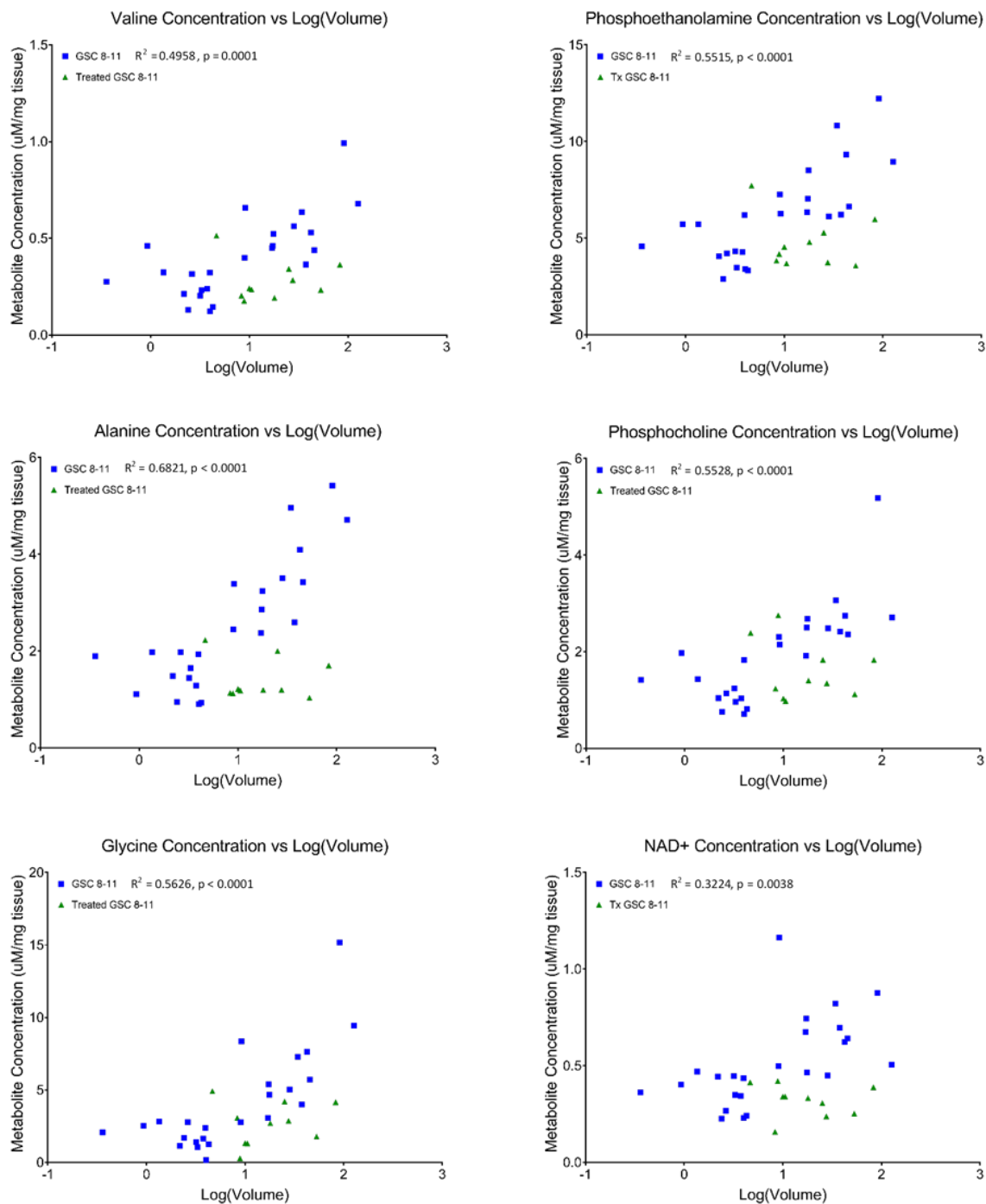


Figure 4.21: *Ex vivo* metabolite pool sizes are significantly correlated with tumor volume. Average metabolite pool sizes, measured from NMR spectroscopy, are plotted as a function of tumor volume in untreated (blue squares) and treated (green triangles) tumor-bearing mice. Correlation was determined by calculating Pearson correlation coefficients and significance was attributed to correlations that produced $p < 0.05$.

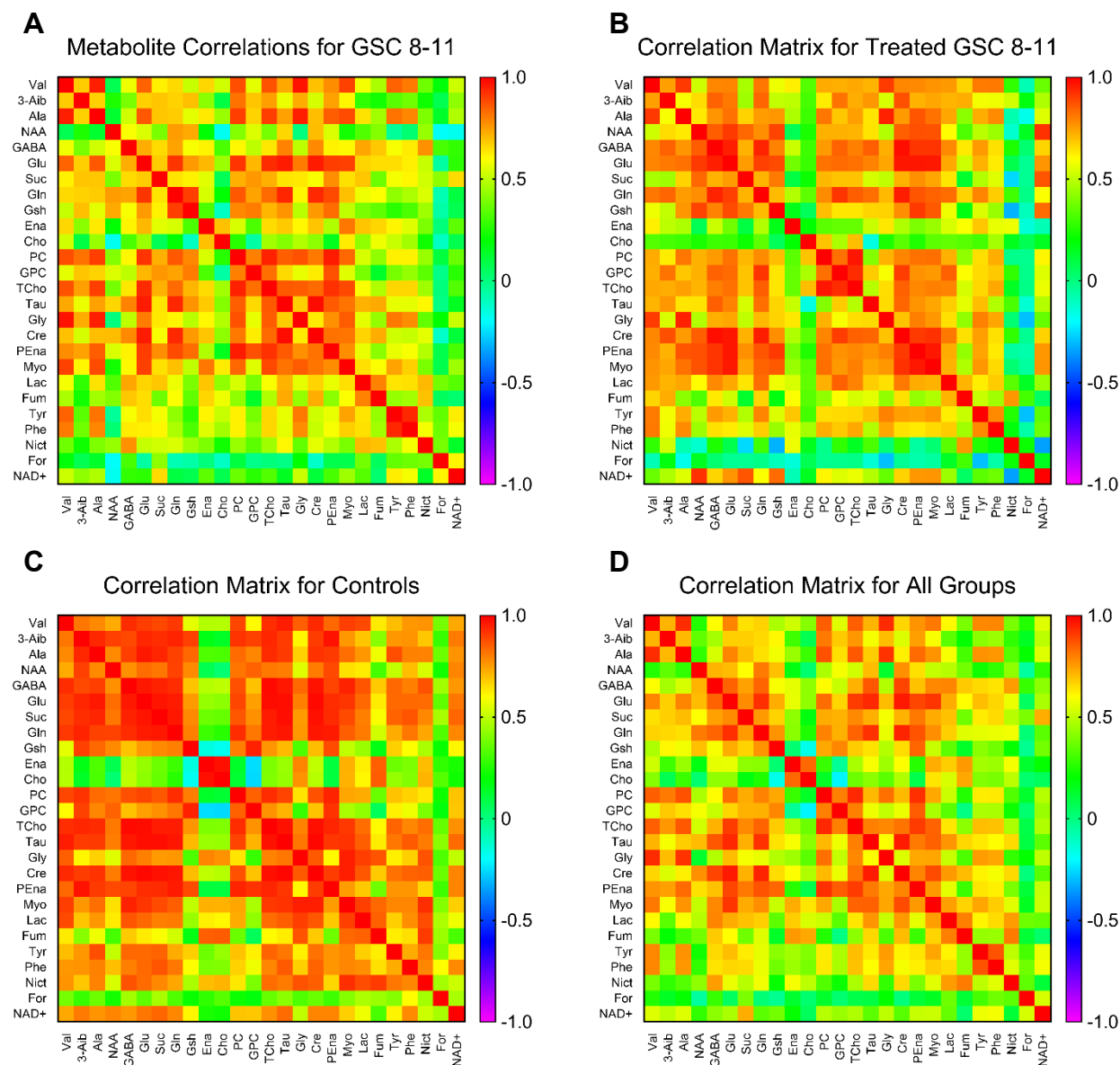


Figure 4.22: Correlations were observed between individual *ex vivo* metabolite pool sizes. Correlation matrices were created to visualize Pearson correlation coefficients between each of the metabolite pool sizes in untreated tumors **(A)**, treated tumors **(B)**, healthy brain controls **(C)**, and all groups combined **(D)**. Correlations between these metabolite pool sizes could inform on specific metabolic pathways which are up- or down-regulated during tumor development and regression.

Discussion

These findings demonstrate that *in situ* analysis of metabolic changes linking the stages of tumor progression (tumor development, regression following radiotherapy, and recurrence) using hyperpolarized MRI and NMR spectroscopy is feasible and informative. By acquiring each of these measurements, along with anatomic growth, in the same mice and at multiple common time-points, the individual evolution of the results from these assays were investigated as well as their relationship and correlation with one another. Thus, an extensive evaluation of cancer metabolism as it advances through different stages of tumor progression was examined. The mouse model used in this project is an orthotopic implantation of patient-derived GBM (GSC 8-11), which generates confidence that these results are clinically relevant and potentially translatable. However, we do acknowledge the caveat that host immunity is not fully represented in these models, which could potentially impact tumor growth, response to therapy, and metabolism.

The results from the hyperpolarized MRS experiments illustrate that measurements of pyruvate-to-lactate conversion are variable in all stages of tumor progression. Therefore, when researchers are using this technique to compare hyperpolarized pyruvate-to-lactate values between tumor types of varying growth rates or before and after treatment, the stage of tumor progression needs to be considered. Factors that could influence the production of hyperpolarized lactate in these experiments include number of cancer cells in the ROI, vascularity of the tumor, concentration of intracellular lactate, concentration of membrane pyruvate transporters such as MCT1, concentration of intracellular LDH-A, and concentration

of cofactor NADH. The number of cancer cells in the ROI is roughly estimated by the observable tumor volume, and there was a significant correlation of nLac with tumor volume in both untreated and treated tumor-bearing mice. However, only a subset of the total number of cancer cells are accounted for in tumor volume measurements. Limits in hardware resolution and SNR lead to inaccuracies of complete tumor segmentation as well as inter-observer variability. Additionally, GBM tumors are invasive and often produce microscopic satellite lesions and quiescent cells that are not detectable with current MRI techniques ¹³⁹. Lack of tumor vascularity can inhibit the influx of hyperpolarized pyruvate in the ROI, producing noisy spectra. In our hyperpolarization experiments, average maximum pyruvate SNR was nearly 7000 and was routinely over 1000. Thus, these tumors appeared to be well-vascularized.

We believe that the increased MCT1 expression observed in this study contributed to the increased pyruvate-to-lactate conversion seen throughout tumor development. Recently, we have demonstrated that after delivery of [1-¹³C]pyruvate to the extracellular space of the tumor, pyruvate transport, primarily driven by MCT1, is a key variable and often rate-limiting in these hyperpolarized pyruvate MR experiments in the context of pancreatic tumors ¹⁴⁰, and there have been additional reports of correlations of MCT1 expression and pyruvate-to-lactate conversion in GBM ⁹⁵ and breast cancer ¹³⁶. In contrast, the only significant increase of LDH-A expression was observed at the final time-point of tumor development on Day 34. *Ex vivo* lactate pool size in the GSC 8-11 tumors from NMR experiments did not reveal significant changes over the course of tumor progression. Additionally, neither untreated nor treated tumors produced significant correlations between their *in vivo* nLac values with

ex vivo lactate pool sizes, although we have observed this correlation in patient-derived pancreatic cancer mouse models of increasing aggressiveness ¹²².

In addition to probing changes in glycolytic metabolism, we were also interested in identifying alternate metabolic pathways which were potentially deregulated throughout tumor progression. These could serve as leads for subsequent imaging probes and therapeutic targets. Results from the NMR experiments of the *ex vivo* tissue samples demonstrated that amino acid metabolism was significantly altered throughout tumor progression. These metabolites are essential for protein synthesis and are necessary for cellular growth and division. In particular, the pool sizes of valine, alanine, and glycine were significantly increased by the end of tumor development and decreased following radiotherapy. These amino acids were also significantly correlated with tumor volume in untreated mice. Valine is a branched chain amino acid (BCAA) and can be used for protein synthesis or oxidized for energy production. Branched-chain aminotransferase 1 (BCAT1) generates glutamate during BCAA catabolism and is overexpressed in many cancers including glioma ^{141–144}. Alanine and α -ketoglutarate can be reversibly produced from pyruvate and glutamate through alanine transaminase (ALT) whenever the pyruvate substrate is available. In some hyperpolarized [1-¹³C]pyruvate MR experiments, it is possible to observe hyperpolarized alanine production, and a decreasing ratio of hyperpolarized alanine-to-lactate has been suggested as a biomarker of disease progression in pancreatic cancer ^{145,146}. Unfortunately, we could not reliably observe hyperpolarized alanine in our experiments to suggest the same is true for GBM. Increased glutamine anaplerosis via ALT has been linked to the viability and proliferation of brain ¹⁴⁷,

breast ^{148,149}, colorectal ¹⁵⁰, and prostate ¹⁵¹ cancers. It was recently demonstrated that alanine uptake and utilization through the SLC38A2 membrane transporter played a key role in pancreatic cancer metabolism and proliferation ¹⁵². Glycine is derived from serine in one-carbon metabolism to maintain redox balance through antioxidant production such as glutathione as well as to produce metabolites involved in purine nucleotide and lipid synthesis, all of which are important for cancer survival and proliferation ¹⁵³. Glycine production through serine hydroxymethyltransferase (SHMT)- a transcriptional target of c-Myc ¹⁵⁴- has been implicated as a driver of cancer cell proliferation in glioma ¹⁵⁵ and many other types of tumors ^{156–160}.

Many tumors rely on antioxidants to quench the effects of reactive oxygen species (ROS) produced from treatments such as radiotherapy and chemotherapy ¹⁶¹ as well as oxidative stress from increased energy metabolism ¹⁶². This is often seen through an increased production of NADPH and glutathione through the pentose phosphate pathway and one-carbon metabolism ¹⁶³. We observed a significant increase in *ex vivo* glutathione pool size in treated tumors one day following radiotherapy compared with treated tumors further into regression, which we believe is an acute response to increased ROS generated from radiotherapy. Increased concentration of antioxidants such as glutathione in tumors immediately following treatment has also been reported elsewhere ^{164,165}.

Increased phospholipid metabolism was observed in these GBM tumors compared with normal brain tissue and correlated with progression. The Kennedy pathway describes the phosphorylation of choline and ethanolamine to phosphocholine and phosphoethanolamine, which eventually form

phosphatidylcholine and phosphatidylethanolamine ¹⁶⁶. These are the two most abundant phospholipids in the cell membrane. The second messenger diacylglycerol is produced in this pathway which can further activate downstream signaling for cellular growth and fatty acid oxidation ¹⁶⁷. Phosphatidylcholine can be broken down into glycerophosphocholine for storage and eventually converted back into choline. Increased phosphocholine and choline-containing metabolite concentrations have been observed in gliomas ^{147,168–171} and many other types of cancer ^{40,172,173}, so it was not surprising to see significantly elevated pools of these metabolites, along with phosphoethanolamine in untreated tumors compared with controls and treated tumors. Furthermore, in untreated tumors, tumor volume was significantly correlated with phosphoethanolamine, phosphocholine, and glycerophosphocholine, and hyperpolarized pyruvate-to-lactate conversion was significantly correlated with phosphoethanolamine and glycerophosphocholine.

Nicotinamide adenine dinucleotide (NAD⁺) is an important cofactor in cellular metabolism and is necessary for glycolysis, pyruvate-to-lactate conversion, and serine biosynthesis. Nicotinamide phosphoribosyltransferase (NAMPT) is the main enzyme for NAD⁺ biosynthesis and has been found to be upregulated in several cancers including glioma ^{174,175}. Inhibition of this enzyme leads to antitumoral effects, which has led to the development of drugs for different types of cancer ^{176–180}. We observed a significant correlation of NAD⁺ pool size with tumor volume in untreated tumors and a significant decrease in NAD⁺ levels following treatment.

Collectively, several clinical deliverables were discussed in this study which have the potential to be implemented throughout the patient care pipeline. With

hyperpolarized MR, these include the ability to predict whether a tumor will be slow-growing or aggressive at the time of diagnosis, help discriminate pseudoprogression from true progression and predict whether patient survival will be improved shortly after administration of a treatment, and determine whether the patient is on the verge of relapse during a follow-up exam. Each of these scenarios would give physicians the time to take appropriate interventional action, improving the chances of patient survival. Additionally, we have demonstrated that *ex vivo* metabolite pool size data from NMR spectroscopy experiments varies with stage of tumor progression (particularly amino acid and phospholipid metabolism). These data can be combined with *in vivo* hyperpolarized MR data to build a model based on tumor metabolism to predict clinical outcomes. Because these data are orthogonal (with hyperpolarized MR measuring real-time flux and NMR spectroscopy measuring metabolite pool size), this model should be more predictive than either technique alone. Unfortunately, we could not implement this in our study because the tumor excision process for NMR spectroscopy requires euthanasia of the mice, preventing validation of treatment response or survival outcomes. However, in the clinical setting, biopsies of tumor tissue can be obtained during diagnosis as well as post-surgery, which could then be processed for NMR spectroscopy. Combining this data with hyperpolarized MR acquisitions at these time-points to predict clinical outcomes could form the basis for a clinical trial.

CHAPTER 5:

SUPPLEMENTAL DATA: PROFILING IMMUNOMETABOLISM

Introduction

While the role of the immune system is well-understood when it comes to most bacterial and viral infections, it is less clear where it fits in the context of cancer ¹⁸¹. By 1960, Sir Macfarlane Burnet and Lewis Thomas proposed the theory of cancer immunosurveillance which stated that one primary role of the immune system was to maintain tissue homeostasis by recognizing small groups of tumor cells by their newly presenting antigens and removing them before they present clinically ^{182,183}. Ideally, natural killer (NK) cells, CD8⁺ cytotoxic T-cells, and CD4⁺ helper T-cells eradicate abnormally behaving cells through interferon- γ and other cytotoxins ¹⁸⁴. While a functioning immune system does reduce the risk of cancer ¹⁸⁵, it is not capable of preventing all cases, and it can even be co-opted to promote the formation of tumors and progression to late-stage metastatic cancer ¹⁸⁶. It has been suggested that the combination of genomic instability and immunoediting, which involves the selection pressure for non-immunogenic cells, is what allows some tumors to survive and thrive amongst an otherwise functioning immune system ¹⁸⁷.

Because cancer originates from normal, healthy cells, some cancer cells can initially avoid immunosurveillance until sufficient genetic modifications occur through mutations and neoantigens are presented on their surface. However, the degree of tumor antigen presentation is highly variable among tumors ¹⁸⁸, and some tumors can evade the immune system by shedding these antigens or making them inaccessible ^{189,190}. Furthermore, cancer cells can express membrane proteins and

secrete molecules (which include, but are not limited to, programmed death-ligand 1 (PD-L1), transforming growth factor (TGF)- β , tumor necrosis factor (TNF)- α , colony stimulating factor (CSF)-1, interleukin (IL)-1, IL-6, IL-8, and IL-10) in order to attenuate the effectiveness of cytotoxic immune cells ¹⁹¹. Secreted chemokines can also shift the Th1/Th2 balance by recruiting immune cells such as CD4⁺CD25⁺FOXP3⁺ regulatory T-cells and myeloid-derived suppressor cells (MDSC) to help protect the tumor from cytotoxic immune cells and promote tumor growth ^{192–195}. This process of evading the immune system has emerged as a hallmark of cancer ¹⁹⁶.

Immunotherapy has recently emerged as the fourth pillar of cancer treatment and has taken many forms to modulate the immune system to improve response. These include cancer vaccines, genetically modified immune cells, and checkpoint blockades ¹⁹¹. The last of which has found great success in some forms of cancer, even in late-stage metastatic disease, and its pioneers were recently awarded the Nobel Prize in Medicine for their efforts ¹⁹⁷. The immune system is also involved with other types of treatment. Radiotherapy and chemotherapy often result in inflammation around the tumor. It is difficult to distinguish between tumor and inflammation with conventional imaging, and it is often the cause of apparent pseudoprogression ¹⁹⁸.

The following projects were performed in collaboration with laboratories at MD Anderson as part of larger studies. As such, the following data are mostly preliminary and either serve as supporting data or the foundation for larger projects. The common theme between the projects is the use of NMR spectroscopy to metabolically profile immune cells in an effort to distinguish between anti-tumor and pro-tumor activity,

monitor treatment response from immunotherapy, and potentially distinguish between inflammation/ pseudoprogression and true progression.

Metabolic Profiling of Licensed and Unlicensed Natural Killer Cells

This section is based upon and reproduced with permission from:

Schafer JR, Salzillo TC, Chakravarti N, Kararoudi MN, Trikha P, Foltz JA, Wang R, Li S, Lee DA. Education-dependent activation of glycolysis promotes the cytolytic potency of licensed human natural killer cells. *Journal of Allergy and Clinical Immunology*. 2019;143(1):346-358.e6. (License number: 1049029-4)

Introduction

NK cells belong to the innate immune system and respond to activated stress signals on cells that are affected by infection or malignant transformation ¹⁹⁹ by producing cytotoxic effects and producing cytokines such as INF- γ to prime other immune cells for response ²⁰⁰. NK cells respond to both allogenic and nonallogenic cells, and their resultant cytotoxic effect is a result of the balance between activation and inhibitory signaling ²⁰¹. During maturation, in a process known as education ²⁰², bone-marrow-derived NK cells which possess inhibitory killer cell Ig-like (KIR) receptors (or Ly49 in mice) are “licensed” by major histocompatibility complex (MHC) class 1 molecules and have been shown to have enhanced proliferation and mature cytotoxic and cytokine production functionality ²⁰³. This is also known as the arming model. A minority of NK cells which do not possess the inhibitory receptors are “unlicensed” and are hyporesponsive and functionally defective in most cases ²⁰⁴.

Once a NK cell binds to a distressed cell, the NK cell’s functionality is adapted based on the presence or absence of MHC class 1 molecules on the bound cell ²⁰⁵. Chronic binding between MHC class 1 molecules and KIR receptors on the licensed

NK cells allows the NK cells to recognize a bound cell as self and produces inhibitory and disarming effects²⁰⁶. Thus, both unlicensed and licensed NK cells are self-tolerant as unlicensed cells are hyporesponsive²⁰⁷ while licensed cells are eventually inhibited after chronic exposure to MHC class 1 molecules²⁰⁸. In response to cells which are absent of MHC class 1 molecules, licensed NK cells can mount an unattenuated cytotoxic and cytokine production effector response, while unlicensed cells still remain hyporesponsive²⁰². It is hypothesized that alternate methods of NK cell education exist, and that unlicensed NK cells can become activated unconventionally^{209,210}. Furthermore, while uneducated NK cells are characterized by hyporesponse and higher threshold for activity, their lack of inhibitory receptors do give them utility in fighting persistent diseases with a high expression of MHC class 1 molecules such as some viruses and cancers^{211–213}. In the tumors that downregulate their MHC class 1 expression, adoptive therapy with NK cells has shown promise as an effective immunotherapy^{214–217}.

The goal of this study was to characterize the mechanism of enhanced function of licensed NK cells for degranulation and cytokine production in targets expressing MHC class 1 molecules²¹⁸. Initial experiments using reverse-phase protein array showed that several proteins involved in metabolism such as MIF, MTCO2, SDHB, and PKM2 were overexpressed in licensed NK cells compared with unlicensed cells. Thus, metabolic profiling of licensed and unlicensed NK cells was performed to support these findings.

Methods

Preparation of the licensed and unlicensed NK cells for metabolic profiling was performed according to prior literature ²¹⁸ and as described by the authors as follows.

Human Subjects: NK cells were derived from peripheral blood or buffy coats of healthy volunteer donors under the MD Anderson Cancer Center IRB-approved protocol LAB07-0296 or IRB exemption PA13-0978.

NK Cell Isolation: NK cells were isolated from whole blood or buffy coats using Rosette-Sep (Stem Cell Technologies) density-gradient centrifugation as previously described ²¹⁹.

KIR and HLA Typing: DNA was isolated from NK cells and submitted to the HLA laboratory at the University of Texas MD Anderson Cancer Center for HLA and KIR typing. HLA typing was performed at the intermediate-resolution level at HLA-A, HLA-B, and HLA-C loci by PCR amplification and oligonucleotide hybridization (One Lambda). KIR genotyping was performed with reverse sequence-specific oligonucleotide methodology using fluorescently labeled beads conjugated to oligonucleotide probes (One Lambda). The HLA group for KIR binding was determined using the KIR Ligand Calculator maintained by the European Bioinformatics Institute of the European Molecular Biology Labs (EMBL-EBI) (<http://www.ebi.ac.uk/ipd/kir/ligand.html>).

Licensed and Unlicensed NK cell discrimination: To avoid confounding from expression of multiple KIRs, here we identified licensed and unlicensed NK cells as those expressing a single inhibitory KIR in an individual who has or lacks, respectively,

the relevant cognate HLA ligand and lacks a complementary activating KIR (e.g., KIR2DL1+KIR2DL2/3–KIR3DL1– NK cells in an HLA-C*0201 individual who lacks the KIR2DS1 gene). Licensed status was determined irrespective of NKG2A expression.

Flow Cytometry: NK cells were labeled with fluorescently conjugated human antibodies to determine licensed and unlicensed NK cell populations: CD56 PerCP CY5.5 (Biolegend), CD3 APC Cy7 (Biolegend), KIR2DL1 FITC (R&D), KIR2DL2/3 APC (Miltenyi), and KIR3DL1 PE (Beckman Coulter). Cells were stained with antibodies at concentrations according to manufacturer guidelines and titrated when necessary. For intracellular staining, cells were washed with staining buffer containing phosphate buffered saline (PBS) and 5% fetal bovine serum (FBS). Cells were fixed in 2% formaldehyde for 10 minutes, then washed and permeabilized with methanol on ice for 10 minutes. They were then washed with staining buffer, followed by staining for p-38 MAPK (D13E1) antibody (Cell Signaling Technologies). Flow cytometry was performed on an LSR Fortessa (BD Biosciences).

Cell Sorting: Cells were labeled with the following fluorescently conjugated human antibodies: CD56 PerCP CY5.5 (Biolegend), CD3 APC Cy7 (Biolegend), KIR2DL1 FITC (R&D), KIR2DL2/3 APC (Miltenyi), and KIR3DL1 PE (Beckman Coulter). Cells were stained with antibodies at concentrations according to manufacturer guidelines and titrated when necessary. Cells were sorted using a FACS Aria IIu sorter (BD Biosciences).

Cell Expansion: To generate sufficient numbers of unlicensed NK cells for phenotypic and metabolic studies, freshly isolated or flow-sorted single-KIR+ NK cells were expanded by stimulation with K562 Clone9.mbIL21 feeder cells for 14–21 days as

previously described ²²⁰. Briefly, irradiated K562 Clone9.mblL21 feeder cells were added to the NK cell culture conditions at a ratio of 2:1 at day 1 and 1:1 at days 7 and 14.

Cell Culture: Mononuclear cells from peripheral blood were cultured in RPMI 1640 Medium supplemented with 50 IU/mL recombinant human IL-2, 10% FBS, L-glutamine, and penicillin/streptomycin, as previously described ²²⁰. The medium was changed every other day.

Sample Preparation for Metabolic Profiling: 10 million cells were spun down into pellets and frozen on dry ice for metabolic profiling. Extraction of water-soluble metabolites is the same procedure as described in **GENERAL METHODS** (Chapter 2) except that because cells were used instead of tissue, the pulverizing and weighting steps were skipped, and the cell pellets were immediately lysed and vortexed in the methanol-water solution. All other procedures for metabolite extraction, NMR spectroscopy, and metabolite pool size measurements were followed as described in **GENERAL METHODS**.

Statistical Analysis of *Ex Vivo* Metabolite Pool Size Measurements: Metabolite pool sizes in units of μM per 10 million cells were calculated in $N = 4$ licensed and $N = 4$ unlicensed samples. Statistical significance was determined between the two groups using unpaired two-tailed T-tests for each identified metabolite. Significance was attributed to comparisons that produced $p < 0.05$.

Results and Discussion

In licensed NK cells, the pool sizes of glutamate, aspartate, and taurine were significantly decreased compared with unlicensed NK cells (Fig. 5.1). This was accompanied by non-significant increases in acetate and lactate in licensed NK cells compared with unlicensed cells. Both glutamate and aspartate can be catabolized into the TCA cycle to provide substrates for oxidative phosphorylation ²²¹. Additionally, taurine is an antioxidant which is beneficial to quench the excess reactive oxygen species produced from oxidative phosphorylation ²²².

Additional experiments in this study, which were performed by Jolie R. Schafer, who is the first-author of this manuscript, demonstrated from Seahorse assays that licensed NK cells possessed a significantly higher extracellular acidification rate (ECAR) compared with unlicensed cells, and thus higher rates of glycolysis and glycolytic capacity. Oxygen consumption rate (OCR) was similar between the two NK cell types, which suggests that mitochondrial respiration through oxidative phosphorylation was unchanged.

Metabolic inhibition with the glycolytic inhibitor, 2-DG, did not reduce cytotoxic potential for either NK cell type. Licensed NK cell cytotoxicity was only significantly reduced when 2-DG administration was combined with glucose starvation. When the oxidative phosphorylation inhibitor, oligomycin, was administered, unlicensed NK cell cytotoxicity was drastically reduced whereas licensed NK cell cytotoxicity was only modestly affected.

Taken collectively, it was postulated that licensed NK cells utilized both glycolysis and oxidative phosphorylation during activation whereas unlicensed cells primarily relied on oxidative phosphorylation. This increase in glycolysis and rapid generation of ATP could be instrumental in cytotoxic activities in licensed NK cells.

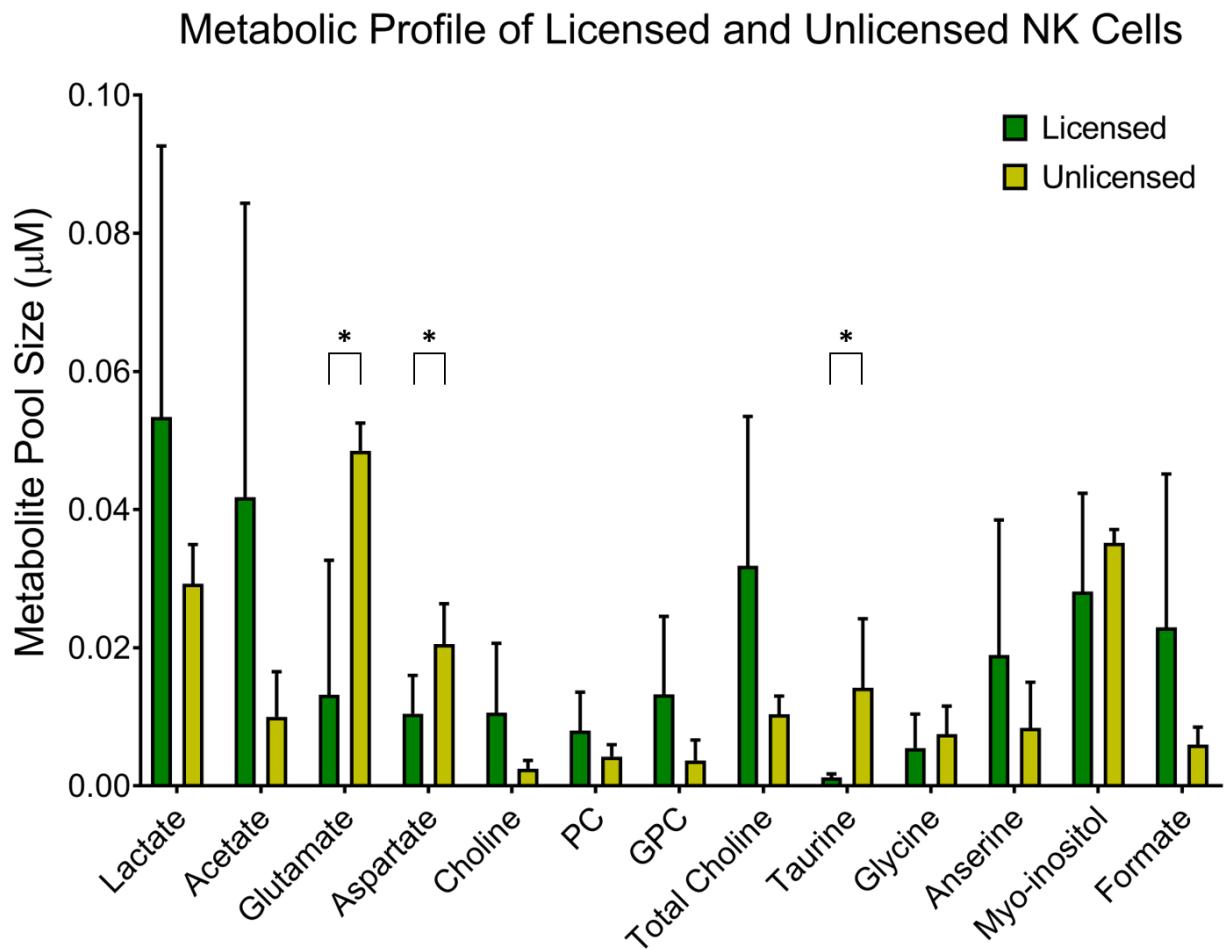


Figure 5.1: Metabolic profiling of licensed and unlicensed natural killer cells. Licensed and unlicensed NK cell samples were metabolically profiled using NMR spectroscopy, and the above metabolites were identified and quantified. Error bars represent standard deviation. Average metabolite concentration between the two groups was tested for significance using unpaired two-tailed T-tests for each identified metabolite. Significance was attributed to comparisons that produced $p < 0.05$. * $p < 0.05$.

Metabolic Profiling of CD14⁺ Monocytes and Polarized Macrophages

Introduction

Monocytes are leukocytes that are produced in the bone marrow and released into the bloodstream. They eventually migrate into different tissues and differentiate into macrophages, dendritic cells, and osteoclasts ²²³. Monocytes are often divided into two established subsets. Monocytes with CD14^{hi}CD16⁻ expression are known as classic monocytes, express CCR2 chemokine receptors, and are recruited to areas of inflammation. The other, CD14⁺CD16⁺ monocytes, share a similar phenotype as mature tissue-resident macrophages and express CCR5 chemokine receptors ²²⁴. Circulating monocytes can be recruited to different tissues to replenish the tissue-resident macrophage population (such as alveolar space in lungs, central nervous system, and spleen). In the central nervous system, the majority of myeloid cells are microglia and macrophages derived from peripheral blood monocytes ²²⁵.

Monocytes are also recruited to areas of inflammation where they differentiate into macrophages. These macrophages can be activated into different states depending on surrounding stimulating factors and possess distinct properties in regards to morphology, cell surface markers, and cytokine production ²²⁵. The classically-activated state (M1) is proinflammatory and is stimulated by IFN- γ and lipopolysaccharide (LPS) ²²⁶. The alternatively-activated state (M2) is associated with tissue repair and increased mannose-receptor activity and is induced by IL-4 and IL-13 ^{227,228}. M2 macrophages have also been implicated in the remodeling of the extracellular matrix and angiogenesis ^{229,230}. Therefore, it is hypothesized that tumor-associated macrophages (TAM) represent the M2 phenotype and help cultivate a

tumor-promoting and immunosuppressive microenvironment^{231–233}. It has also been suggested that TAM are heterogeneous and are comprised of primarily M1 macrophages state in early-stage tumors whereas M2 phenotypes are dominant in late-stage and hypoxic tumors^{181,234}. In GBM, M2 TAM represent the majority of immune-infiltrating cells¹⁹⁵. It is still under debate whether macrophages belong to only one of the discrete states or reside in a spectrum of states with variable expression of the different phenotypes. Furthermore, it is not determined whether macrophages permanently differentiate into one of the states or if there is plasticity between them^{223,235}.

The purpose of this study was to elucidate metabolic differences between peripheral blood and tissue-residing CD14⁺ monocytes from GBM patients and healthy volunteers. In addition, the metabolic profiles of unpolarized (M0), M1, and M2 macrophages were investigated. The goal was to append this data to a larger set of experiments to potentially identify a metabolic mechanism for macrophage activation which could be applied to non-invasive imaging or metabolic therapy.

Methods

Human Subjects: This study was conducted under protocols LAB03-0687 and LAB06-0008, which were approved by the Institutional Review Board of The University of Texas MD Anderson Cancer Center. The Research Ethics Board of McGill University approved the use of nonidentifiable tissues for research. Patient tumors were graded pathologically as newly diagnosed adult glioblastoma (N = 3) by a neuropathologist according to the World Health Organization classification. At least 2 g of viable, nonnecrotic tumor was required to obtain sufficient quantities of immune cells for analysis and was processed within 1 hour after resection. Peripheral blood was drawn from the patients intra-operatively and from healthy donors. Control CD14⁺ cells (general marker of myeloid lineage cells) (N = 3) were derived from tissue samples surgically resected from nonmalignant cases of intractable epilepsy (Montreal Neurological Institute). These samples were obtained from tissues removed during the approach to the lesion site. Human glioblastoma or nonmalignant central nervous system tissue was digested with Liberase TM Research Grade Enzyme (Roche Diagnostics). After enzymatic digestion, myelin was removed by centrifugation in a Percoll gradient.

Isolation of Myeloid Cells from Fresh Human Glioblastoma Tissue: Freshly resected human glioblastoma tissue was minced into small pieces using a scalpel, dissociated using a Pasteur pipette, and suspended in Roswell Park Memorial Institute (RPMI) 1640 medium with L-glutamine (Mediatech Inc.) containing Liberase TM Research Grade Enzyme at a final concentration of 30 µg/mL. The prepared mixture was incubated for 1 h at 37°C with agitation. After brief centrifugation, the pellet was

resuspended in 20 mL of 1.03 Percoll underlaid with 10 mL of 1.095 Percoll and overlaid with 10 mL of fluorescence-activated cell sorter buffer (5% FBS, MilliporeSigma) in PBS (Mediatech Inc.). The tube was centrifuged at 1,200 g for 20 min at room temperature with no brake. After centrifugation, the cell layer on top of the 1.095 Percoll was collected, filtered through a 70- μ m nylon strainer (BD Biosciences), washed, stained with Trypan blue dye (MilliporeSigma), and counted in a Neubauer chamber (Fisher Scientific). Afterward, myeloid cells were blocked for nonspecific binding using Fc γ R-binding inhibitor (Miltenyi Biotec) and magnetically labeled with CD14 microbeads (Miltenyi Biotec) at 4° C for 30 min. The cell suspension was loaded onto a MACS Column (Miltenyi Biotec) in the magnetic field. The negative fraction was discharged. Upon removal of the column from the MACS separation system, CD14⁺ cells were eluted as positive fractions.

Isolation of Microglia from Human Nontumoral Tissue: Samples of brain tissue surgically resected from cases of intractable epilepsy of nonmalignant origin were processed as described previously ²²⁵, and microglia were separated magnetically with CD14 microbeads.

Isolation of CD14⁺ Monocytes: Peripheral blood mononuclear cells (PBMCs) were purified from 3 healthy blood donors (Gulf Coast Blood Center, Houston, Texas), 3 healthy donors (volunteers), and from 3 glioblastoma patients undergoing resection at The University of Texas MD Anderson Cancer Center by centrifugation on a Ficoll-Hypaque density gradient (MilliporeSigma) ²³⁶. CD14⁺ monocytes were isolated from PBMCs via positive selection using CD14 microbeads (Miltenyi Biotec) as per the manufacturer's instructions.

Monocyte Differentiation into the M0, M1, M2A, or M2C Phenotype: Monocytes were cultured in RPMI 1640 medium containing L-glutamine (Mediatech Inc.), 20% heat-inactivated FBS (MilliporeSigma) without penicillin and streptomycin. Nonpolarized M0 macrophages were generated by culturing monocytes in medium with granulocyte-macrophage colony-stimulating factor (GM-CSF; 50 ng/mL) and harvested on day 4. M1 and M2 macrophages were cultured in medium with GM-CSF (50 ng/mL) and macrophage colony-stimulating factor (M-CSF; 100 ng/mL), respectively. On day 4, 50% of complete, fresh M1 or M2 monocyte medium was added for 48 h. Further polarization was achieved by removing the medium and culturing cells for additional 48 h in fresh medium with GM-CSF (50 ng/mL), lipopolysaccharide from *Escherichia coli* 055:B5 (100 ng/mL; MilliporeSigma), IFN- γ (50 ng/mL; Peprotech), and TNF- α (20 ng/mL; Peprotech) for M1 polarization; M-CSF (100 ng/mL) and IL-4 (20 ng/mL; R&D Systems) for M2A polarization; M-CSF (100 ng/mL), IL-10 (10 ng/mL; Peprotech) and TGF- β 1 (10 ng/mL; Peprotech) for M2C polarization. On day 8, M1, M2a, and M2c macrophages were harvested.

Sample Preparation for Metabolic Profiling: 10 million cells were spun down into pellets and frozen on dry ice for metabolic profiling. Extraction of water-soluble metabolites is the same procedure as described in **GENERAL METHODS** (Chapter 2) except that because cells were used instead of tissue, the pulverizing and weighting steps were skipped, and the cell pellets were immediately lysed and vortexed in the methanol-water solution. All other procedures for metabolite extraction, NMR spectroscopy, and metabolite pool size measurements were followed as described in **GENERAL METHODS**.

Statistical Analysis of *Ex Vivo* Metabolite Pool Size Measurements: Metabolite pool sizes in units of μM per 10 million cells were calculated in each of the $N = 3$ CD14⁺ monocytes and polarized macrophage cell samples. Statistical significance for each metabolite was determined using ordinary one-way ANOVA and follow-up Fisher's Least Significant Difference tests. Due to the large number of comparisons (each set of comparisons made for 24 metabolites), the false discovery rate was controlled using the two-stage step-up method of Benjamini, Krieger and Yekutieli ($Q < 0.05$).

Results and Discussion

33 metabolites were identified which appeared in at least one of the NMR spectra. After disqualifying the metabolites which were present in only a sparse number of samples or whose resonances were consistently convolved with other metabolite peaks, there were 24 metabolites considered for quantification and statistical analysis. The group of metabolites consists of several amino acids, lipids, and carbohydrates.

The metabolomic profiles of CD14⁺ blood cells isolated from glioblastoma patients and healthy blood donors, and CD14⁺ cells isolated from freshly resected glioblastoma tissue or nonmalignant surgical samples were examined. The analysis revealed concentrations of 3 metabolites reached statistical significance. Acetate, propionate, and formate were all elevated in blood- and tissue-derived CD14⁺ cells from GBM patients compared to those from healthy donors (Fig. 5.2).

The metabolomic profiles of nonpolarized (M0), classically-activated (M1), and alternatively-activated (M2A, M2C) macrophages were investigated. Five metabolites reached statistical significance (Fig. 5.3). Acetate had markedly higher concentration in M0, M2A, and M2C macrophages than M1 macrophages. Glutamate was elevated in M2A macrophages compared to other groups. Increased glutamate could be the result of upregulated arginine-to-ornithine conversion which occurs in M2 macrophages^{237–239}. In contrast, M1 macrophages utilize most of their arginine in cytotoxic NOS production. Taurine was downregulated in M0 macrophages compared to the other groups and was elevated in M2A macrophages compared to M1 and M2C groups. Lactate was upregulated in M2A and M2C macrophages compared to M0

macrophages which could be a result of increased glycolysis in these subtypes. Formate was elevated in M0 macrophages compared to the other groups.

These data elucidate only one dimension of the metabolism of tumor-associated monocytes and the mechanism behind macrophage polarization and should be combined with genotyping or protein expression data to perform an integrated pathway analysis to look deeper into these processes. Furthermore, phantoms containing these cells could be scanned on an MR spectrometer to test the feasibility of using clinical ^1H MRS to detect monocyte involvement and macrophage polarization. However, advanced pulse sequences such as spectral editing and efficient fat/water suppression would most likely be required to detect the subtle differences in relative metabolite concentration.

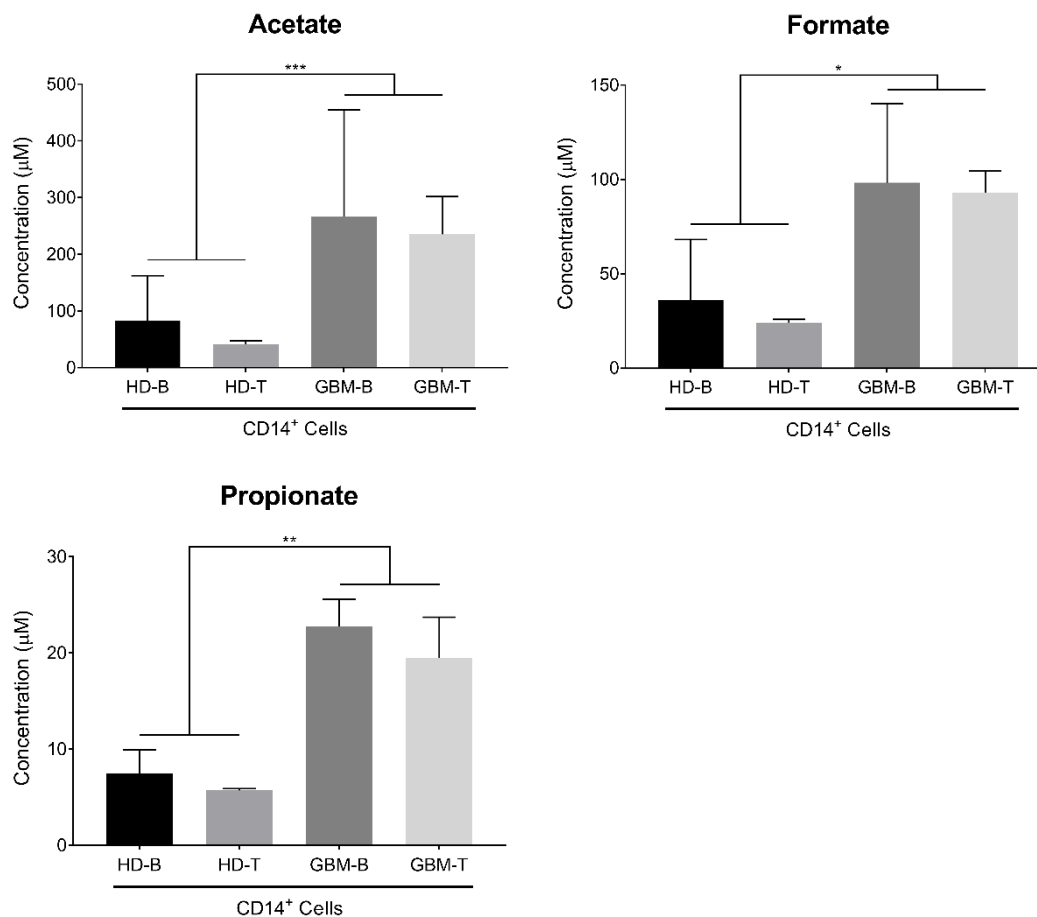


Figure 5.2: Significantly altered metabolites in CD14⁺ monocytes residing in blood (-B) and tissue (-T) samples from healthy donors (HD) and GBM patients. Error bars represent standard deviation. Statistical significance was determined using ordinary one-way ANOVA and follow-up Fisher's Least Significant Difference tests. The false discovery rate was controlled using the two-stage step-up method of Benjamini, Krieger and Yekutieli, and significance was attributed to comparisons that produced $q < 0.05$. * $q < 0.05$.

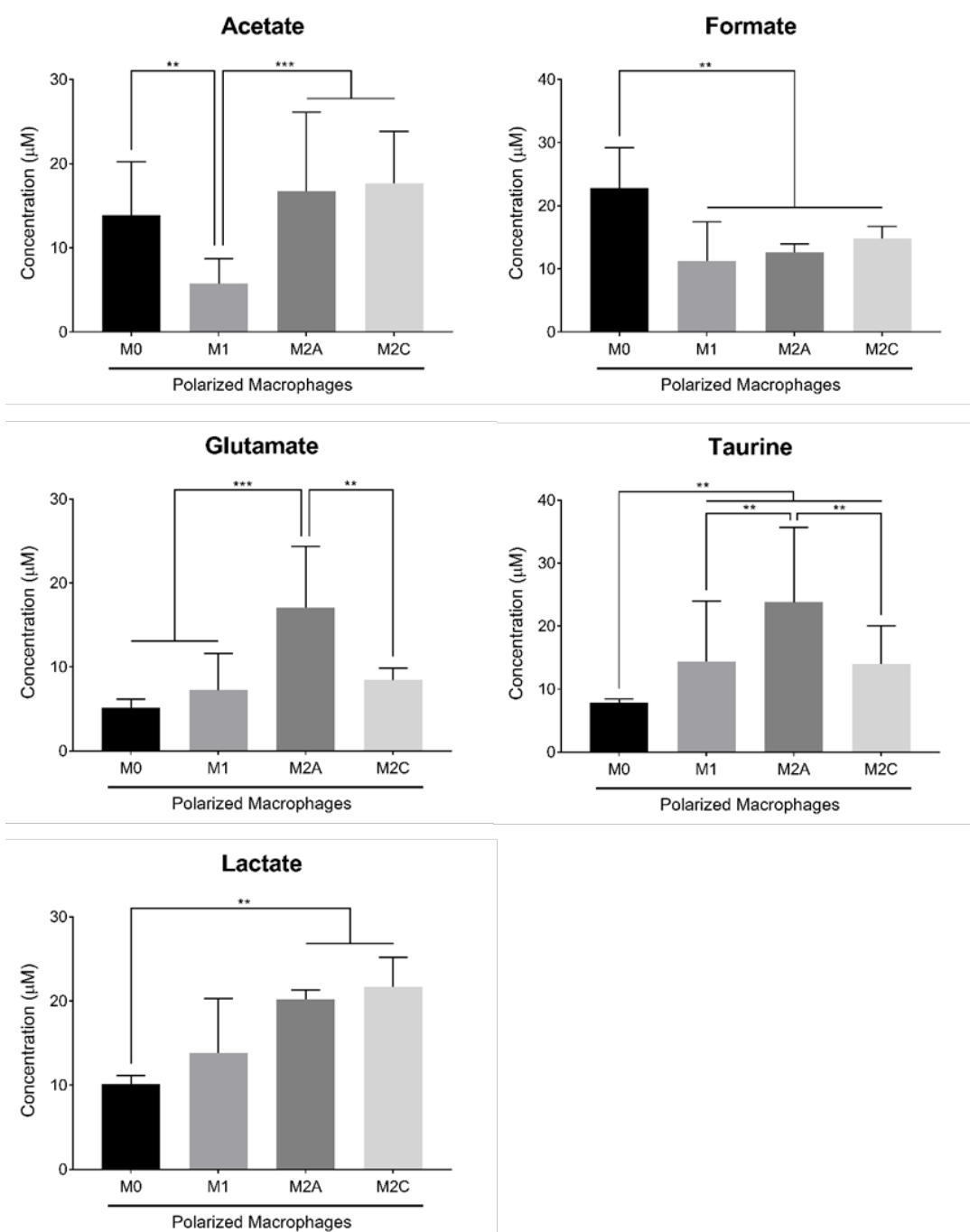


Figure 5.3: Significantly altered metabolites in unpolarized (M0), classically activated (M1) and alternatively activated (M2A, M2C) macrophages. Error bars represent standard deviation. Statistical significance was determined using ordinary one-way ANOVA and follow-up Fisher's Least Significant Difference tests. The false discovery rate was controlled using the two-stage step-up method of Benjamini, Krieger and Yekutieli, and significance was attributed to comparisons that produced $q < 0.05$. * $q < 0.05$.

CHAPTER 6:

CONCLUDING REMARKS

Several aspects of brain tumor metabolism and immunometabolism were investigated and discussed. With regards to the main body of work discussed in **CHAPTER 4**, this is the most comprehensive longitudinal study using hyperpolarized MR to probe tumor metabolism to my knowledge. Not only were data acquired from several time-points which spanned the entirety of tumor progression (development, regression, and recurrence), they were acquired using multiple modalities (anatomic MRI, hyperpolarized MRS, NMR spectroscopy, and immunohistochemistry) which evaluated orthogonal aspects of tumor progression (anatomic growth, real-time metabolic conversion, steady-state metabolite pool size, and protein expression). Because each class of data were acquired at the same time-points, the individual evolution as well as the interrelationship of the variables could be studied. The main purpose of this work was to highlight the capabilities of the novel imaging technique of hyperpolarized MR which can measure real-time metabolic activity *in vivo*. The use of this technology to measure hyperpolarized pyruvate-to-lactate conversion is currently in clinical trials, and this project demonstrated the value that it could add to routine imaging of cancer by addressing several clinical challenges (predicting aggressive expansion of tumors during development, distinguishing between true progression and pseudoprogression following treatment, predicting treatment outcomes, quantifying treatment response, and predicting tumor relapse). Therefore, there are both clinical and scientific implications of this study.

An improvement in this study would be to implement a more aggressive treatment regimen to induce a greater reduction in tumor burden. This could be in the form of increased dose of radiotherapy- either whole-brain or targeted with 3-D planning or intensity-modulated to reduce toxicity- or with adjuvant chemo-, targeted-, or immunotherapy. Doing so would increase the magnitude of tumor volume and metabolic changes which could lead to discovery or more nuanced alterations. Additionally, the period of remission would be extended which would allow more measurements to be acquired and could lead to the diagnosis of transient responses such as a gain of treatment resistance. Each of these aspects are directions for future work. Furthermore, this study would benefit from a similar analysis with another GBM line such as a different GSC mouse model to determine if it is a general pattern among brain tumors. Eventually, one could work his/her way back to the goal discussed in **CHAPTER 3** of trying to predict tumor aggressiveness with hyperpolarized MR which would also be of immense value to the clinic. As hyperpolarized MR makes its way through clinical trials as a metabolic imaging modality, we believe its value in cancer care will continue to grow. Just as PET imaging became a staple in the clinic, so too should hyperpolarized MRI as an invaluable tool for interrogating the metabolism of cancer.

Lastly, the concept of immunometabolism was discussed in **CHAPTER 5** in the context of two projects- one that was part of a larger study for investigating NK cell education, and the other that could form the foundation of a new project to probe macrophage metabolism. This discussion was primarily to introduce a couple of routes

that metabolic profiling could be applied to immunology and highlight the work I conducted in collaboration with other laboratories at MD Anderson.

BIBLIOGRAPHY

1. Ostrom QT, Cioffi G, Gittleman H, Patil N, Waite K, Kruchko C, Barnholtz-Sloan JS. CBTRUS Statistical Report: Primary Brain and Other Central Nervous System Tumors Diagnosed in the United States in 2012–2016. *Neuro-Oncology*. 2019;21(Supplement_5):v1-v100.
2. Stupp R, Hegi ME, Mason WP, van den Bent MJ, Taphoorn MJ, Janzer RC, Ludwin SK, Allgeier A, Fisher B, Belanger K, Hau P, Brandes AA, Gijtenbeek J, Marosi C, Vecht CJ, Mokhtari K, Wesseling P, Villa S, Eisenhauer E, Gorlia T, Weller M, Lacombe D, Cairncross JG, Mirimanoff R-O. Effects of radiotherapy with concomitant and adjuvant temozolomide versus radiotherapy alone on survival in glioblastoma in a randomised phase III study: 5-year analysis of the EORTC-NCIC trial. *The Lancet Oncology*. 2009;10(5):459-466.
3. Brem H, Piantadosi S, Burger P., Walker M, Selker R, Vick N., Black K, Sisti M, Brem S, Mohr G, Muller P, Morawetz R, Schold S. Placebo-controlled trial of safety and efficacy of intraoperative controlled delivery by biodegradable polymers of chemotherapy for recurrent gliomas. *The Lancet*. 1995;345(8956):1008-1012.
4. Westphal M, Hilt DC, Bortey E, Delavault P, Olivares R, Warnke PC, Whittle IR, Jääskeläinen J, Ram Z. A phase 3 trial of local chemotherapy with biodegradable carmustine (BCNU) wafers (Gliadel wafers) in patients with primary malignant glioma. *Neuro-Oncology*. 2003;5(2):79-88.

5. Gilbert MR, Dignam JJ, Armstrong TS, Wefel JS, Blumenthal DT, Vogelbaum MA, Colman H, Chakravarti A, Pugh S, Won M, Jeraj R, Brown PD, Jaeckle KA, Schiff D, Stieber VW, Brachman DG, Werner-Wasik M, Tremont-Lukats IW, Sulman EP, Aldape KD, Curran WJ, Mehta MP. A Randomized Trial of Bevacizumab for Newly Diagnosed Glioblastoma. *New England Journal of Medicine*. 2014;370(8):699-708.
6. Wick W, Gorlia T, Bendszus M, Taphoorn M, Sahm F, Harting I, Brandes AA, Taal W, Domont J, Idbaih A, Campone M, Clement PM, Stupp R, Fabbro M, Le Rhun E, Dubois F, Weller M, von Deimling A, Golfopoulos V, Bromberg JC, Platten M, Klein M, van den Bent MJ. Lomustine and Bevacizumab in Progressive Glioblastoma. *New England Journal of Medicine*. 2017;377(20):1954-1963.
7. Stupp R, Taillibert S, Kanner AA, Kesari S, Steinberg DM, Toms SA, Taylor LP, Lieberman F, Silvani A, Fink KL, Barnett GH, Zhu J-J, Henson JW, Engelhard HH, Chen TC, Tran DD, Sroubek J, Tran ND, Hottinger AF, Landolfi J, Desai R, Caroli M, Kew Y, Honnorat J, Idbaih A, Kirson ED, Weinberg U, Palti Y, Hegi ME, Ram Z. Maintenance Therapy With Tumor-Treating Fields Plus Temozolomide vs Temozolomide Alone for Glioblastoma. *JAMA*. 2015;314(23):2535.
8. Zhang H, Wang R, Yu Y, Liu J, Luo T, Fan F. Glioblastoma Treatment Modalities besides Surgery. *Journal of Cancer*. 2019;10(20):4793-4806.
9. Hodges TR, Ott M, Xiu J, Gatalica Z, Swensen J, Zhou S, Huse JT, de Groot

- J, Li S, Overwijk WW, Spetzler D, Heimberger AB. Mutational burden, immune checkpoint expression, and mismatch repair in glioma: implications for immune checkpoint immunotherapy. *Neuro-Oncology*. 2017;19(8):1047-1057.
10. Villanueva-Meyer JE, Mabray MC, Cha S. Current Clinical Brain Tumor Imaging. *Neurosurgery*. 2017;81(3):397-415.
 11. Bernstein MA, King KF, Zhou XJ. *Handbook of MRI Pulse Sequences*. Elsevier; 2004.
 12. Keunen O, Taxt T, Grüner R, Lund-Johansen M, Tonn J-C, Pavlin T, Bjerkvig R, Niclou SP, Thorsen F. Multimodal imaging of gliomas in the context of evolving cellular and molecular therapies. *Advanced Drug Delivery Reviews*. 2014;76(1):98-115.
 13. Chaddad A, Kucharczyk MJ, Daniel P, Sabri S, Jean-Claude BJ, Niazi T, Abdulkarim B. Radiomics in Glioblastoma: Current Status and Challenges Facing Clinical Implementation. *Frontiers in Oncology*. 2019;9.
 14. Elshafeey N, Kotrotsou A, Hassan A, Elshafei N, Hassan I, Ahmed S, Abrol S, Agarwal A, El Salek K, Bergamaschi S, Acharya J, Moron FE, Law M, Fuller GN, Huse JT, Zinn PO, Colen RR. Multicenter study demonstrates radiomic features derived from magnetic resonance perfusion images identify pseudoprogression in glioblastoma. *Nature Communications*. 2019;10(1):3170.
 15. Momcilovic M, Shackelford DB. Imaging Cancer Metabolism. *Biomolecules & Therapeutics*. 2018;26(1):81-92.

16. Penet M-F, Mikhaylova M, Li C, Krishnamachary B, Glunde K, Pathak AP, Bhujwala ZM. Applications of molecular MRI and optical imaging in cancer. *Future Medicinal Chemistry*. 2010;2(6):975-988.
17. Gurcan MN, Boucheron LE, Can A, Madabhushi A, Rajpoot NM, Yener B. Histopathological Image Analysis: A Review. *IEEE Reviews in Biomedical Engineering*. 2009;2:147-171.
18. Dang X, Bardhan NM, Qi J, Gu L, Eze NA, Lin C-W, Kataria S, Hammond PT, Belcher AM. Deep-tissue optical imaging of near cellular-sized features. *Scientific Reports*. 2019;9(1):3873.
19. Wang C, Wang Z, Zhao T, Li Y, Huang G, Sumer BD, Gao J. Optical molecular imaging for tumor detection and image-guided surgery. *Biomaterials*. 2018;157:62-75.
20. Stummer W, Pichlmeier U, Meinel T, Wiestler OD, Zanella F, Reulen H-J. Fluorescence-guided surgery with 5-aminolevulinic acid for resection of malignant glioma: a randomised controlled multicentre phase III trial. *The Lancet Oncology*. 2006;7(5):392-401.
21. Hoh CK. Clinical use of FDG PET. *Nuclear Medicine and Biology*. 2007;34(7):737-742.
22. Fletcher JW, Djulbegovic B, Soares HP, Siegel BA, Lowe VJ, Lyman GH, Coleman RE, Wahl R, Paschold JC, Avril N, Einhorn LH, Suh WW, Samson D, Delbeke D, Gorman M, Shields AF. Recommendations on the Use of 18F-FDG PET in Oncology. *Journal of Nuclear Medicine*. 2008;49(3):480-508.

23. Zhu A, Lee D, Shim H. Metabolic Positron Emission Tomography Imaging in Cancer Detection and Therapy Response. *Seminars in Oncology*. 2011;38(1):55-69.
24. Thiele F, Ehmer J, Piroth MD, Eble MJ, Coenen HH, Kaiser H-J, Schaefer WM, Buell U, Boy C. The quantification of dynamic FET PET imaging and correlation with the clinical outcome in patients with glioblastoma. *Physics in Medicine and Biology*. 2009;54(18):5525-5539.
25. Pöppel G, Kreth FW, Herms J, Koch W, Mehrkens JH, Gildehaus FJ, Kretzschmar HA, Tonn JC, Tatsch K. Analysis of 18F-FET PET for grading of recurrent gliomas: is evaluation of uptake kinetics superior to standard methods? *Journal of Nuclear Medicine*. 2006;47(3):393-403.
26. Tripathi M, Sharma R, D'Souza M, Jaimini A, Panwar P, Varshney R, Datta A, Kumar N, Garg G, Singh D, Grover RK, Mishra AK, Mondal A. Comparative Evaluation of F-18 FDOPA, F-18 FDG, and F-18 FLT-PET/CT for Metabolic Imaging of Low Grade Gliomas. *Clinical Nuclear Medicine*. 2009;34(12):878-883.
27. Chen W, Silverman DHS, Delaloye S, Czernin J, Kamdar N, Pope W, Satyamurthy N, Schiepers C, Cloughesy T. 18F-FDOPA PET imaging of brain tumors: comparison study with 18F-FDG PET and evaluation of diagnostic accuracy. *Journal of Nuclear Medicine*. 2006;47(6):904-911.
28. Glatstein E. Comparison of 11C-choline PET and FDG PET for the Differential Diagnosis of Malignant Tumors. *Yearbook of Oncology*. 2006;2006:33-36.

29. Hara T, Kosaka N, Shinoura N, Kondo T. PET imaging of brain tumor with [methyl-11C]choline. *Journal of Nuclear Medicine*. 1997;38(6):842-847.
30. DeBerardinis RJ, Thompson CB. Cellular Metabolism and Disease: What Do Metabolic Outliers Teach Us? *Cell*. 2012;148(6):1132-1144.
31. Hanahan D, Weinberg RA. The Hallmarks of Cancer. *Cell*. 2000;100:57-70.
32. Yan H, Parsons DW, Jin G, McLendon R, Rasheed BA, Yuan W, Kos I, Batinic-Haberle I, Jones S, Riggins GJ, Friedman H, Friedman A, Reardon D, Herndon J, Kinzler KW, Velculescu VE, Vogelstein B, Bigner DD. IDH1 and IDH2 Mutations in Gliomas. *New England Journal of Medicine*. 2009;360(8):765-773.
33. Hu J, Salzillo TC, Sailasuta N, Lang FF, Bhattacharya P. Interrogating IDH Mutation in Brain Tumor: Magnetic Resonance and Hyperpolarization. *Topics in magnetic resonance imaging : TMRI*. 2017;26(1):27-32.
34. Coller HA. Is Cancer a Metabolic Disease? *The American Journal of Pathology*. 2014;184(1):4-17.
35. Martinez-Outschoorn UE, Peiris-Pagés M, Pestell RG, Sotgia F, Lisanti MP. Cancer metabolism: a therapeutic perspective. *Nature Reviews Clinical Oncology*. 2017;14(1):11-31.
36. Vander Heiden MG, Cantley LC, Thompson CB. Understanding the Warburg Effect: The Metabolic Requirements of Cell Proliferation. *Science*. 2009;324(5930):1029-1033.

37. Warburg O. On the Origin of Cancer Cells. *Science*. 1956;123(3191):309-314.
38. de Graaf RA. *In Vivo NMR Spectroscopy*. John Wiley & Sons, Ltd; 2007.
39. Zhu H, Barker PB. MR Spectroscopy and Spectroscopic Imaging of the Brain. In: *Methods in Molecular Biology*. ; 2011:203-226.
40. Glunde K, Bhujwala ZM, Ronen SM. Choline metabolism in malignant transformation. *Nature Reviews Cancer*. 2011;11(12):835-848.
41. Zoula S, Hérigault G, Ziegler A, Farion R, Décorps M, Rémy C. Correlation between the occurrence of 1 H-MRS lipid signal, necrosis and lipid droplets during C6 rat glioma development. *NMR in Biomedicine*. 2003;16(4):199-212.
42. Rémy C, Arús C, Ziegler A, Lai ES, Moreno A, Fur Y Le, Décorps M. In Vivo, Ex Vivo, and In Vitro One- and Two-Dimensional Nuclear Magnetic Resonance Spectroscopy of an Intracerebral Glioma in Rat Brain: Assignment of Resonances. *Journal of Neurochemistry*. 2008;62(1):166-179.
43. DeBerardinis RJ, Mancuso A, Daikhin E, Nissim I, Yudkoff M, Wehrli S, Thompson CB. Beyond aerobic glycolysis: Transformed cells can engage in glutamine metabolism that exceeds the requirement for protein and nucleotide synthesis. *Proceedings of the National Academy of Sciences*. 2007;104(49):19345-19350.
44. Dang L, White DW, Gross S, Bennett BD, Bittinger MA, Driggers EM, Fantin VR, Jang HG, Jin S, Keenan MC, Marks KM, Prins RM, Ward PS, Yen KE, Liao LM, Rabinowitz JD, Cantley LC, Thompson CB, Vander Heiden MG, Su

- SM. Cancer-associated IDH1 mutations produce 2-hydroxyglutarate. *Nature*. 2009;462(7274):739-744.
45. Nelson SJ. Assessment of therapeutic response and treatment planning for brain tumors using metabolic and physiological MRI. *NMR in Biomedicine*. 2011;24(6):734-749.
46. Nelson SJ, Ozhinsky E, Li Y, Park IW, Crane J. Strategies for rapid in vivo ¹H and hyperpolarized ¹³C MR spectroscopic imaging. *Journal of Magnetic Resonance*. 2013;229:187-197.
47. Fulham MJ, Bizzi A, Dietz MJ, Shih HHL, Raman R, Sobering GS, Frank JA, Dwyer AJ, Alger JR, Di Chiro G. Mapping of brain tumor metabolites with proton MR spectroscopic imaging: clinical relevance. *Radiology*. 1992;185(3):675-686.
48. Negendank WG, Sauter R, Brown TR, Evelhoch JL, Falini A, Gotsis ED, Heerschap A, Kamada K, Lee BCP, Mengeot MM, Moser E, Padavic-Shaller KA, Sanders JA, Spraggins TA, Stillman AE, Terwey B, Vogl TJ, Wicklow K, Zimmerman RA. Proton magnetic resonance spectroscopy in patients with glial tumors: a multicenter study. *Journal of Neurosurgery*. 1996;84(3):449-458.
49. Dowling C, Bollen AW, Noworolski SM, McDermott MW, Barbaro NM, Day MR, Henry RG, Chang SM, Dillon WP, Nelson SJ, Vigneron DB. Preoperative proton MR spectroscopic imaging of brain tumors: correlation with histopathologic analysis of resection specimens. *American Journal of*

Neuroradiology. 2001;22(4):604-612.

50. Louis DN, Ohgaki H, Wiestler OD, Cavenee WK, Burger PC, Jouvet A, Scheithauer BW, Kleihues P. The 2007 WHO Classification of Tumours of the Central Nervous System. *Acta Neuropathologica*. 2007;114(2):97-109.
51. Di Costanzo A, Trojsi F, Giannatempo GM, Vuolo L, Popolizio T, Catapano D, Bonavita S, D'Angelo VA, Tedeschi G, Scarabino T. Spectroscopic, diffusion and perfusion magnetic resonance imaging at 3.0 Tesla in the delineation of glioblastomas: preliminary results. *Journal of experimental & clinical cancer research : CR*. 2006;25(3):383-390.
52. Di Costanzo A, Scarabino T, Trojsi F, Giannatempo GM, Popolizio T, Catapano D, Bonavita S, Maggialelli N, Tosetti M, Salvolini U, D'Angelo VA, Tedeschi G. Multiparametric 3T MR approach to the assessment of cerebral gliomas: tumor extent and malignancy. *Neuroradiology*. 2006;48(9):622-631.
53. Croteau D, Scarpace L, Hearshen D, Gutierrez J, Fisher JL, Rock JP, Mikkelsen T. Correlation between Magnetic Resonance Spectroscopy Imaging and Image-guided Biopsies: Semiquantitative and Qualitative Histopathological Analyses of Patients with Untreated Glioma. *Neurosurgery*. 2001;49(4):823-829.
54. Chang SM, Nelson S, Vandenberg S, Cha S, Prados M, Butowski N, McDermott M, Parsa AT, Aghi M, Clarke J, Berger M. Integration of preoperative anatomic and metabolic physiologic imaging of newly diagnosed glioma. *Journal of Neuro-Oncology*. 2009;92(3):401-415.

55. McKnight TR, Noworolski SM, Vigneron DB, Nelson DR, Nataraj SJ. An automated technique for the quantitative assessment of 3D-MRSI data from patients with glioma. *Journal of Magnetic Resonance Imaging*. 2001;13(2):167-177.
56. Caivano R, Lotumolo A, Rabasco P, Zandolino A, D'Antuono F, Villonio A, Lancellotti MI, Macarini L, Cammarota A. 3 Tesla magnetic resonance spectroscopy: cerebral gliomas vs. metastatic brain tumors. Our experience and review of the literature. *International Journal of Neuroscience*. 2013;123(8):537-543.
57. Venkatesh SK, Gupta RK, Pal L, Husain N, Husain M. Spectroscopic increase in choline signal is a nonspecific marker for differentiation of infective/inflammatory from neoplastic lesions of the brain. *Journal of Magnetic Resonance Imaging*. 2001;14(1):8-15.
58. Li X, Jin H, Lu Y, Oh J, Chang S, Nelson SJ. Identification of MRI and ¹H MRSI parameters that may predict survival for patients with malignant gliomas. *NMR in Biomedicine*. 2004;17(1):10-20.
59. Hattingen E, Delic O, Franz K, Pilatus U, Raab P, Lanfermann H, Gerlach R. ¹H MRSI and progression-free survival in patients with WHO grades II and III gliomas. *Neurological Research*. 2010;32(6):593-602.
60. Chan AA, Lau A, Pirzkall A, Chang SM, Verhey LJ, Larson D, McDermott MW, Dillon WP, Nelson SJ. Proton magnetic resonance spectroscopy imaging in the evaluation of patients undergoing gamma knife surgery for Grade IV

- glioma. *Journal of Neurosurgery*. 2004;101(3):467-475.
61. Alexander A, Murtha A, Abdulkarim B, Mehta V, Wheatley M, Murray B, Riauka T, Hanson J, Fulton D, McEwan A, Roa W. Prognostic significance of serial magnetic resonance spectroscopies over the course of radiation therapy for patients with malignant glioma. *Clinical and investigative medicine Medecine clinique et experimentale*. 2006;29(5):301-311.
 62. Zeeman P. XXXII. On the influence of magnetism on the nature of the light emitted by a substance. *The London, Edinburgh, and Dublin Philosophical Magazine and Journal of Science*. 1897;43(262):226-239.
 63. Brown RW, Cheng YCN, Haacke EM, Thompson MR, Venkatesan R. *Magnetic Resonance Imaging*. (Brown RW, Cheng Y-CN, Haacke EM, Thompson MR, Venkatesan R, eds.). John Wiley & Sons Ltd; 2014.
 64. Ernst T, Kreis R, Ross BD. Absolute Quantitation of Water and Metabolites in the Human Brain. I. Compartments and Water. *Journal of Magnetic Resonance, Series B*. 1993;102(1):1-8.
 65. Kim I-Y, Suh S-H, Lee I-K, Wolfe RR. Applications of stable, nonradioactive isotope tracers in in vivo human metabolic research. *Experimental & Molecular Medicine*. 2016;48(1):e203-e203.
 66. Jang C, Chen L, Rabinowitz JD. Metabolomics and Isotope Tracing. *Cell*. 2018;173(4):822-837.
 67. Buescher JM, Antoniewicz MR, Boros LG, Burgess SC, Brunengraber H, Clish

- CB, DeBerardinis RJ, Feron O, Frezza C, Ghesquiere B, Gottlieb E, Hiller K, Jones RG, Kamphorst JJ, Kibbey RG, Kimmelman AC, Locasale JW, Lunt SY, Maddocks ODK, Malloy C, Metallo CM, Meuillet EJ, Munger J, Nöh K, Rabinowitz JD, Ralser M, Sauer U, Stephanopoulos G, St-Pierre J, Tennant DA, Wittmann C, Vander Heiden MG, Vazquez A, Vousden K, Young JD, Zamboni N, Fendt S-M. A roadmap for interpreting ^{13}C metabolite labeling patterns from cells. *Current Opinion in Biotechnology*. 2015;34:189-201.
68. Frossati G. Polarization of ^3He , D_2 and (eventually) ^{129}Xe Using Low Temperatures and High Magnetic Fields. *Journal of Low Temperature Physics*. 1998;111:521-532.
 69. Hirsch ML, Kalechofsky N, Belzer A, Rosay M, Kempf JG. Brute-Force Hyperpolarization for NMR and MRI. *Journal of the American Chemical Society*. 2015;137(26):8428-8434.
 70. Eisenschmid TC, Kirss RU, Deutsch PP, Hommeltoft SI, Eisenberg R, Bargon J, Lawler RG, Balch AL. Para hydrogen induced polarization in hydrogenation reactions. *Journal of the American Chemical Society*. 1987;109(26):8089-8091.
 71. Bhattacharya P, Chekmenev EY, Reynolds WF, Wagner S, Zacharias N, Chan HR, Bünger R, Ross BD. Parahydrogen-induced polarization (PHIP) hyperpolarized MR receptor imaging in vivo: a pilot study of ^{13}C imaging of atheroma in mice. *NMR in Biomedicine*. 2011;24(8):1023-1028.
 72. Zhou X, Graziani D, Pines A. Hyperpolarized xenon NMR and MRI signal

- amplification by gas extraction. *Proceedings of the National Academy of Sciences*. 2009;106(40):16903-16906.
73. Walker TG, Happer W. Spin-exchange optical pumping of noble-gas nuclei. *Reviews of Modern Physics*. 1997;69(2):629-642.
 74. Abragam A, Goldman M. Principles of dynamic nuclear polarisation. *Reports on Progress in Physics*. 1978;41(3):395-467.
 75. Dutta P, Martinez G V., Gillies RJ. A new horizon of DNP technology: application to in-vivo ¹³C magnetic resonance spectroscopy and imaging. *Biophysical Reviews*. 2013;5(3):271-281.
 76. Overhauser AW. Polarization of Nuclei in Metals. *Physical Review*. 1953;92(2):411-415.
 77. Carver TR, Slichter CP. Polarization of Nuclear Spins in Metals. *Physical Review*. 1953;92(1):212-213.
 78. Ardenkjaer-Larsen JH, Fridlund B, Gram A, Hansson G, Hansson L, Lerche MH, Servin R, Thaning M, Golman K. Increase in signal-to-noise ratio of > 10,000 times in liquid-state NMR. *Proceedings of the National Academy of Sciences*. 2003;100(18):10158-10163.
 79. Wang ZJ, Ohliger MA, Larson PEZ, Gordon JW, Bok RA, Slater J, Villanueva-Meyer JE, Hess CP, Kurhanewicz J, Vigneron DB. Hyperpolarized ¹³C MRI: State of the Art and Future Directions. *Radiology*. 2019;291(2):273-284.
 80. Gordon JW, Larson PEZ. Pulse Sequences for Hyperpolarized MRS. In:

EMagRes. John Wiley & Sons, Ltd; 2016:1229-1246.

81. Larson PEZ, Kerr AB, Chen AP, Lustig MS, Zierhut ML, Hu S, Cunningham CH, Pauly JM, Kurhanewicz J, Vigneron DB. Multiband excitation pulses for hyperpolarized ¹³C dynamic chemical-shift imaging. *Journal of Magnetic Resonance*. 2008;194(1):121-127.
82. Topping GJ, Hundshammer C, Nagel L, Grashei M, Aigner M, Skinner JG, Schulte RF, Schilling F. Acquisition strategies for spatially resolved magnetic resonance detection of hyperpolarized nuclei. *Magnetic Resonance Materials in Physics, Biology and Medicine*. 2020;33(2):221-256.
83. Hill DK, Orton MR, Mariotti E, Boulton JKR, Panek R, Jafar M, Parkes HG, Jamin Y, Miniotis MF, Al-Saffar NMS, Belouche-Babari M, Robinson SP, Leach MO, Chung Y-L, Eykyn TR. Model Free Approach to Kinetic Analysis of Real-Time Hyperpolarized ¹³C Magnetic Resonance Spectroscopy Data. Bathen TF, ed. *PLoS ONE*. 2013;8(9):e71996.
84. Daniels CJ, McLean MA, Schulte RF, Robb FJ, Gill AB, McGlashan N, Graves MJ, Schwaiger M, Lomas DJ, Brindle KM, Gallagher FA. A comparison of quantitative methods for clinical imaging with hyperpolarized ¹³C-pyruvate. *NMR in Biomedicine*. 2016;29(4):387-399.
85. Larson PEZ, Chen H-Y, Gordon JW, Korn N, Maidens J, Arcak M, Tang S, Criekinge M, Carvajal L, Mammoli D, Bok R, Aggarwal R, Ferrone M, Slater JB, Nelson SJ, Kurhanewicz J, Vigneron DB. Investigation of analysis methods for hyperpolarized ¹³C-pyruvate metabolic MRI in prostate cancer

patients. *NMR in Biomedicine*. 2018;31(11):e3997.

86. Kurhanewicz J, Vigneron DB, Brindle K, Chekmenev EY, Comment A, Cunningham CH, DeBerardinis RJ, Green GG, Leach MO, Rajan SS, Rizi RR, Ross BD, Warren WS, Malloy CR. Analysis of Cancer Metabolism by Imaging Hyperpolarized Nuclei: Prospects for Translation to Clinical Research. *Neoplasia*. 2011;13(2):81-97.
87. Salamanca-Cardona L, Keshari KR. ¹³C-labeled biochemical probes for the study of cancer metabolism with dynamic nuclear polarization-enhanced magnetic resonance imaging. *Cancer & Metabolism*. 2015;3(1):9.
88. Kurhanewicz J, Vigneron DB, Ardenkjaer-Larsen JH, Bankson JA, Brindle K, Cunningham CH, Gallagher FA, Keshari KR, Kjaer A, Laustsen C, Mankoff DA, Merritt ME, Nelson SJ, Pauly JM, Lee P, Ronen S, Tyler DJ, Rajan SS, Spielman DM, Wald L, Zhang X, Malloy CR, Rizi R. Hyperpolarized ¹³C MRI: Path to Clinical Translation in Oncology. *Neoplasia*. 2019;21(1):1-16.
89. Dutta P, Salzillo TC, Pudakalakatti S, Gammon ST, Kaiparettu BA, McAllister F, Wagner S, Frigo DE, Logothetis CJ, Zacharias NM, Bhattacharya PK. Assessing Therapeutic Efficacy in Real-time by Hyperpolarized Magnetic Resonance Metabolic Imaging. *Cells*. 2019;8(4):340.
90. Brindle K. Watching tumours gasp and die with MRI: the promise of hyperpolarised ¹³C MR spectroscopic imaging. *The British Journal of Radiology*. 2012;85(1014):697-708.
91. Chaumeil MM, Radoul M, Najac C, Eriksson P, Viswanath P, Blough MD,

- Chesnelong C, Luchman HA, Cairncross JG, Ronen SM. Hyperpolarized ^{13}C MR imaging detects no lactate production in mutant IDH1 gliomas: Implications for diagnosis and response monitoring. *NeuroImage: Clinical*. 2016;12:180-189.
92. Park JM, Josan S, Jang T, Merchant M, Yen Y-F, Hurd RE, Recht L, Spielman DM, Mayer D. Metabolite kinetics in C6 rat glioma model using magnetic resonance spectroscopic imaging of hyperpolarized $[1-^{13}\text{C}]$ pyruvate. *Magnetic Resonance in Medicine*. 2012;68(6):1886-1893.
 93. Park JM, Josan S, Jang T, Merchant M, Watkins R, Hurd RE, Recht LD, Mayer D, Spielman DM. Volumetric spiral chemical shift imaging of hyperpolarized $[2-^{13}\text{C}]$ pyruvate in a rat c6 glioma model. *Magnetic Resonance in Medicine*. 2016;75(3):973-984.
 94. Autry AW, Hashizume R, James CD, Larson PEZ, Vigneron DB, Park I. Measuring Tumor Metabolism in Pediatric Diffuse Intrinsic Pontine Glioma Using Hyperpolarized Carbon-13 MR Metabolic Imaging. *Contrast Media & Molecular Imaging*. 2018;2018:1-6.
 95. Mair R, Wright AJ, Ros S, Hu D, Booth T, Kreis F, Rao J, Watts C, Brindle KM. Metabolic Imaging Detects Low Levels of Glycolytic Activity That Vary with Levels of c-Myc Expression in Patient-Derived Xenograft Models of Glioblastoma. *Cancer Research*. 2018;78(18):5408-5418.
 96. Day SE, Kettunen MI, Cherukuri MK, Mitchell JB, Lizak MJ, Morris HD, Matsumoto S, Koretsky AP, Brindle KM. Detecting response of rat C6 glioma

- tumors to radiotherapy using hyperpolarized [1-¹³C]pyruvate and ¹³C magnetic resonance spectroscopic imaging. *Magnetic Resonance in Medicine*. 2011;65(2):557-563.
97. Park I, Bok R, Ozawa T, Phillips JJ, James CD, Vigneron DB, Ronen SM, Nelson SJ. Detection of early response to temozolomide treatment in brain tumors using hyperpolarized ¹³C MR metabolic imaging. *Journal of Magnetic Resonance Imaging*. 2011;33(6):1284-1290.
 98. Datta K, Lauritzen MH, Merchant M, Jang T, Liu S-C, Hurd R, Recht L, Spielman DM. Reversed metabolic reprogramming as a measure of cancer treatment efficacy in rat C6 glioma model. Dadachova E, ed. *PLOS ONE*. 2019;14(12):e0225313.
 99. Michel KA, Zieliński R, Walker CM, Le Roux L, Priebe W, Bankson JA, Schellingerhout D. Hyperpolarized Pyruvate MR Spectroscopy Depicts Glycolytic Inhibition in a Mouse Model of Glioma. *Radiology*. 2019;293(1):168-173.
 100. Lee CY, Soliman H, Geraghty BJ, Chen AP, Connelly KA, Endre R, Perks WJ, Heyn C, Black SE, Cunningham CH. Lactate topography of the human brain using hyperpolarized ¹³C-MRI. *NeuroImage*. 2020;204:116202.
 101. Grist JT, McLean MA, Riemer F, Schulte RF, Deen SS, Zaccagna F, Woitek R, Daniels CJ, Kaggie JD, Matys T, Patterson I, Slough R, Gill AB, Chhabra A, Eichenberger R, Laurent M-C, Comment A, Gillard JH, Coles AJ, Tyler DJ, Wilkinson I, Basu B, Lomas DJ, Graves MJ, Brindle KM, Gallagher FA.

- Quantifying normal human brain metabolism using hyperpolarized [1–¹³C]pyruvate and magnetic resonance imaging. *NeuroImage*. 2019;189:171-179.
102. Chung BT, Chen H-Y, Gordon J, Mammoli D, Sriram R, Autry AW, Le Page LM, Chaumeil MM, Shin P, Slater J, Tan CT, Suszczynski C, Chang S, Li Y, Bok RA, Ronen SM, Larson PEZ, Kurhanewicz J, Vigneron DB. First hyperpolarized [2-¹³C]pyruvate MR studies of human brain metabolism. *Journal of Magnetic Resonance*. 2019;309:106617.
 103. Miloushev VZ, Granlund KL, Boltyanskiy R, Lyashchenko SK, DeAngelis LM, Mellinghoff IK, Brennan CW, Tabar V, Yang TJ, Holodny AI, Sosa RE, Guo YW, Chen AP, Tropp J, Robb F, Keshari KR. Metabolic Imaging of the Human Brain with Hyperpolarized ¹³C Pyruvate Demonstrates ¹³C Lactate Production in Brain Tumor Patients. *Cancer Research*. 2018;78(14):3755-3760.
 104. Gordon JW, Chen H, Autry A, Park I, Van Criekinge M, Mammoli D, Milshteyn E, Bok R, Xu D, Li Y, Aggarwal R, Chang S, Slater JB, Ferrone M, Nelson S, Kurhanewicz J, Larson PEZ, Vigneron DB. Translation of Carbon-13 EPI for hyperpolarized MR molecular imaging of prostate and brain cancer patients. *Magnetic Resonance in Medicine*. 2019;81(4):2702-2709.
 105. Park I, Larson PEZ, Gordon JW, Carvajal L, Chen H-Y, Bok R, Van Criekinge M, Ferrone M, Slater JB, Xu D, Kurhanewicz J, Vigneron DB, Chang S, Nelson SJ. Development of methods and feasibility of using hyperpolarized carbon-13

- imaging data for evaluating brain metabolism in patient studies. *Magnetic Resonance in Medicine*. 2018;80(3):864-873.
106. Mammoli D, Carvajal L, Slater JB, Bok R, Crane J, Xu D, Chang S, Vigneron DB, Gordon J, Autry A, Larson PEZ, Li Y, Chen H-Y, Chung B, Shin P, Van Criekinge M. Kinetic Modeling of Hyperpolarized Carbon-13 Pyruvate Metabolism in the Human Brain. *IEEE Transactions on Medical Imaging*. 2020;39(2):320-327.
 107. Crane JC, Gordon JW, Chen H-Y, Autry AW, Li Y, Olson MP, Kurhanewicz J, Vigneron DB, Larson PEZ, Xu D. Hyperpolarized ¹³C MRI data acquisition and analysis in prostate and brain at University of California, San Francisco. *NMR in Biomedicine*. Published online March 19, 2020:e4280.
 108. Mansouri S, Singh S, Alamsahebpour A, Burrell K, Li M, Karabork M, Ekinci C, Koch E, Solaroglu I, Chang JT, Wouters B, Aldape K, Zadeh G. DICER governs characteristics of glioma stem cells and the resulting tumors in xenograft mouse models of glioblastoma. *Oncotarget*. 2016;7(35):56431-56446.
 109. Singh SK, Hawkins C, Clarke ID, Squire JA, Bayani J, Hide T, Henkelman RM, Cusimano MD, Dirks PB. Identification of human brain tumour initiating cells. *Nature*. 2004;432(7015):396-401.
 110. Wei J, Barr J, Kong L-Y, Wang Y, Wu A, Sharma AK, Gumin J, Henry V, Colman H, Priebe W, Sawaya R, Lang FF, Heimberger AB. Glioblastoma Cancer-Initiating Cells Inhibit T-Cell Proliferation and Effector Responses by

- the Signal Transducers and Activators of Transcription 3 Pathway. *Molecular Cancer Therapeutics*. 2010;9(1):67-78.
111. Lal S, Lacroix M, Tofilon P, Fuller GN, Sawaya R, Lang FF. An implantable guide-screw system for brain tumor studies in small animals. *Journal of Neurosurgery*. 2000;92(2):326-333.
 112. Fedorov A, Beichel R, Kalpathy-Cramer J, Finet J, Fillion-Robin J-C, Pujol S, Bauer C, Jennings D, Fennessy F, Sonka M, Buatti J, Aylward S, Miller J V., Pieper S, Kikinis R. 3D Slicer as an image computing platform for the Quantitative Imaging Network. *Magnetic Resonance Imaging*. 2012;30(9):1323-1341.
 113. Weygand J, Carter SE, Salzillo TC, Moussalli M, Dai B, Dutta P, Zuo X, Fleming JB, Shureiqi I, Bhattacharya P. Can an Organoid Recapitulate the Metabolome of its Parent Tissue? A Pilot NMR Spectroscopy Study. *Journal of Cancer Prevention & Current Research*. 2017;8(7):00307.
 114. Zacharias NM, McCullough C, Shanmugavelandy S, Lee J, Lee Y, Dutta P, McHenry J, Nguyen L, Norton W, Jones LW, Bhattacharya PK. Metabolic Differences in Glutamine Utilization Lead to Metabolic Vulnerabilities in Prostate Cancer. *Scientific Reports*. 2017;7(1):16159.
 115. Schindelin J, Arganda-Carreras I, Frise E, Kaynig V, Longair M, Pietzsch T, Preibisch S, Rueden C, Saalfeld S, Schmid B, Tinevez J-Y, White DJ, Hartenstein V, Eliceiri K, Tomancak P, Cardona A. Fiji: an open-source platform for biological-image analysis. *Nature Methods*. 2012;9(7):676-682.

116. Ruifrok AC, Johnston DA. Quantification of histochemical staining by color deconvolution. *Analytical and quantitative cytology and histology*. 2001;23(4):291-299.
117. Fisher R, Pusztai L, Swanton C. Cancer heterogeneity: implications for targeted therapeutics. *British Journal of Cancer*. 2013;108(3):479-485.
118. Meacham CE, Morrison SJ. Tumour heterogeneity and cancer cell plasticity. *Nature*. 2013;501(7467):328-337.
119. Brennan CW, Verhaak RGW, Mckenna A, Campos B, Noushmehr H, Salama SR, Zheng S, Chakravarty D, Sanborn JZ, Berman SH, Beroukhir R, Bernard B, Wu C-J, Genovese G, Shmulevich I, Barnholtz-Sloan J, Zou L, Vegesna R, Shukla SA, Ciriello G, Yung WK, Zhang W, Sougnez C, Mikkelsen T, Weisenberger DJ, Penny R, Kucherlapati R, Perou CM, Hayes DN, Gibbs R, Marra M, Mills GB, Lander E, Spellman P, Wilson R, Sander C, Weinstein J, Meyerson M, Gabriel S, Laird PW, Haussler D, Getz G, Chin L, Network TR. The Somatic Genomic Landscape of Glioblastoma. *Cell*. 2013;155(155):462-477.
120. McLendon R, Friedman A, Bigner D, Van Meir EG, Brat DJ, M. Mastrogiannis G, Olson JJ, Mikkelsen T, Thomson E, et al. Comprehensive genomic characterization defines human glioblastoma genes and core pathways. *Nature*. 2008;455(7216):1061-1068.
121. Wangaryattawanich P, Hatami M, Wang J, Thomas G, Flanders A, Kirby J, Wintermark M, Huang ES, Bakhtiari AS, Luedi MM, Hashmi SS, Rubin DL,

- Chen JY, Hwang SN, Freymann J, Holder CA, Zinn PO, Colen RR. Multicenter imaging outcomes study of The Cancer Genome Atlas glioblastoma patient cohort: imaging predictors of overall and progression-free survival. *Neuro-Oncology*. 2015;17(11):1525-1537.
122. Dutta P, Perez MR, Lee J, Kang Y, Pratt M, Salzillo TC, Weygand J, Zacharias NM, Gammon ST, Koay EJ, Kim M, McAllister F, Sen S, Maitra A, Piwnica-Worms D, Fleming JB, Bhattacharya PK. Combining Hyperpolarized Real-Time Metabolic Imaging and NMR Spectroscopy To Identify Metabolic Biomarkers in Pancreatic Cancer. *Journal of Proteome Research*. 2019;18(7):2826-2834.
 123. Seyfried TN, Kiebish MA, Marsh J, Shelton LM, Huysentruyt LC, Mukherjee P. Metabolic management of brain cancer. *Biochimica et Biophysica Acta (BBA) - Bioenergetics*. 2011;1807(6):577-594.
 124. Libby CJ, Tran AN, Scott SE, Griguer C, Hjelmeland AB. The pro-tumorigenic effects of metabolic alterations in glioblastoma including brain tumor initiating cells. *Biochimica et Biophysica Acta (BBA) - Reviews on Cancer*. 2018;1869(2):175-188.
 125. Robertson-Tessi M, Gillies RJ, Gatenby RA, Anderson ARA. Impact of Metabolic Heterogeneity on Tumor Growth, Invasion, and Treatment Outcomes. *Cancer Research*. 2015;75(8):1567-1579.
 126. van Linde ME, Brahm CG, de Witt Hamer PC, Reijneveld JC, Bruynzeel AME, Vandertop WP, van de Ven PM, Wagemakers M, van der Weide HL, Enting

RH, Walenkamp AME, Verheul HMW. Treatment outcome of patients with recurrent glioblastoma multiforme: a retrospective multicenter analysis.

Journal of Neuro-Oncology. Published online 2017.

127. Zhao Y-H, Wang Z-F, Pan Z-Y, Péus D, Delgado-Fernandez J, Pallud J, Li Z-Q. A Meta-Analysis of Survival Outcomes Following Reoperation in Recurrent Glioblastoma: Time to Consider the Timing of Reoperation. *Frontiers in Neurology*. Published online 2019.
128. Ghosh D, Ulasov I V., Chen L, Harkins LE, Wallenborg K, Hothi P, Rostad S, Hood L, Cobbs CS. TGF β -Responsive HMOX1 Expression Is Associated with Stemness and Invasion in Glioblastoma Multiforme. *STEM CELLS*. 2016;34(9):2276-2289.
129. Park SJ, Smith CP, Wilbur RR, Cain CP, Kallu SR, Valasapalli S, Sahoo A, Guda MR, Tsung AJ, Velpula KK. An overview of MCT1 and MCT4 in GBM: small molecule transporters with large implications. *American journal of cancer research*. 2018;8(10):1967-1976.
130. Viswanath P, Najac C, Izquierdo JL, Pankov A, Hong C, Eriksson P, Costello JF, Pieper RO, Ronen SM. Mutant IDH1 expression is associated with down-regulation of monocarboxylate transporters. *Oncotarget*. 2016;7(23):34942-34955.
131. Parsons DW, Jones S, Zhang X, Lin JC-H, Leary RJ, Angenendt P, Mankoo P, Carter H, Siu I-M, Gallia GL, Olivi A, McLendon R, Rasheed BA, Keir S, Nikolskaya T, Nikolsky Y, Busam DA, Tekleab H, Diaz LA, Hartigan J, Smith

- DR, Strausberg RL, Marie SKN, Shinjo SMO, Yan H, Riggins GJ, Bigner DD, Karchin R, Papadopoulos N, Parmigiani G, Vogelstein B, Velculescu VE, Kinzler KW. An Integrated Genomic Analysis of Human Glioblastoma Multiforme. *Science*. 2008;321(5897):1807-1812.
132. Froberg MK, Gerhart DZ, Enerson BE, Manivel C, Guzman-Paz M, Seacotte N, Drewes LR. Expression of monocarboxylate transporter MCT1 in normal and neoplastic human CNS tissues. *Neuroreport*. 2001;12(4):761-765.
 133. Miranda-Gonçalves V, Honavar M, Pinheiro C, Martinho O, Pires MM, Pinheiro C, Cordeiro M, Bebiano G, Costa P, Palmeirim I, Reis RM, Baltazar F. Monocarboxylate transporters (MCTs) in gliomas: expression and exploitation as therapeutic targets. *Neuro-Oncology*. 2013;15(2):172-188.
 134. Colen CB, Shen Y, Ghoddoussi F, Yu P, Francis TB, Koch BJ, Monterey MD, Galloway MP, Sloan AE, Mathupala SP. Metabolic Targeting of Lactate Efflux by Malignant Glioma Inhibits Invasiveness and Induces Necrosis: An In Vivo Study. *Neoplasia*. 2011;13(7):620-632.
 135. Granlund KL, Tee S-S, Vargas HA, Lyashchenko SK, Reznik E, Fine S, Laudone V, Eastham JA, Touijer KA, Reuter VE, Gonen M, Sosa RE, Nicholson D, Guo YW, Chen AP, Tropp J, Robb F, Hricak H, Keshari KR. Hyperpolarized MRI of Human Prostate Cancer Reveals Increased Lactate with Tumor Grade Driven by Monocarboxylate Transporter 1. *Cell Metabolism*. 2020;31(1):105-114.e3.
 136. Gallagher FA, Woitek R, McLean MA, Gill AB, Manzano Garcia R, Provenzano

- E, Riemer F, Kaggie J, Chhabra A, Ursprung S, Grist JT, Daniels CJ, Zaccagna F, Laurent M-C, Locke M, Hilborne S, Frary A, Torheim T, Boursnell C, Schiller A, Patterson I, Slough R, Carmo B, Kane J, Biggs H, Harrison E, Deen SS, Patterson A, Lanz T, Kingsbury Z, Ross M, Basu B, Baird R, Lomas DJ, Sala E, Wason J, Rueda OM, Chin S-F, Wilkinson IB, Graves MJ, Abraham JE, Gilbert FJ, Caldas C, Brindle KM. Imaging breast cancer using hyperpolarized carbon-13 MRI. *Proceedings of the National Academy of Sciences*. 2020;117(4):2092-2098.
137. Taal W, Brandsma D, de Bruin HG, Bromberg JE, Swaak-Kragten AT, Sillevius Smitt PAE, van Es CA, van den Bent MJ. Incidence of early pseudo-progression in a cohort of malignant glioma patients treated with chemoradiation with temozolomide. *Cancer*. 2008;113(2):405-410.
138. Shin PJ, Zhu Z, Camarda R, Bok RA, Zhou AY, Kurhanewicz J, Goga A, Vigneron DB. Cancer recurrence monitoring using hyperpolarized [1-13C]pyruvate metabolic imaging in murine breast cancer model. *Magnetic Resonance Imaging*. 2017;43:105-109.
139. Hu B, Wang Q, Wang YA, Hua S, Sauvé C-EG, Ong D, Lan ZD, Chang Q, Ho YW, Monasterio MM, Lu X, Zhong Y, Zhang J, Deng P, Tan Z, Wang G, Liao W-T, Corley LJ, Yan H, Zhang J, You Y, Liu N, Cai L, Finocchiaro G, Phillips JJ, Berger MS, Spring DJ, Hu J, Sulman EP, Fuller GN, Chin L, Verhaak RGW, DePinho RA. Epigenetic Activation of WNT5A Drives Glioblastoma Stem Cell Differentiation and Invasive Growth. *Cell*. 2016;167(5):1281-1295.e18.

140. Rao Y, Gammon S, Zacharias NM, Liu T, Salzillo T, Xi Y, Wang J, Bhattacharya P, Piwnica-Worms D. Hyperpolarized [1-¹³C]Pyruvate-to-[1-¹³C]Lactate Conversion is Rate Limited by Monocarboxylate Transporter-1 in the Plasma Membrane. *Proceedings of the National Academy of Sciences*. 2020;In Press.
141. Bianchi L, De Micheli E, Bricolo A, Ballini C, Fattori M, Venturi C, Pedata F, Tipton KF, Corte L Della. Extracellular Levels of Amino Acids and Choline in Human High Grade Gliomas: An Intraoperative Microdialysis Study. *Neurochemical Research*. 2004;29(1):325-334.
142. Ananieva EA, Wilkinson AC. Branched-chain amino acid metabolism in cancer. *Current Opinion in Clinical Nutrition and Metabolic Care*. 2018;21(1):64-70.
143. Tönjes M, Barbus S, Park YJ, Wang W, Schlotter M, Lindroth AM, Pleier S V., Bai AHC, Karra D, Piro RM, Felsberg J, Addington A, Lemke D, Weibrecht I, Hovestadt V, Rolli CG, Campos B, Turcan S, Sturm D, Witt H, Chan TA, Herold-Mende C, Kemkemer R, König R, Schmidt K, Hull W-E, Pfister SM, Jugold M, Hutson SM, Plass C, Okun JG, Reifenberger G, Lichter P, Radlwimmer B. BCAT1 promotes cell proliferation through amino acid catabolism in gliomas carrying wild-type IDH1. *Nature Medicine*. 2013;19(7):901-908.
144. Suh EH, Hackett EP, Wynn RM, Chuang DT, Zhang B, Luo W, Sherry AD, Park JM. In vivo assessment of increased oxidation of branched-chain amino

- acids in glioblastoma. *Scientific Reports*. 2019;9(1):340.
145. Serrao EM, Kettunen MI, Rodrigues TB, Dzien P, Wright AJ, Gopinathan A, Gallagher FA, Lewis DY, Frese KK, Almeida J, Howat WJ, Tuveson DA, Brindle KM. MRI with hyperpolarised [1-¹³C]pyruvate detects advanced pancreatic preneoplasia prior to invasive disease in a mouse model. *Gut*. 2016;65(3):465-475.
146. Dutta P, Castro Pando S, Mascaro M, Riquelme E, Zoltan M, Zacharias NM, Gammon ST, Piwnica-Worms D, Pagel MD, Sen S, Maitra A, Shams S, McAllister F, Bhattacharya PK. Early Detection of Pancreatic Intraepithelial Neoplasias (PanINs) in Transgenic Mouse Model by Hyperpolarized ¹³C Metabolic Magnetic Resonance Spectroscopy. *International Journal of Molecular Sciences*. 2020;21(10):3722.
147. Jalbert LE, Elkhaled A, Phillips JJ, Neill E, Williams A, Crane JC, Olson MP, Molinaro AM, Berger MS, Kurhanewicz J, Ronen SM, Chang SM, Nelson SJ. Metabolic Profiling of IDH Mutation and Malignant Progression in Infiltrating Glioma. *Scientific Reports*. 2017;7(1):44792.
148. Coloff JL, Murphy JP, Braun CR, Harris IS, Shelton LM, Kami K, Gygi SP, Selfors LM, Brugge JS. Differential Glutamate Metabolism in Proliferating and Quiescent Mammary Epithelial Cells. *Cell Metabolism*. 2016;23(5):867-880.
149. Cao Y, Lin S-H, Wang Y, Chin YE, Kang L, Mi J. Glutamic Pyruvate Transaminase GPT2 Promotes Tumorigenesis of Breast Cancer Cells by Activating Sonic Hedgehog Signaling. *Theranostics*. 2017;7(12):3021-3033.

150. Hao Y, Samuels Y, Li Q, Krokowski D, Guan B-J, Wang C, Jin Z, Dong B, Cao B, Feng X, Xiang M, Xu C, Fink S, Meropol NJ, Xu Y, Conlon RA, Markowitz S, Kinzler KW, Velculescu VE, Brunengraber H, Willis JE, LaFramboise T, Hatzoglou M, Zhang G-F, Vogelstein B, Wang Z. Oncogenic PIK3CA mutations reprogram glutamine metabolism in colorectal cancer. *Nature Communications*. 2016;7(1):11971.
151. Itkonen HM, Gorad SS, Duveau DY, Martin SES, Barkovskaya A, Bathen TF, Moestue SA, Mills IG. Inhibition of O-GlcNAc transferase activity reprograms prostate cancer cell metabolism. *Oncotarget*. 2016;7(11):12464-12476.
152. Parker SJ, Amendola CR, Hollinshead KER, Yu Q, Yamamoto K, Encarnación-Rosado J, Rose RE, LaRue MM, Sohn ASW, Biancur DE, Paulo JA, Gygi SP, Jones DR, Wang H, Philips MR, Bar-Sagi D, Mancias JD, Kimmelman AC. Selective Alanine Transporter Utilization Creates a Targetable Metabolic Niche in Pancreatic Cancer. *Cancer Discovery*. Published online April 27, 2020.
153. Ducker GS, Rabinowitz JD. One-Carbon Metabolism in Health and Disease. *Cell Metabolism*. 2017;25(1):27-42.
154. Nikiforov MA, Chandriani S, O'Connell B, Petrenko O, Kotenko I, Beavis A, Sedivy JM, Cole MD. A Functional Screen for Myc-Responsive Genes Reveals Serine Hydroxymethyltransferase, a Major Source of the One-Carbon Unit for Cell Metabolism. *Molecular and Cellular Biology*. 2002;22(16):5793-5800.

155. Tiwari V, Daoud E V, Hatanpaa KJ, Gao A, Zhang S, An Z, Ganji SK, Raisanen JM, Lewis CM, Askari P, Baxter J, Levy M, Dimitrov I, Thomas BP, Pinho MC, Madden CJ, Pan E, Patel TR, DeBerardinis RJ, Sherry AD, Mickey BE, Malloy CR, Maher EA, Choi C. Glycine by MR spectroscopy is an imaging biomarker of glioma aggressiveness. *Neuro-Oncology*. Published online February 14, 2020.
156. Zhang WC, Shyh-Chang N, Yang H, Rai A, Umashankar S, Ma S, Soh BS, Sun LL, Tai BC, Nga ME, Bhakoo KK, Jayapal SR, Nichane M, Yu Q, Ahmed DA, Tan C, Sing WP, Tam J, Thirugananam A, Noghabi MS, Huei Pang Y, Ang HS, Mitchell W, Robson P, Kaldis P, Soo RA, Swarup S, Lim EH, Lim B. Glycine Decarboxylase Activity Drives Non-Small Cell Lung Cancer Tumor-Initiating Cells and Tumorigenesis. *Cell*. 2012;148(1-2):259-272.
157. Jain M, Nilsson R, Sharma S, Madhusudhan N, Kitami T, Souza AL, Kafri R, Kirschner MW, Clish CB, Mootha VK. Metabolite Profiling Identifies a Key Role for Glycine in Rapid Cancer Cell Proliferation. *Science*. 2012;336(6084):1040-1044.
158. Tedeschi PM, Markert EK, Gounder M, Lin H, Dvorzhinski D, Dolfi SC, Chan LLY, Qiu J, DiPaola RS, Hirshfield KM, Boros LG, Bertino JR, Oltvai ZN, Vazquez A. Contribution of serine, folate and glycine metabolism to the ATP, NADPH and purine requirements of cancer cells. *Cell Death & Disease*. 2013;4(10):e877-e877.
159. Amelio I, Cutruzzolá F, Antonov A, Agostini M, Melino G. Serine and glycine

- metabolism in cancer. *Trends in Biochemical Sciences*. 2014;39(4):191-198.
160. Locasale JW. Serine, glycine and one-carbon units: cancer metabolism in full circle. *Nature reviews Cancer*. 2013;13(8):572-583.
161. Godwin AK, Meister A, O'Dwyer PJ, Huang CS, Hamilton TC, Anderson ME. High resistance to cisplatin in human ovarian cancer cell lines is associated with marked increase of glutathione synthesis. *Proceedings of the National Academy of Sciences*. 1992;89(7):3070-3074.
162. Aquilano K, Baldelli S, Ciriolo MR. Glutathione: new roles in redox signaling for an old antioxidant. *Frontiers in Pharmacology*. 2014;5:196.
163. Bansal A, Simon MC. Glutathione metabolism in cancer progression and treatment resistance. *Journal of Cell Biology*. 2018;217(7):2291-2298.
164. Baltruskeviciene E, Kazbariene B, Aleknavicius E, Krikstaponiene A, Venceviciene L, Suziedelis K, Stratilatovas E, Didziapetriene J. Changes of reduced glutathione and glutathione S-transferase levels in colorectal cancer patients undergoing treatment. *Tumori Journal*. 2018;104(5):375-380.
165. Mila-Kierzenkowska C, Kędziora-Kornatowska K, Woźniak A, Drewa T, Woźniak B, Drewa S, Krzyżyńska-Malinowska E, Makarewicz R. The effect of brachytherapy on antioxidant status and lipid peroxidation in patients with cancer of the uterine cervix. *Cellular and Molecular Biology Letters*. 2004;9(3):511-518.
166. Kennedy EP, Weiss SB. The function of cytidine coenzymes in the

- biosynthesis of phospholipides. *The Journal of biological chemistry*. 1956;222(1):193-214.
167. van der Veen JN, Kennelly JP, Wan S, Vance JE, Vance DE, Jacobs RL. The critical role of phosphatidylcholine and phosphatidylethanolamine metabolism in health and disease. *Biochimica et Biophysica Acta (BBA) - Biomembranes*. 2017;1859(9):1558-1572.
168. Wehrl HF, Schwab J, Hasenbach K, Reischl G, Tabatabai G, Quintanilla-Martinez L, Jiru F, Chughtai K, Kiss A, Cay F, Bukala D, Heeren RMA, Pichler BJ, Sauter AW. Multimodal Elucidation of Choline Metabolism in a Murine Glioma Model Using Magnetic Resonance Spectroscopy and ¹¹C-Choline Positron Emission Tomography. *Cancer Research*. 2013;73(5):1470-1480.
169. Righi V, Roda JM, Paz J, Mucci A, Tugnoli V, Rodriguez-Tarduchy G, Barrios L, Schenetti L, Cerdán S, García-Martín ML. ¹H HR-MAS and genomic analysis of human tumor biopsies discriminate between high and low grade astrocytomas. *NMR in Biomedicine*. 2009;22(6):629-637.
170. Hattingen E, Bähr O, Rieger J, Blasel S, Steinbach J, Pilatus U. Phospholipid Metabolites in Recurrent Glioblastoma: In Vivo Markers Detect Different Tumor Phenotypes before and under Antiangiogenic Therapy. Platten M, ed. *PLoS ONE*. 2013;8(3):e56439.
171. Gillies RJ, Barry JA, Ross BD. In Vitro and in Vivo ¹³C and ³¹P NMR analyses of phosphocholine metabolism in rat glioma cells. *Magnetic Resonance in Medicine*. 1994;32(3):310-318.

172. Katz-Brull R, Seger D, Rivenson-Segal D, Rushkin E, Degani H. Metabolic markers of breast cancer: Enhanced choline metabolism and reduced choline-ether-phospholipid synthesis. *Cancer Research*. 2002;62(7):1966-1970.
173. Glunde K, Jacobs MA, Bhujwalla ZM. Choline metabolism in cancer: implications for diagnosis and therapy. *Expert Review of Molecular Diagnostics*. 2006;6(6):821-829.
174. Yaku K, Okabe K, Hikosaka K, Nakagawa T. NAD Metabolism in Cancer Therapeutics. *Frontiers in Oncology*. 2018;8(622).
175. Lucena-Cacace A, Otero-Albiol D, Jiménez-García MP, Peinado-Serrano J, Carnero A. NAMPT overexpression induces cancer stemness and defines a novel tumor signature for glioma prognosis. *Oncotarget*. 2017;8(59):99514-99530.
176. Tan B, Young DA, Lu Z-H, Wang T, Meier TI, Shepard RL, Roth K, Zhai Y, Huss K, Kuo M-S, Gillig J, Parthasarathy S, Burkholder TP, Smith MC, Geeganage S, Zhao G. Pharmacological Inhibition of Nicotinamide Phosphoribosyltransferase (NAMPT), an Enzyme Essential for NAD + Biosynthesis, in Human Cancer Cells. *Journal of Biological Chemistry*. 2013;288(5):3500-3511.
177. Watson M, Roulston A, Bélec L, Billot X, Marcellus R, Bédard D, Bernier C, Branchaud S, Chan H, Dairi K, Gilbert K, Goulet D, Gratton M-O, Isakau H, Jang A, Khadir A, Koch E, Lavoie M, Lawless M, Nguyen M, Paquette D, Turcotte E, Berger A, Mitchell M, Shore GC, Beauparlant P. The Small

- Molecule GMX1778 Is a Potent Inhibitor of NAD⁺ Biosynthesis: Strategy for Enhanced Therapy in Nicotinic Acid Phosphoribosyltransferase 1-Deficient Tumors. *Molecular and Cellular Biology*. 2009;29(21):5872-5888.
178. Wang B, Hasan MK, Alvarado E, Yuan H, Wu H, Chen WY. NAMPT overexpression in prostate cancer and its contribution to tumor cell survival and stress response. *Oncogene*. 2011;30(8):907-921.
 179. Muruganandham M, Alfieri AA, Matei C, Chen Y, Sukenick G, Schemainda I, Hasmann M, Saltz LB, Koutcher JA. Metabolic Signatures Associated with a NAD Synthesis Inhibitor-Induced Tumor Apoptosis Identified by ¹H-Decoupled-³¹P Magnetic Resonance Spectroscopy. *Clinical Cancer Research*. 2005;11(9):3503-3513.
 180. Bi T-Q, Che X-M, Liao X-H, Zhang D-J, Long H-L, Li H-J, Zhao W. Overexpression of Nampt in gastric cancer and chemopotentiating effects of the Nampt inhibitor FK866 in combination with fluorouracil. *Oncology Reports*. 2011;26(5):1251-1257.
 181. Zamarron BF, Chen W. Dual Roles of Immune Cells and Their Factors in Cancer Development and Progression. *International Journal of Biological Sciences*. 2011;7(5):651-658.
 182. Carsiotis M. Cellular and Humoral Aspects of the Hypersensitive States. A Symposium Held at the New York Academy of Medicine . H. Sherwood Lawrence. *The Quarterly Review of Biology*. 1960;35(4):355-355.
 183. Burnet M. Cancer--A Biological Approach: III. Viruses Associated with

Neoplastic Conditions. IV. Practical Applications. *BMJ*. 1957;1(5023):841-847.

184. Teng MWL, Galon J, Fridman W-H, Smyth MJ. From mice to humans: developments in cancer immunoediting. *Journal of Clinical Investigation*. 2015;125(9):3338-3346.
185. Dunn GP, Bruce AT, Ikeda H, Old LJ, Schreiber RD. Cancer immunoediting: from immunosurveillance to tumor escape. *Nature Immunology*. 2002;3(11):991-998.
186. Gonzalez H, Hagerling C, Werb Z. Roles of the immune system in cancer: from tumor initiation to metastatic progression. *Genes & Development*. 2018;32(19-20):1267-1284.
187. Dunn GP, Old LJ, Schreiber RD. The Three Es of Cancer Immunoediting. *Annual Review of Immunology*. 2004;22(1):329-360.
188. Restifo NP, Esquivel F, Kawakami Y, Yewdell JW, Mulé JJ, Rosenberg SA, Bannink JR. Identification of human cancers deficient in antigen processing. *The Journal of Experimental Medicine*. 1993;177(2):265-272.
189. Johnsen AK, Templeton DJ, Sy M, Harding C V. Deficiency of transporter for antigen presentation (TAP) in tumor cells allows evasion of immune surveillance and increases tumorigenesis. *Journal of Immunology*. 1999;163(8):4224-4231.
190. Malladi S, Macalinao DG, Jin X, He L, Basnet H, Zou Y, de Stanchina E, Massagué J. Metastatic Latency and Immune Evasion through Autocrine

Inhibition of WNT. *Cell*. 2016;165(1):45-60.

191. Vinay DS, Ryan EP, Pawelec G, Talib WH, Stagg J, Elkord E, Lichtor T, Decker WK, Whelan RL, Kumara HMCS, Signori E, Honoki K, Georgakilas AG, Amin A, Helferich WG, Boosani CS, Guha G, Ciriolo MR, Chen S, Mohammed SI, Azmi AS, Keith WN, Bilsland A, Bhakta D, Halicka D, Fujii H, Aquilano K, Ashraf SS, Newsheen S, Yang X, Choi BK, Kwon BS. Immune evasion in cancer: Mechanistic basis and therapeutic strategies. *Seminars in Cancer Biology*. 2015;35:S185-S198.
192. Curiel TJ, Coukos G, Zou L, Alvarez X, Cheng P, Mottram P, Evdemon-Hogan M, Conejo-Garcia JR, Zhang L, Burow M, Zhu Y, Wei S, Kryczek I, Daniel B, Gordon A, Myers L, Lackner A, Disis ML, Knutson KL, Chen L, Zou W. Specific recruitment of regulatory T cells in ovarian carcinoma fosters immune privilege and predicts reduced survival. *Nature Medicine*. 2004;10(9):942-949.
193. Murdoch C, Muthana M, Coffelt SB, Lewis CE. The role of myeloid cells in the promotion of tumour angiogenesis. *Nature Reviews Cancer*. 2008;8(8):618-631.
194. Maeda H, Shiraishi A. TGF-beta contributes to the shift toward Th2-type responses through direct and IL-10-mediated pathways in tumor-bearing mice. *Journal of Immunology*. 1996;156(1):73-78.
195. Hussain SF, Yang D, Suki D, Aldape K, Grimm E, Heimberger AB. The role of human glioma-infiltrating microglia/macrophages in mediating antitumor immune responses. *Neuro-Oncology*. 2006;8(3):261-279.

196. Hanahan D, Weinberg RA. Hallmarks of Cancer: The Next Generation. *Cell*. 2011;144(5):646-674.
197. Guo ZS. The 2018 Nobel Prize in medicine goes to cancer immunotherapy. *BMC Cancer*. 2018;18(1):1086.
198. Huang RY, Neagu MR, Reardon DA, Wen PY. Pitfalls in the neuroimaging of glioblastoma in the era of antiangiogenic and immuno/targeted therapy - detecting illusive disease, defining response. *Frontiers in neurology*. 2015;6(FEB):33.
199. Moretta L, Moretta A. Unravelling natural killer cell function: triggering and inhibitory human NK receptors. *The EMBO Journal*. 2004;23(2):255-259.
200. Martín-Fontecha A, Thomsen LL, Brett S, Gerard C, Lipp M, Lanzavecchia A, Sallusto F. Induced recruitment of NK cells to lymph nodes provides IFN- γ for TH1 priming. *Nature Immunology*. 2004;5(12):1260-1265.
201. Vivier E. Natural Killer Cell Signaling Pathways. *Science*. 2004;306(5701):1517-1519.
202. Anfossi N, André P, Guia S, Falk CS, Roetynck S, Stewart CA, Bresó V, Frassati C, Revirón D, Middleton D, Romagné F, Ugolini S, Vivier E. Human NK Cell Education by Inhibitory Receptors for MHC Class I. *Immunity*. 2006;25(2):331-342.
203. Kim S, Poursine-Laurent J, Truscott SM, Lybarger L, Song Y-J, Yang L, French AR, Sunwoo JB, Lemieux S, Hansen TH, Yokoyama WM. Licensing of

- natural killer cells by host major histocompatibility complex class I molecules. *Nature*. 2005;436(7051):709-713.
204. Bélanger S, Tu MM, Rahim MMA, Mahmoud AB, Patel R, Tai L-H, Troke AD, Wilhelm BT, Landry J-R, Zhu Q, Tung KS, Raulet DH, Makrigiannis AP. Impaired natural killer cell self-education and “missing-self” responses in Ly49-deficient mice. *Blood*. 2012;120(3):592-602.
 205. Bessoles S, Grandclément C, Alari-Pahissa E, Gehrig J, Jeevan-Raj B, Held W. Adaptations of Natural Killer Cells to Self-MHC Class I. *Frontiers in immunology*. 2014;5:349.
 206. Parham P. MHC class I molecules and kirs in human history, health and survival. *Nature Reviews Immunology*. 2005;5(3):201-214.
 207. Fernandez NC, Treiner E, Vance RE, Jamieson AM, Lemieux S, Raulet DH. A subset of natural killer cells achieves self-tolerance without expressing inhibitory receptors specific for self-MHC molecules. *Blood*. 2005;105(11):4416-4423.
 208. Karlhofer FM, Ribaud RK, Yokoyama WM. MHC class I alloantigen specificity of Ly-49+ IL-2-activated natural killer cells. *Nature*. 1992;358(6381):66-70.
 209. He Y, Tian Z. NK cell education via nonclassical MHC and non-MHC ligands. *Cellular & Molecular Immunology*. 2017;14(4):321-330.
 210. Juelke K, Killig M, Thiel A, Dong J, Romagnani C. Education of hyporesponsive NK cells by cytokines. *European Journal of Immunology*.

2009;39(9):2548-2555.

211. Orr MT, Murphy WJ, Lanier LL. "Unlicensed" natural killer cells dominate the response to cytomegalovirus infection. *Nature Immunology*. 2010;11(4):321-327.
212. Tarek N, Le Luque J-B, Gallagher MM, Zheng J, Venstrom JM, Chamberlain E, Modak S, Heller G, Dupont B, Cheung N-K V., Hsu KC. Unlicensed NK cells target neuroblastoma following anti-GD2 antibody treatment. *Journal of Clinical Investigation*. 2012;122(9):3260-3270.
213. Boudreau JE, Hsu KC. Natural Killer Cell Education and the Response to Infection and Cancer Therapy: Stay Tuned. *Trends in Immunology*. 2018;39(3):222-239.
214. Buddingh EP, Schilham MW, Ruslan SEN, Berghuis D, Szuhai K, Suurmond J, Taminiau AHM, Gelderblom H, Egeler RM, Serra M, Hogendoorn PCW, Lankester AC. Chemotherapy-resistant osteosarcoma is highly susceptible to IL-15-activated allogeneic and autologous NK cells. *Cancer Immunology, Immunotherapy*. 2011;60(4):575-586.
215. Cho D, Shook DR, Shimasaki N, Chang Y-H, Fujisaki H, Campana D. Cytotoxicity of Activated Natural Killer Cells against Pediatric Solid Tumors. *Clinical Cancer Research*. 2010;16(15):3901-3909.
216. Iliopoulou EG, Kountourakis P, Karamouzis M V., Doufexis D, Ardavanis A, Baxevanis CN, Rigatos G, Papamichail M, Perez SA. A phase I trial of adoptive transfer of allogeneic natural killer cells in patients with advanced

non-small cell lung cancer. *Cancer Immunology, Immunotherapy*. 2010;59(12):1781-1789.

217. Miller JS, Soignier Y, Panoskaltsis-Mortari A, McNearney SA, Yun GH, Fautsch SK, McKenna D, Le C, DeFor TE, Burns LJ, Orchard PJ, Blazar BR, Wagner JE, Slungaard A, Weisdorf DJ, Okazaki IJ, McGlave PB. Successful adoptive transfer and in vivo expansion of human haploidentical NK cells in patients with cancer. *Blood*. 2005;105(8):3051-3057.
218. Schafer JR, Salzillo TC, Chakravarti N, Kararoudi MN, Trikha P, Foltz JA, Wang R, Li S, Lee DA. Education-dependent activation of glycolysis promotes the cytolytic potency of licensed human natural killer cells. *Journal of Allergy and Clinical Immunology*. 2019;143(1):346-358.e6.
219. Somanchi SS, Senyukov V V., Denman CJ, Lee DA. Expansion, Purification, and Functional Assessment of Human Peripheral Blood NK Cells. *Journal of Visualized Experiments*. 2011;(48).
220. Denman CJ, Senyukov V V., Somanchi SS, Phatarpekar P V., Kopp LM, Johnson JL, Singh H, Hurton L, Maiti SN, Huls MH, Champlin RE, Cooper LJN, Lee DA. Membrane-Bound IL-21 Promotes Sustained Ex Vivo Proliferation of Human Natural Killer Cells. Dieli F, ed. *PLoS ONE*. 2012;7(1):e30264.
221. Owen OE, Kalhan SC, Hanson RW. The Key Role of Anaplerosis and Cataplerosis for Citric Acid Cycle Function. *Journal of Biological Chemistry*. 2002;277(34):30409-30412.

222. Murphy MP. How mitochondria produce reactive oxygen species. *Biochemical Journal*. 2009;417(1):1-13.
223. Gordon S, Taylor PR. Monocyte and macrophage heterogeneity. *Nature Reviews Immunology*. 2005;5(12):953-964.
224. Weber C, Belge K-U, von Hundelshausen P, Draude G, Steppich B, Mack M, Frankenberger M, Weber KSC, Ziegler-Heitbrock HWL. Differential chemokine receptor expression and function in human monocyte subpopulations. *Journal of Leukocyte Biology*. 2000;67(5):699-704.
225. Durafour BA, Moore CS, Zammit DA, Johnson TA, Zaguia F, Guiot M-C, Bar-Or A, Antel JP. Comparison of polarization properties of human adult microglia and blood-derived macrophages. *Glia*. 2012;60(5):717-727.
226. Dalton D, Pitts-Meek S, Keshav S, Figari I, Bradley A, Stewart T. Multiple defects of immune cell function in mice with disrupted interferon-gamma genes. *Science*. 1993;259(5102):1739-1742.
227. Doyle AG, Herbein G, Montaner LJ, Minty AJ, Caput D, Ferrara P, Gordon S. Interleukin-13 alters the activation state of murine macrophages in vitro: Comparison with interleukin-4 and interferon- γ . *European Journal of Immunology*. 1994;24(6):1441-1445.
228. Stein M, Keshav S, Harris N, Gordon S. Interleukin 4 potently enhances murine macrophage mannose receptor activity: a marker of alternative immunologic macrophage activation. *The Journal of Experimental Medicine*. 1992;176(1):287-292.

229. Gratchev A, Guillot P, Hakiy N, Politz O, Orfanos CE, Schledzewski K, Goerd S. Alternatively Activated Macrophages Differentially Express Fibronectin and Its Splice Variants and the Extracellular Matrix Protein beta1G-H3. *Scandinavian Journal of Immunology*. 2001;53(4):386-392.
230. Schwartz M. "Tissue-repairing" blood-derived macrophages are essential for healing of the injured spinal cord: From skin-activated macrophages to infiltrating blood-derived cells? *Brain, Behavior, and Immunity*. 2010;24(7):1054-1057.
231. Wu A, Wei J, Kong L-Y, Wang Y, Priebe W, Qiao W, Sawaya R, Heimberger AB. Glioma cancer stem cells induce immunosuppressive macrophages/microglia. *Neuro-Oncology*. 2010;12(11):1113-1125.
232. Sica A, Schioppa T, Mantovani A, Allavena P. Tumour-associated macrophages are a distinct M2 polarised population promoting tumour progression: Potential targets of anti-cancer therapy. *European Journal of Cancer*. 2006;42(6):717-727.
233. Mantovani A, Sozzani S, Locati M, Allavena P, Sica A. Macrophage polarization: tumor-associated macrophages as a paradigm for polarized M2 mononuclear phagocytes. *Trends in immunology*. 2002;23(11):549-555.
234. Movahedi K, Laoui D, Gysemans C, Baeten M, Stange G, Van den Bossche J, Mack M, Pipeleers D, In't Veld P, De Baetselier P, Van Ginderachter JA. Different Tumor Microenvironments Contain Functionally Distinct Subsets of Macrophages Derived from Ly6C(high) Monocytes. *Cancer Research*.

2010;70(14):5728-5739.

235. Biswas SK, Mantovani A. Macrophage plasticity and interaction with lymphocyte subsets: cancer as a paradigm. *Nature Immunology*. 2010;11(10):889-896.
236. Xu S, Wei J, Wang F, Kong L-Y, Ling X-Y, Nduom E, Gabrusiewicz K, Doucette T, Yang Y, Yaghi NK, Fajt V, Levine JM, Qiao W, Li X-G, Lang FF, Rao G, Fuller GN, Calin GA, Heimberger AB. Effect of miR-142-3p on the M2 Macrophage and Therapeutic Efficacy Against Murine Glioblastoma. *Journal of the National Cancer Institute*. 2014;106(8).
237. Morris SM. Arginine Metabolism Revisited. *The Journal of Nutrition*. 2016;146(12):2579S-2586S.
238. Hesse M, Modolell M, La Flamme AC, Schito M, Fuentes JM, Cheever AW, Pearce EJ, Wynn TA. Differential Regulation of Nitric Oxide Synthase-2 and Arginase-1 by Type 1/Type 2 Cytokines In Vivo: Granulomatous Pathology Is Shaped by the Pattern of L-Arginine Metabolism. *The Journal of Immunology*. 2001;167(11):6533-6544.
239. Albina JE, Mahoney EJ, Daley JM, Wesche DE, Morris SM, Reichner JS. Macrophage arginase regulation by CCAAT/enhancer-binding protein β . *Shock*. 2005;23(2):168-172.

VITA

Travis Salzillo was born in Bedford, England, the son and only child of Jill Elizabeth Mellor and Joseph Charles Salzillo. He moved to Austin, Texas before the age of 1 and thus has a perfectly boring American accent. Growing up, Travis developed a love of baseball and his favorite team, the Boston Red Sox. Travis excelled in school, graduating in the top 5% of his high school class in 2010 and *summa cum laude* with degrees in Physics and Mathematics from Tarleton State University in 2014. It was here that he discovered his passion for education, and he hopes to eventually lecture courses in higher education at some point in his career. Travis enrolled in the Medical Physics program at the University of Texas MD Anderson Cancer Center UTHHealth Graduate School of Biomedical Sciences in August 2014 in pursuit of his Ph.D. His career goals following graduation involve academic research in and the clinical implementation of advanced imaging techniques in the field of radiation oncology with an emphasis in magnetic resonance-guided radiotherapy.